PHOTOMECHANICS: A STUDY OF INELASTIC BEHAVIOUR OF POLYCARBONATE OF BISPHENOL A

A thesis presented for the degree of Doctor of Philosophy in Mechanical Engineering

in the University of Canterbury,
Christchurch, New Zealand.

by TRẦN-XUÂN DANH

1970.

ACKNOWLEDGEMENTS

Mr. R.M. Taylor of the Mechanical Engineering Department supervised this project, his guidance and interests throughout all stages have been invaluable and are deeply appreciated.

Many members of the academic staff of the University have provided help and advice, in particular Professor D.C. Stevenson of the Mechanical Engineering Department, Mr. C.L. Miles and Mr. K.W. Roth of the Physics Department.

My thanks also to Messrs. E.D. Retallick, K. Sinclair and O. Bolt for their help in constructing experimental equipment. Equipment has also been made available by all engineering departments and I am grateful to Messrs. R.I. Stewart, A.R. Hirst, M.E. Webb, H.J. Anink and Miss B.J. Barclay. The staff of Kodak Ltd. and Christchurch Photoengravers Ltd. provided indispensable help in photography and photoengraving.

I wish to thank the staff of the Engineering and Science library for their generous assistance in procuring interloans and extending many overdue books and journals.

Mesdames D.M. Eggleston, P. Barnett, V.J. Grey and Miss C. Hawkins and Mr. E. Thompson have displayed care and interest in the production of the thesis.

My fellow post-graduate students of the Mechanical Engineering Department and my friends have contributed in many

indirect ways during the course of this project.

Understanding and encouragement were constantly given by the Egglestons and Miss T.T. Kim-Anh, who, in spite of the distance, shared much of the frustration and hardship.

ABSTRACT

The photomechanical relationship of a polymer undergoing finite deformation is examined in light of basic considerations of the relationship between the index tensor and the mechanical tensors: the stress and strain tensor, and from the molecular mechanisms of birefringence and deformation.

For polycarbonate of bisphenol A, it is concluded that, in an isothermal deformation the index tensor can be expressed as a linear function of the strain tensor. For the range of principal strain difference studied (within .15) first order approximation of the linear photomechanical relationship is adequate for polycarbonate of bisphenol A. That is to say that the fringe order per unit optical path is proportional to the difference of the secondary principal strains and that the isoclinics represent the secondary principal strain directions.

Uniaxial tensile tests in the form of creep tests and stress relaxation tests, biaxial plane stress experiments, strain-freezing experiments and experiments involving mechanical non-coincidence are in agreement with the strain-optical law. The strain-fringe coefficient of polycarbonate of bisphenol A decreases with increasing temperature and decreases slightly at large strain in a room temperature deformation. Characterisation tests in uniaxial tension show that the time dependence of inelastic

deformation of polycarbonate is non-linear with respect to the stress applied.

The Moiré grid analyser method for the analysis of finite strain is presented. The method is well suited for strain measurements in studying inelastic behaviour of polymers.

CONTENTS

LIST OF FIGURES

facing Pages

facing pages

LIST OF COMMONLY OCCURRING SYMBOLS

(Some of these are temporarily defined to have other meanings in certain Sections; all symbols are defined where they first occur.)

a_i, a_1, a_2, a_3	coordinate axes associated with the undeformed state.
$\underline{B}$	magnetic induction vector.
c	velocity of light in vacuo.
C	stress - optical coefficient.
C_σ	stress - fringe coefficient.
C_ϵ, c_ϵ	strain - fringe coefficient.
C_ϵ^A	apparent strain - fringe coefficient in strain freezing experiments.
C_ϵ^R	residual strain - fringe coefficient in strain freezing experiments.
e_x^L, e_y^L, e_1^L, e_2^L	Lagrangian engineering strains (normal).
e_x^E, e_y^E, e_1^E, e_2^E	Eulerian Engineering strains (normal).
E	modulus of elasticity.
$\underline{E}$	electric field intensity vector.
f	frequency of grating.
g	original specimen pitch.
g_a	analyser pitch.
h	optical path, thickness.
h_n	interfringe distance.
h_{ni}	initial interfringe distance.
$\underline{H}$	magnetic field intensity vector.
$\underline{\underline{K}}$, K_{ij}	dielectric tensor.
K	strain - optical coefficient.

K_σ	stress concentration factor.
K_γ	maximum-shear-strain concentration vector.
m_{aX}, m_{aY}	index of analyser X, Y grating.
m_{sX}, m_{sY}	index of specimen X, Y grating.
n	model fringe order
N	fringe order per unit optical path.
$N^{(1)}$	first order approximation of N (equation 2.9).
$N^{(2)}$	2nd order approximation of N (equation 2.10).
N_p	inelastic portion of N.
N_{max}	maximum fringe order in strain freezing experiments.
N_o	initial fringe order in strain freezing experiments.
N^R	residual or frozen fringe order in strain freezing experiments.
N^T	total fringe order in experiments on the meaning of isoclinics.
N_{ij}	fringe order tensor
N'_1, N'_2	secondary principal values of N_{ij}.
N_X, N_Y	Moiré fringe order of X, Y fringe family.
r, r^N	ratios (equation 6.21).
R	relative retardation.
t	time.
t_o	reference time.
t_i	time from the instant of loading completed (isochronous).
T	temperature.
T_g	glass-transition temperature.

$\underline{u}$	displacement vector.
u, v, w	displacements.
v_1', v_2'	velocities of polarised waves.
v_o	velocity of light in a medium in the undeformed state.
x, y, z	coordinate axes.
(x, y)	deformed specimen grid directions.
(x_o, y_o)	initial specimen grid directions.
X, Y	grating family, Moiré fringe family.
α	principal strain direction.
β	angle between load lines of test pieces in experiments on the meaning of isoclinics.
$\gamma, \gamma_{xy}, \gamma_{xy}^{L}$	Lagrangian engineering shear strain.
γ_{xy}^{E}	Eulerian engineering shear strain.
δ_{ij}	Kronecker delta.
ϵ_{ij}	strain tensor.
ϵ_1, ϵ_2	principal strains.
$\epsilon_1' \quad \epsilon_2'$	secondary principal strain.
ϵ_{ij}^{L}	Lagrangian finite strain tensor.
ϵ_{ij}^{E}	Eulerian finite strain tensor.
$\epsilon_{ij}^{R}, \epsilon_{ij}^{T}$	residual strain tensor, total strain tensor, in experiments on the meaning of isoclinics.
ξ, η	analyser grid direction.
$\underline{\underline{\eta}}, \eta_{ij}$	index tensor.
θ	isoclinic directions.
θ_o	initial rotation.

ϕ_X, ϕ_Y	fringe inclination.
ϕ_{Xi}, ϕ_{Yi}	initial fringe inclination.
λ	initial mismatch.
λ	wavelength in vacuo.
λ_{ij}	mechanical state tensor.
λ'_α, λ'_1, λ'_2	secondary principal values of λ_{ij}
μ_o	refractive index in undeformed state.
μ_{ij}	refractive index tensor.
ν	Poisson's ratio.
σ_{ij}	stress tensor.
σ	uniaxial tensile stress.
σ_1	stress parameter in Ramberg-Osgood equation.
τ_{ij}	stress tensor.
τ_{xy}	shear stress.
ω	wave frequency.
$\Omega(t)$	normalised optical creep function.
$\exists(t)$	normalised mechanical creep function.

CHAPTER 1

REVIEW OF LITERATURE

1.1 INTRODUCTION

Photoelasticity, an experimental method of stress and strain analysis employing transparent model material and polarised light, originated with Sir David Brewster's discovery of birefringent effects in strained glass in 1815. Lack of suitable material prevented the discovery being developed into a useful experimental technique until almost a century later when "Xylonite" (celluloid) was used by Coker. As more suitable materials became available, new experimental techniques and rigorous mathematical formulation developed, and the science has expanded into a firmly established field of experimental stress analysis. In photoelasticity only linear elastic model materials are used. Linear viscoelastic materials could be used under certain conditions discussed by Mindlin.(1)*

The extension of techniques of photoelasticity in the study of other fields of mechanics such as fluid flow, viscoelasticity, plasticity and dynamic elasticity has justified the term photomechanics. The first studies of photomechanical relations beyond the elastic limit were carried out by Coker,

* Refers to references.

Filon and their co-workers on celluloid in the early 1920's but these were not followed up until the early 1950's when plasticity of materials became an important field of mechanics. Because of the difficulty and controversy involved in the analytical approach, experimental techniques employing models, such as the photoelastic technique, have been sought to study plasticity. Such studies have resulted in a confused terminology and account for the phenomenologically biased works that have been published. The literature is surveyed and classified according to the viewpoints of these studies.

1.2 PHOTOPLASTICITY AND PHOTOINELASTICITY

The term "photoplasticity" has been used to indicate the use of photoelasticity techniques in studying plasticity (time independent irrecoverable deformation) by using models which exhibit similar plastic behaviour. However, apart from silver chloride, most model materials used are polymers which are only partly crystallised. Their behaviour beyond the linear elastic limit is a combination of viscoelastic (time dependent recoverable and irrecoverable deformation) and plastic deformation. Inelasticity would be a more proper term to cover post-elastic deformation of polymers, hence the term "photoinelasticity".

In the study of "photoplasticity", much emphasis is normally put on the phenomenological behaviour of the model material and the application of birefringence studies to

plastic stress analysis of metallic materials; the actual photomechanical behaviour of the model material is usually neglected. Little interest has been shown in using polymers to study inelastic deformation as, for example, in the high temperature deformation of metals (creep). The similarity criterion has not been thoroughly investigated to the same extent as in photoelasticity.

1.3 EXPERIMENTAL STUDIES OF PHOTOINELASTICITY RELATIONS

Experimental studies in photoinelasticity using celluloid began early in the 1920's with the works of Coker, Filon and co-workers; Filon and Jessop's paper published in 1923[2] was of special note. In 1951, Hetenyi[3] and Fried[4] renewed interest in the subject. Various materials have been studied but less attention has been paid to their specifications than to the conditions of the tests such as temperature, relative humidity (R.H.), rate of loading or strain rate. Hetenyi showed that birefringence in a nylon co-polymer is always proportional to strain, not to stress. Fried and Soup[5], working with Polyethylene similarly found that birefringence is proportional to strain, independently of the strain rate.

Hiltscher[6] tested polystyrene in compression and found more complex behaviour: beyond the elastic limit, fringe order decreases and even reverses in sign.

Celluloid has been studied by various researchers, but the grade of celluloid and the amount of camphor are not

specified, except in Fujii and Tokuoka.[7] Mönch and Loreck[8] emphasised the similarity of the loading programmes of the model to those of the calibration test pieces. They constructed "effective" stress-strain curves (isochronous stress-strain curves) from stress-strain curves of different strain rates tests and observed that with very slow loading or at large "test times" after the start of loading, the curves are less affected by strain rate or "test times". They also used dispersion as a measure of "plastic" distortion. Nisida et al[9] with very slow loading obtained an ideal plastic stress-strain curve and found, during the flow, fringe order increasing but not proportional to strain. Frocht and Thompson [10,11] also used extensive creep of celluloid at constant temperature and R-H and observed that when observations were made at periods exceeding three hours, maximum strain was less than 8% , and for a monotonically increasing loading path, fringe order is a single valued function of stress. Together with Cheng[12,13] using plane models and tubes, they thoroughly investigated the relationship between the stress and the strain principal directions and isoclinics in the case of mechanical non-coincidence (i.e. principal directions of stress and strain tensors are not parallel). They found that fringe order is a function of the difference and history of the secondary principal stresses (see Appendix 1) and that the isoclinics always represent principal stress directions.

Bayoumi and Frankl[14] reached different conclusions with Catalin 800 and CR-39, and proposed the "mechanical state" tensor, a linear combination of stress and strain tensor, to be related to birefringence.

Gubkin et al[15] discussed the suitability of various materials for photoplasticity, among them Bakelite, I.M. 44, glycerin, celluloid and silver chloride. Their studies are confined to uniaxial tests, to the application of photoelastic techniques to viscoelastic flow problems, to modelling manufacturing processes using polymers, and to studying mechanisms of plasticity in silver chloride.

Recently, Johnson III and Goldsmith[16] studied nylon, polyethylene and a polyester in the post elastic region and obtained a linear relationship between fringe order and strain, independently of strain rate, at least up to 20% strain. Ito[17], Sharples[18] recommended polycarbonate as a photoplastic material and Cloud[19] studied its photomechanical relation within the linear elastic limit. Brill[20] found from the uniaxial tensile behaviour of polycarbonate that birefringence is a single-valued function of the principal strain difference. Biaxial tests also substantiated this conclusion and indicated that isoclinics represent the principal strain directions. Brill's works were not available to the author until the final stage.

1.4 SEMI-EMPIRICAL STUDIES

The experimental works indicated that the photomechanical behaviour beyond the elastic limit depends on many factors, the most important being the material itself. Various theories have been advanced to explain the observed behaviour of a particular material.

Filon and Jessop[2] assumed a heterogeneous structure of celluloid consisting of two constituents, one perfectly elastic, the other plastic and both following a stress-optical relation.

Heywood[21] considered birefringence to be strain induced, but that two strain optical coefficients should be used for the elastic and inelastic portion of the total strain. This hypothesis has been supported by various researchers[7,14, 22-24]. Bayoumi and Frankl, and Tokuoka formulated a tensor relationship between birefringence, stress tensor and total strain tensor.

1.5 MOLECULAR STRUCTURE

From a macroscopic point of view birefringence in polymers is a result of the optical anisotropy arising out of the polarisability of the molecules which can be represented by a dielectric tensor or an ellipsoid. If the distribution of such molecular ellipsoids is statistically accidental, the material is macroscopically optically isotropic. Anisotropy arises when there is any biased orientation of these ellipsoids.

Javornicky[22] regarded birefringence as consisting mainly of

1. stress birefringence n_{σ}, due to displacement of atoms, altering the interatomic forces or primary bonds. This is instantaneously reversible and is related to the elastic strain portion, hence to stress.
2. orientation birefringence n_{OR}, due to orientation and straightening of molecular chains. These effects may be reversible (instantaneous or delayed) or irreversible, and are related to the inelastic strain portion.

These two types of birefringence always arise simultaneously, although they may be different in magnitude and sign. The relationship between birefringence and molecular structure in polystyrene and its derivatives was studied by Andrews and co-workers (25-28). They showed that the photoelastic effect in polystyrene is mainly due to the polarisability of the phenyl rings and is influenced by any mechanism which affects the flexibility of the phenyl groups in orientating. Taylor and Darin[29] found that birefringence in elastomers is mainly due to the oriented crystallites and that the degree of crystallization estimated from birefringence measurements agreed with X-ray results.

1.6 EXPERIMENTAL APPLICATION OF PHOTOINELASTICITY - SIMILARITY AND ANALYSIS

The similarity criterion has not been firmly established

for the transition of photoinelastic data of models to the stress and strain analysis of prototypes in post-elastic range. This topic was mentioned in[5,6,10].

The criteria that have been generally accepted for a monotonically increasing loading path were essentially as follows:

1. similar shape of stress-strain curve (in uniaxial tests)
2. similar law of yielding and flow rules.
3. same Poisson's ratio.

To formulate these conditions analytically and to verify them experimentally would require a thorough testing programme, touching upon some aspects that are still open to debate in the much explored field of metallic plasticity and creep. The Ramberg-Osgood[30] equation has been accepted for the purpose of comparison of stress-strain curves. However, due to the viscoelastic nature of polymer deformation, almost any shape of the Ramberg-Osgood curve can be generated, using creep due to time and/or temperature[9,22,31,32]. Poisson's ratio of inelastic strain in polymer has been assumed to be half, as in plasticity and creep of metals.

The laws of yielding and plastic flow have not been thoroughly investigated for polymers because of the complexity of the experiments. Hiltscher[6] indicated that polystyrene obeys the total strain energy theory and Mönch and Jira[38] showed that celluloid obeys the octahedral shear stress law

of yielding (von Mises), however, their works are far from being conclusive.[22] Recent works by Ely[34] for Nylon 6-6 indicated that both theories compare favourably with experimental results. Methods of analysis have been limited to cases where the secondary principal stress difference, $(\sigma_1' - \sigma_2')$, can be expressed as a single valued function of birefringence. Separation of principal stress requires further assumptions e.g. the shear difference method can be used only if isoclinic directions represent the principal stress directions.

Bayoumi and Frankl[14] and Javornicky[22] used the assumption that the elastic strain-induced birefringence disappears instantaneously to relate the difference of the amounts of birefringence on loading and unloading to $(\sigma_1' - \sigma_2')$. However, as pointed out by Frocht and Thompson[10] the technique is not generally applicable to a non-homogeneous stress state. The scattered light technique has been mentioned as the most suitable method for three dimensional photoplasticity because of its non-destructive nature. Hunter and Schwarz[32] employed "stress" frozen techniques to generate the desired "effective" stress-strain (i.e. initial stress - frozen strain) and used the slicing technique to study simulated cracks problems. Crack problems have also been studied by Brinson[35] using polycarbonate. Early applications of photoplasticity were mainly qualitative, such as effect of creep on bending stress distribution[4], stress

distribution due to indentation by a wedge and compression of a wedge by a flat die[9]. The stress and strain concentration due to a notch (hole, groove) in a tensile plate has been a popular case study for various researchers[3,5,6,8,10,11,22,36,), the works of Frocht and Thompson and Javornicky being the most extensive.

1.7 CONCLUSIONS

To date no definite quantitative conclusions on photomechanical relations beyond the linear-elastic state have been derived. Mechanical and optical properties of a polymeric material are closely related to the molecular structure of the polymer, its mechanical and thermal history and the conditions of the tests. Most experiments have been conducted at constant temperature (room temperature) and constant relative humidity and for a monotonically increasing loading path. Emphasis has been put on the similarity of loading programmes of the model to those of the calibration test piece. Such a loading programme can be selected from a series of characterisation curves (creep, constant strain rate, stress relaxation tests) and by using the effect of time and/or temperature on the amount of viscoelastic flow a desirable stress-strain curve can be simulated. The "simulation" technique and the application of birefringence measurements to plasticity problems of metals has caused confusion and neglect in formulating a concrete similarity

criterion. For a monotonically increasing loading path the Frocht and Thompson criterion is accepted as sufficient.

Another important question is the meaning of isoclinics. Do they represent the secondary principal directions of the stress tensor or those of the strain tensor, or neither? The Frocht shear difference technique based on the equilibrium equation of the stress tensor is applicable for elastic as well as inelastic stress distribution. However, it is useful only if the isoclinics represent the secondary principal stress directions.

Apart from the usual requirements of a photoelastic model material, the following points are desirable in "photoplasticity" studies:

1. Similar uniaxial stress-strain curves for model and prototype materials, preferably without plastic instability.
2. Similar laws of yielding and of flow and similar nature of post-elastic deformation.
3. Similar Poisson's ratio.
4. Moderate optical sensitivity; not exhibiting too many fringes above the elastic limit.
5. Linear stress-optical or linear strain-optical relation.
6. Isoclinics represent secondary principal stress directions or secondary principal strain directions.

1.8 SCOPE OF THESIS

Polycarbonate is selected for the photomechanical studies beyond the elastic limit. Because of the finite deformation and high optical sensitivity of polycarbonate the fundamental relations of photomechanics are reconsidered. The Maxwell electromagnetic wave equation and its solution are investigated for the case of a highly optical sensitive polymer undergoing finite deformation.

Various descriptions of finite deformation are presented and their relations are derived. (Chapter 2).

An explanation of photomechanics in terms of molecular structure is presented with particular reference to polycarbonate. (Chapter 3).

The development of the Moiré grid analyser technique of surface finite strain measurement for a non-homogeneous strain field is given. (Chapter 4).

Uniaxial tests of characterisation including strain-freezing tests are presented. (Chapter 5).

Biaxial experiments on the meaning of isoclinics in the case of mechanical non-coincidence were carried out. (Chapter 6).

A case-study of plates with semi-circular grooves or central holes under tension is presented. The results are

compared with various published theoretical and experimental works. (Chapter 7).

CHAPTER 2

CONSIDERATIONS OF BASIC PHOTOMECHANICAL RELATIONSHIPS OF AN OPTICALLY SENSITIVE POLYMER, UNDER FINITE DEFORMATION.

2.1 INTRODUCTION

The birefringence effect observed in a polariscope can be explained in terms of the interference of two polarised light waves travelling at slightly different velocities, where light is described as a simple harmonic wave.

In photoelasticity the relationships between the isochromatics and isoclinics and the mechanical tensors (stress and strain tensors) are derived from either the stress-optical law or the strain-optical law. These two laws are equivalent for a linear elastic material undergoing infinitesimal strain and small changes in refractive index. If the deformation and change of refractive index are finite, as in the case in an optically sensitive polymer in post-elastic region, the following points need to be reconsidered:

1. simple harmonic waves as solutions of Maxwell's equations.
2. linear stress-optical or strain-optical laws.
3. description of finite deformation in photomechanics.

Point 3 is extended to relate Lagrangian and Eulerian finite strain tensors and "engineering strains" to provide a basis for later works.

2.2 MAXWELL'S ELECTROMAGNETIC EQUATIONS

The propagation of light in a medium can be described in terms of Maxwell's electromagnetic equations when the medium is optically anisotropic such as some crystals or a polymer under deformation, the dielectric tensor K_{ij} is used to describe the anisotropy effect on light propagation. It can be shown that (see Appendix 2), for an uncharged, non-magnetic, anisotropic dielectric medium (a polymer under deformation for example), the magnetic field intensity vector $\underline{H}$ satisfies the equation

$$\mu_o \frac{\partial^2 \underline{H}}{\partial t^2} = - \text{curl } (\underline{\underline{\eta}} \cdot \text{curl } \underline{H}) \qquad (2.1)$$

where $\underline{\underline{\eta}}$ is the index tensor defined by: $\eta_{ij} = (K_{ij})^{-1}$

Mindlin[37] showed that the simple harmonic wave solution is an exact solution of the equation (2.1) only if the anisotropy is homogeneous.

The error of approximation depends largely on the optical path and on the rate of change of refractive index with respect to a length dimension in the plane normal to the optical path (see Appendix 2).

The analysis indicates that except for regions of large gradient of refractive index, the simple harmonic wave is a good approximate solution of equation (2.1), i.e. corresponding to an incident plane polarised wave on the medium, there are two plane polarised waves travelling through the medium

such that:

1. the directions of polarisation of the two polarised waves are along the secondary principal axes of the refractive index tensor μ_{ij} ($\mu_{ij} = K_{ij}^{\frac{1}{2}}$).
2. their refractive indices are secondary principal values of μ_{ij}.

For a detailed proof see Dill and Fowlkes[38] or Coker et al[39].

2.3 INTERPRETATION OF ISOCLINICS AND ISOCHROMATICS

Once the simple harmonic wave is accepted as a solution of Maxwell's equations, Isochromatics and Isoclinics observed in a polariscope can be related to the refractive index tensor of the medium. The proof is well covered in standard texts on photoelasticity. Briefly, for a plane slab of the medium of homogeneous anisotropy:

1. the <u>isoclinics</u> (lines of zero intensity) in a crossed plane polariscope are loci of points where the directions of polarisation of the two polarised waves are parallel to the polarising axes of the polariscope.
2. the <u>isochromatics</u> (lines of local minimum intensity) are loci of points where the relative retardation R is a multiple of the observing wave length. It can be shown that

$$R = h(\mu_1' - \mu_2') \qquad (2.2)$$

where, h = optical path

μ_1', μ_2' = secondary principal values of μ_{ij} associated with the optical path

for a monochromatic light of wave frequency ω, wave length λ in vacuo,

$$\omega = \frac{c}{\lambda}$$

where c is velocity of light in vacuo. (Unlike wave length, wave frequency does not change in travelling through various media.)

The fringe order n is defined as:

$$n = \frac{R}{\lambda} \qquad (2.3)$$

Defining the fringe order per unit thickness as N,

$$N = \frac{n}{h} = \frac{\mu_1' - \mu_2'}{\lambda} \qquad \text{by (2.2)}$$

where $\mu_1' = \frac{c}{v_1'}$ giving:

$$N = \omega\left(\frac{1}{v_1'} - \frac{1}{v_2'}\right) \qquad (2.4)$$

(v_1', v_2' are velocities corresponding to μ_1', μ_2').

The equations (2.2) - (2.4) are optically true for any anisotropic dielectric medium, regardless of the cause of anisotropy. The definition in (2.3), although arbitrary, avoids the difficulty of wave length change in the medium.

2.4 BASIC PHOTOMECHANICAL RELATIONSHIP

A photomechanical relationship relates the birefringence effects to the mechanical state, i.e. the dielectric tensor to the tensors of mechanics (stress andstrain tensors).

In linear elasticity the stress and strain tensors are coaxial. By symmetry the dielectric tensor is also coaxial

to these tensors and either stress tensor σ_{ij} or strain tensor ϵ_{ij} can be used in the photomechanical relationship.

In inelastic loading involving mechanical non-coincidence, the mechanical state should generally be described by a function of σ_{ij} and ϵ_{ij}. Following Bayoumi and Frankl[14] let such a function be called the "mechanical state tensor" λ_{ij}.

The simplest photomechanical relationship is a linear one between λ_{ij} and K_{ij} (or η_{ij}):

$$\eta_{ij} = (\eta_0 + a_0)\ \delta_{ij} + a_1 \lambda_{ij} \qquad (2.5)$$

where

δ_{ij} = Kronecker's delta.

η_0 = principal values of η_{ij} in the undeformed state.

Coefficients a_0, a_1 are related to isotropic and anisotropic change of η_{ij} respectively.

Equation (2.5) can be written in terms of secondary principal values:

$$\eta'_\alpha = (\eta_0 + a_0) + a_1 \lambda'_\alpha \qquad \alpha = 1, 2. \qquad (2.6)$$

substitute $(v'_\alpha)^2 = c^2 \eta'_{\alpha+1}$:

$$(v'_\alpha)^2 = v_0^2 + c^2(a_0 + a_1 \lambda'_{\alpha+1}) \qquad \alpha = 1, 2.$$

$$\text{i.e. } \frac{1}{v'_\alpha} = \frac{1}{v_0}\left[1 + \frac{c^2}{v_0^2}\ (a_0 + a_1 \lambda'_{\alpha+1})\right]^{-\frac{1}{2}} \qquad (2.7)$$

substitute equation (2.7) into equation (2.4):

$$N = \frac{\omega}{v_o}\left\{\left[1+\frac{c^2}{v_o^2}\left(a_o + a_1\lambda_2'\right)\right]^{-\frac{1}{2}} - \left[1+\frac{c^2}{v_o^2}\left(a_o + a_1\lambda_1'\right)\right]^{-\frac{1}{2}}\right\} \tag{2.8}$$

This is the exact expression of N in a linear photomechanical relationship.

Using binomial expression and upon neglecting high order terms of $\frac{c^2}{v_o^2}(a_o + a_1\lambda_\alpha')$ we have:

$$* \quad N^{(1)} = \frac{\omega c^2}{2v_o^3} a_1(\lambda_1' - \lambda_2'), \text{ neglecting second and higher order terms.} \tag{2.9}$$

$$* \quad N^{(2)} = \frac{\omega c^2}{2v_o^3} a_1(\lambda_1' - \lambda_2')\left\{1 - \frac{3}{4}\frac{c^2}{v_o^2}\left[2a_o + a_1(\lambda_1' + \lambda_2')\right]\right\}, \tag{2.10}$$

neglecting third and higher order terms, where the superscripts (1), (2) indicate the order of the expressions of N.

Equation (2.9) gives the stress-optical and strain-optical laws when σ_{ij} and ϵ_{ij} replaces λ_{ij} respectively.

The linear photomechanical law (equation (2.5)) can include any complex photomechanical relationship if λ_{ij} is expressed as a complicated non-linear function of σ_{ij} and ϵ_{ij}, as in Tokuoka's papers[23,24], where the "pseudo strain tensor" replaces λ_{ij}.

2.5 STRESS- AND STRAIN-OPTICAL LAWS

In the stress-optical law, isoclinics are related to directions of secondary principal stresses, and the relative retardation is proportional to the difference of secondary principal stresses:

$$R = C\,h\,(\sigma_1' - \sigma_2') \tag{2.11}$$

or

$$N = c_\sigma\,(\sigma_1' - \sigma_2') = \frac{1}{f}(\sigma_1' - \sigma_2') \tag{2.12}$$

where:

C = stress-optical coefficient

c_σ = stress-fringe coefficient

f = fringe-stress coefficient or material fringe value.

Similarly in the strain-optical law, isoclinics are related to secondary principal strain directions and

$$R = K\,h\,(\epsilon_1' - \epsilon_2') \tag{2.13}$$

$$N = c_\epsilon\,(\epsilon_1' - \epsilon_2') = \frac{1}{g}(\epsilon_1' - \epsilon_2') \tag{2.14}$$

where

K = strain-optical coefficient

c_ϵ = strain fringe coefficient

g = fringe-strain coefficient.

For a linear elastic material the two laws are equivalent, and it can be shown that:

$$\frac{K}{C} = \frac{c_\epsilon}{c_\sigma} = \frac{f}{g} = \frac{E}{1+\nu} \tag{2.15}$$

These laws are only first order approximation of the linear

photomechanical relationship as shown in equation (2.9).

When the term $\frac{c^2}{v_0^2}(a_0 + a_1 \lambda'_\alpha)$ in equation (2.8) is not small compared to unity, these laws are not satisfactory (such as in an optically sensitive material undergoing finite deformation). To assess the error involved, equation (2.9) is compared to equation (2.10).

2.6 ERROR OF FIRST ORDER LINEAR PHOTOMECHANICAL LAWS

From equations (2.9) and (2.10)

$$\frac{\delta N}{N} = \frac{N^{(2)} - N^{(1)}}{N^{(1)}} = -\frac{3}{4}\frac{c^2}{v_0^2}\left[(a_0 + a_1 \lambda'_1) + (a_0 + a_2 \lambda'_2)\right] \quad (2.16)$$

by equation (2.7)

$$\frac{\delta N}{N} = -\frac{3}{4}\left[\left(\frac{v'_2}{v_0}\right)^2 - 1 + \left(\frac{v'_1}{v_0}\right)^2 - 1\right]$$

using $\mu = \frac{c}{v}$ we have:

$$\frac{\delta N}{N} = -\frac{3}{4}\left[\left(\frac{\mu_0}{\mu'_1}\right)^2 + \left(\frac{\mu_0}{\mu'_2}\right)^2 - 2\right] \quad (2.17)$$

Let

$$\mu'_1 = \mu_0(1 + \delta_1)$$
$$\mu'_2 = \mu_0(1 + \delta_2) \quad (2.18)$$

where μ_0 is the refractive index in the undeformed state.

$$\frac{\delta N}{N} = -\frac{3}{4}\left[(1+\delta_1)^{-2} + (1+\delta_2)^{-2} - 2\right]$$

$$\simeq +\frac{3}{2}(\delta_1 + \delta_2)$$

$$= 3\left(\frac{\mu_1' + \mu_2'}{2\mu_0} - 1\right) \text{ approximately.} \qquad (2.19)$$

Equation (2.19) indicates that the error depends on the sum of the two refractive indices of the two polarised waves, i.e. on the values of λ_1' and λ_2'. Therefore in a material obeying stress-optical law, the error of first order photomechanical law is related to the isotropic component of the stress tensor.

The error can be evaluated if μ_1' and μ_2' are measured, e.g. by interferometry[40-42].

2.7 STRAIN DESCRIPTION IN PHOTOMECHANICS

Two common descriptions of continuum mechanics are:

1. Lagrangian description, related to the undeformed state.
2. Eulerian description, related to the deformed state.

The stress tensor, which is developed from either the equilibrium or from the equation of motion of a volume element of the deformed body, has been customarily associated with Eulerian description. In the case of infinitesimal deformation the Lagrangian and Eulerian description of strain are the same. However, for the finite deformation encountered in post-elastic behaviour of polymers, a distinction

must be made between the two descriptions.

Birefringence, being related to the dielectric tensor of the deformed state, is apt to be described in Eulerian variables. This point was also raised by Coker et al.(39,§3.06) A satisfactory finite strain description should:

1. have tensorial properties to allow principal values to be evaluated.
2. be related to physical measurements (length and angle).

Strain analysis in continuum mechanics describes finite deformation in tensorial quantities while experimental strain analysis employs expressions related to physical measurements. Numerous strain measures allow for flexibility in choosing a suitable description for the problem considered but also give rise to confusion.

Finite strain tensors and "engineering" strains are set out in detail in Appendix 3; the distinction and relationship between different strain descriptions are also clarified.

Most strain measurement techniques give the Lagrangian engineering strains such as electrical strain gauges, Moiré fringes (see Chapter 4). The analysis presented allows the principal values of the Eulerian finite strain tensor to be evaluated from those of Lagrangian engineering strains. The boundary between finite and infinitesimal strain is shown to depend on the acceptable error. For a

maximum error of 10%, the finite strain tensor and the engineering strains of the same description (Eulerian or Lagrangian) can be considered equivalent if the magnitude of the maximum normal strain is less than 5% and if it is less than 25% the Eulerian and the Lagrangian finite tensors can be considered the same.

2.8 CONCLUSION

When an optically sensitive material undergoes finite deformation, the simple harmonic wave is still a good approximate solution of Maxwell's electromagnetic equations, except in regions of large gradient of optical anisotropy. A basic photomechanical relationship is one between the dielectric tensor and the mechanical state tensor, a function of the stress and the strain tensors. It was shown that the stress- or strain-optical laws of photoelasticity are first order approximations of the linear photomechanical relationship, the error involved can be large when the changes in refractive index from μ_o corresponding to the two polarised waves are large and are of the same sign. In a photomechanical relationship, finite deformation is preferably described in terms of Eulerian variables, which can be evaluated in terms of experimental measurements of Lagrangian variables. Distinction must be made between various strain descriptions when the deformation is finite.

Furthermore, a general consideration of a photomechanical relationship in inelasticity indicates that both stress and strain tensors should be used. In other words the isoclinics may represent neither the principal stress directions nor the principal strain directions.

CHAPTER 3

PHOTOMECHANICAL BEHAVIOUR OF POLYMERS FROM THE VIEWPOINT OF MOLECULAR STRUCTURE, WITH PARTICULAR REFERENCE TO POLYCARBONATE OF BISPHENOL A.

3.1 INTRODUCTION

Most of the commonly used photomechanical model materials are polymers. They can be considered as linear elastic or linear viscoelastic materials when they are subjected to small deformation. The theory of linear viscoelasticity adequately describes such behaviour. However, under large deformation the time dependence of the behaviour of polymers may be non-linear with respect to the applied stress.

The birefringent property of polymers has been explained in terms of the diphase (or multiphase) theory. This theory considers polymers as consisting of a rigid skeleton and a viscous amorphous mass, resembling the spring and dashpot model of mechanical behaviour.

When large deformation is considered, such models, no matter how complicated, fail to account for the complex photomechanical behaviour of a number of polymers. On the other hand, a quantitative statistical analysis of the contribution made by the atoms, which form the molecular chains, to deformation and birefringence has not been successful.

The photomechanical behaviour of polymers is here explained from the point of view of their molecular structure, with particular reference to polycarbonate of bisphenol A.

3.2 MECHANISM OF DEFORMATION

The deformation of polymers is explained in terms of molecular chain motion. The most catastrophic form of mobility is the scission of primary bonds. However, before this happens, a chain segment can surmount the lower secondary binding energy to slide over other segments of its own chain or of other neighbouring chains and to rotate about primary bonds. The chain motion, if confined to the switching to and fro of a finite number of configurations, is a recoverable process (instantaneous or retarded); however, if it tends to deform the neighbourhood, a return to the original chain entanglement is unlikely and the chain motion is thus irreversible. In cross-linked and highly crystallized polymers, the cross links and the crystallized regions act as permanent entanglements. True molecular flow short of primary bond scission is not possible.

The glass transition temperature T_g marks a change in the mobility of chain segments due to thermal energy. Above T_g chain segments are readily activated to slide and rotate. Application of a small stress would bias chain segment motion and polymers can be fairly described as linear

viscoelastic. Below T_g, the chain motion is more stress dependent, especially if the polymer has high crystallinity.

Increasing crystallinity results in increased Young's modulus, in high strength but also results in a tendency towards failure at low strain. Another disadvantage in using a polymer of high crystallinity as a photoplastic model material is its opacity, unless very thin film is used. Cross-linked polymers and elastomers (having T_g below room temperature and exhibiting large elastic deformation at room temperature) are only good photoelastic materials. Linear polymers of intermediate crystallinity (20 - 60%), exhibiting sufficient inelastic deformation at room temperature, would serve as good photoinelastic model material.

3.3 BIREFRINGENCE PHENOMENON

In polymers, birefringence is considered to arise out of macroscopic polarisability of molecules. The atomic groups that form the polymer chains are generally of different polarisability. The contribution made by those of predominantly high polarisability is most important. These atomic groups are called "optically sensitive" groups.

On a macroscopic level, the overall contribution made by the polymer chains depends largely on the orientation of the optically sensitive groups and any factor affecting their orientation influences the birefringence.

The works of Andrews and coworkers[25-28,48,49] indicate that the phenyl group, 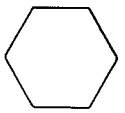 , and the ester (methyl) group 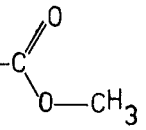 are of high polarisability, whereas the hydro-carbon group 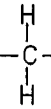 is far less sensitive. In Polystyrene, the polarisability of the chain is mainly contributed by the phenyl group. Above the glass transition temperature, the chains readily align with the direction of applied stress, with phenyl rings at transverse direction giving large negative birefringence. Below T_g and under small stress the chain mobility is negligible, the phenyl rings tend to align with stress direction resulting in small positive birefringence.

Steric hindrance to the optically sensitive groups caused by bulky groups, such as that of the methyl group on the phenyl ring in poly- α methyl-styrene, reduces birefringence. However, in polyphenyl methacrylate the phenyl ring is given more flexibility by two intermediate atoms separating it from the chain backbone. The former polymer exhibits small negative birefringence while the latter exhibits large positive birefringence[26].

On a larger scale, the contribution of a crystallized area to birefringence is larger than that of an amorphous area. Other factors affecting flexibility of the optically sensitive groups such as: molecular weight, copolymers,

hydrogen bonds of polar groups etc..., all influence birefringence.

3.4 PHOTOMECHANICAL BEHAVIOUR

The above considerations show that in general birefringence and deformation are related to different mechanisms of molecular chain motion. The deformation is related to overall chain motion whereas birefringence depends largely on the orientation of optically sensitive groups, whether they are on the main chain or they are side groups. Crystallized regions acting as cross-links tend to reduce the chain segment mobility but contribute more to the birefringence than the amorphous areas. The effects of steric hindrance on optically sensitive groups play a very important role in birefringence.

In a polymer where the optical sensitive groups form only a part of the main chain or are only side groups, the photomechanical behaviour with respect to stress and temperature is very complex. Such is the case with polystyrene[6,26]. In such a polymer the dielectric tensor or the index tensor cannot be expressed as a function of the total strain tensor alone (equation 2.5).

In polyethylene, the only atomic group is 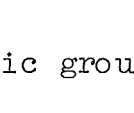 , the deformation and birefringent responses to temperature and stress are similar, thus the total strain tensor is

related to the index tensor and replaces the mechanical state tensor in equation (2.5)[5].

When deformation is accompanied by structural changes like crystallization, cross-linking, scission of primary bonds, abnormal photomechanical behaviour results[50].

The "stress" freezing phenomenon observed when a polymer undergoes a thermal cycle under loading can be explained as: in the temperature range in the vicinity of T_g, the chain mobility increases enormously, chain entanglements are drastically changed, resulting in irreversible deformation and orientation. The glass transition temperature is often called the annealing or "stress" freezing temperature. "Stress" freezing below T_g is possible or even desirable if deformation is to be kept small, just as annealing far above T_g is required if excessive birefringence had been introduced.

3.5 POLYCARBONATE OF BISPHENOL A

Polycarbonates are linear polyesters of carbonic acid with alipathic or aromatic dihydroxy compounds. The commercially available polycarbonate is prepared from bisphenol A with phosgene, the monomer unit of which is:

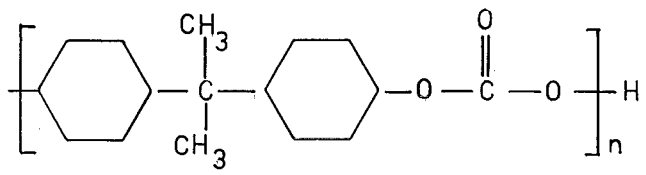

Polycarbonate of bisphenol A investigated here was obtained from Farbenfabriken Bayer under the trade name Makrolon and from General Electric Company under the name Lexan. Preparation, manufacturing processes and properties of polycarbonates are discussed in Mark and Gaylord[51], Christopher and Fox[52].

The two phenyl rings make the main chain relatively stiff, their rotation is also restricted by the two methyl groups. Polycarbonate of bisphenol A has high T_g (see Appendix 4), and high melt viscosity. Absence of strong polar groups indicates that polycarbonate does not readily crystallize.

Polycarbonate of bisphenol A is moderately crystalline (20% to 40%). The size of crystallites is small. "Cold drawing" does not increase crystallinity as evidenced by X-ray diffraction diagrams[52]. Crystallinity can be increased by slow evaporation of cast film or by heat aging: spherulites start to develop after eight days at 180° C. and full development could be obtained in the same period at 190° C.

From the molecular configuration of polycarbonate of bisphenol A, the optical sensitive groups are the phenyl rings and the carboxyl group $-O-\overset{\overset{O}{\|}}{C}-$. They make up most of the main chain.

At temperatures below T_g the chain mobility and the orientation of the optically sensitive groups are of the same order. When temperature approaches T_g, the chain mobility increases rapidly resulting in large deformation. The orientation of the phenyl rings is, however, restricted by the steric hindrance of the two methyl groups. Therefore, the birefringence does not increase as rapidly as the deformation. At room temperature the chain mobility can be increased by mechanical energy, the maximum strain is, however, not as large as that caused by high temperature.

Furthermore crystallinity is not increased by "cold drawing".

These observations suggest that in polycarbonate, the mechanisms of deformation and birefringence are intimately related. The total strain tensor ϵ_{ij} adequately represents the mechanical state tensor λ_{ij} in equation (2.5):

$$\eta_{ij} = (\eta_0 + a_0)\delta_{ij} + a_1 \epsilon_{ij} \qquad (4.1)$$

where coefficients a_0, a_1 are functions of temperature.

At a constant temperature and small changes of refractive index, equation (2.9) can be used:

$$N^{(1)} = \frac{c^2}{2v_0^3} a_1 (\epsilon_1' - \epsilon_2')$$

$$= c_\epsilon (\epsilon_1' - \epsilon_2') \qquad (4.2)$$

where c_ϵ, the strain-fringe coefficient is a function of temperature. At large deformation and temperatures close to T_g this first order approximation may not be satisfactory.

The above discussion also indicates that c_ϵ decreases with temperature because birefringence does not increase as rapidly as deformation does at high temperatures. At room temperature, c_ϵ may decrease slightly when extensive deformation occurs because of a similar reason.

3.6 CONCLUSION

A general consideration of the mechanisms of deformation and birefringence in terms of the molecular structure of polymers, indicates that the two responses are generally different under the application of stress and changes of temperature.

The deformation is related to the chain mobility as a whole, while the birefringence is related to the orientation of optically sensitive groups. Only when the optically sensitive groups form most of the chain backbone is the total strain tensor proportional to the index tensor, such as in the case of polyethylene, Nylon 6-6, Nylon 6-10[5,16].

For polymers of complex configuration like polystyrene, cellulose nitrate, polymethyl methacrylate (Appendix 4) the mechanical state tensor should be used in the photomechanical relationship.

The contribution of crystallized regions to birefringence is more substantial than that of the amorphous areas, but is less substantial to deformation. These considerations suggest that in polycarbonate of bisphenol A undergoing an isothermal deformation, the index tensor is proportional to the total strain tensor; the strain-fringe coefficient c_ϵ decreases when temperatures approach T_g and may also decrease slightly under large deformation at room temperature.

CHAPTER 4

THE MOIRÉ GRID ANALYSER METHOD FOR FINITE STRAIN ANALYSIS

4.1 INTRODUCTION

Prior to any experimental work in photomechanical relationships, a technique of analysing non-homogeneous finite strain in polymers has to be developed. It is appropriate at this stage to discuss the Moiré grid analyser method for the analysis of finite strain.

When a uniform finite strain field is studied, strain measurement techniques employing large gauge length can be used. When the strain field is non-homogeneous, and especially in regions of large strain gradient which are of most interest in post-elastic problems, small gauge lengths should be used. The grid technique has been used with success for very large strain, say above 25%. Electrical resistance strain gauges of high elongtion, up to 15% strain, are also available but are expensive and could be used only once in post-elastic analysis. When electrical resistance strain gauges are applied to polymers, problems are encountered because of the poor thermal conductivity of polymers and the adverse effects of cements. In the intermediate range of strain between 1% and 25%, the Moiré fringe technique has been recently used and is very suitable for finite strain analysis

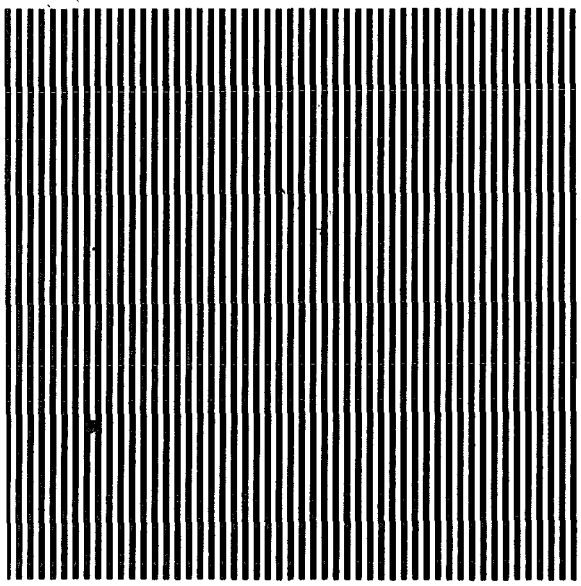

Fig. 4·1 GRATING GEOMETRY.

of polymers.

Moiré fringes result when two fine periodic patterns are superimposed. They can be fully described by the diffraction theory of light and have been used in various scientific and engineering fields[56-58]. A brief review of the terminology and the application of Moiré fringes in surface strain measurement is presented, followed by the development of the grid analyser method for finite strain analysis.

4.2 REVIEW OF THE METHOD OF STRAIN MEASUREMENT BY MOIRÉ FRINGES

a. Definition of general terms. The following definitions are presented to reduce confusion over the terminology.

In strain analysis the most commonly used pattern comprises straight, parallel, equidistant opaque bars separated by transparent bars. This pattern is called a grating. (Fig. 4.1).

The pitch g is the distance between corresponding points of adjacent bars of the same kind.

The frequency f is the inverse of the pitch, usually specified in "number of lines per inch", L.P.I.

A pattern consisting of two gratings oriented at an angle, usually 90°, is termed a grid.

Curvilinear gratings and grids, such as: concentric circles, radial lines, spirals, have also been used[59-61].

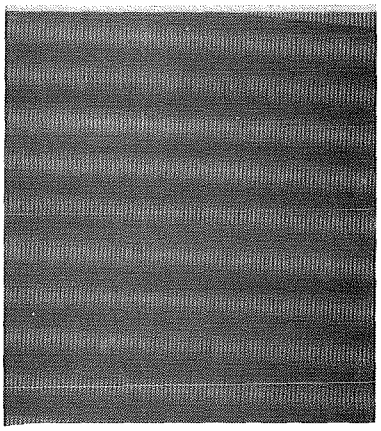

(a) Rotation

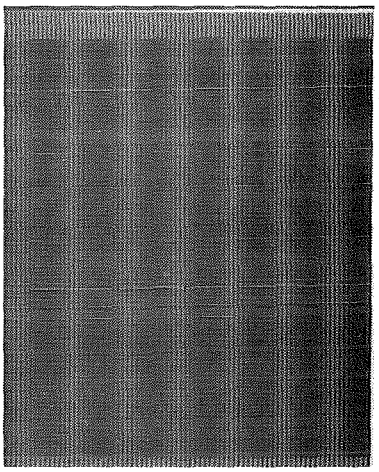

(b) Mismatch

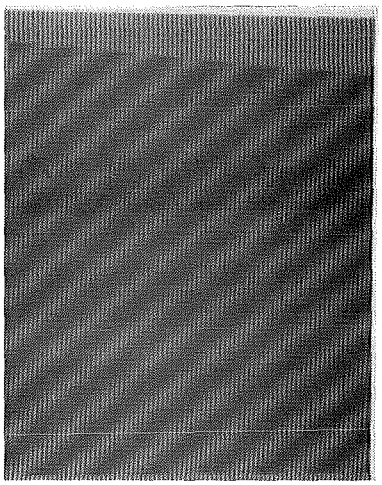

(c) Combination of rotation & mismatch.

Fig. 4·2 MOIRÉ FRINGES OF:-

For gratings employed in strain analysis, the frequency is usually less than 1000 L.P.I., Moiré patterns can be interpreted as "mechanical or geometric interference" of light propagation, i.e. assuming rectilinear propagation of light: the light is transmitted through transparent bars and obstructed by opaque bars. Diffraction effects modify only the intensity distribution but not the geometric relationship between grating (or grid) with Moiré fringes. The normal distance between two Moiré fringes is called the interfringe distance.

Consider two linear gratings. The Moiré fringes can be produced either by a difference in pitch, mismatch, or by a small relative rotation between the direction of gratings, misalignment, or by a combination of both. (Fig. 4.2). Consider one grating to be scribed onto the surface of the specimen in the undeformed state. This grating is called the specimen grating. On deformation, its pitch and grating direction will change, producing Moiré fringes when another grating is superimposed on the specimen grating. This grating is called the analyser or the master. Moiré fringes are thus related to two inherent characteristics of deformation: change in length and in direction.

b. Interpretation of Moiré fringes.

When there is no rigid body rotation between the original (undeformed) specimen grating direction and the analyser grating direction, Moiré fringes can be considered as the loci

of points undergoing a displacement of a multiple of g in the direction normal to the analyser grating, where g is the original pitch of the specimen grating.[62-64]

In a case of relative rotation or when the grating is curvilinear, it is more convenient to describe gratings by analytical functions and Moiré fringes by parametric equations or indicial equations.[60,65,66]

In strain analysis it is desirable to obtain distinct, sharp Moiré fringes. When such is the case, the index notation and the indicial equation outlined by Post[67] adequately interprets Moiré fringes. An elegant method to describe Moiré fringes by the covariant vector difference concept was given by Brombley[68].

c. Methods of analysis.

Experimental techniques of producing Moiré fringes are discussed in detail by Holister[69,70]. Most of published works on Moiré fringes have been devoted to small strain analysis and surface topography.

In surface strain analysis, the strain parameters can be found from the Moiré interfringe distance and fringe inclinations[62,71,72] or from partial derivatives of displacements, which are evaluated from Moiré fringes when there is no relative rotation between the analyser and the original specimen grating direction[63-65,73]. These techniques encounter practical difficulties: inaccurate determination of

interfringe distances and of fringe inclinations in a non-homogeneous strain field, susceptibility to error or the shear strain component, and in general the condition of zero relative rotation is not met.

A number of techniques have been employed to improve the accuracy in small strain measurements: measuring light intensity between Moiré fringes[74,75], grid shifting[65,76,77], fringe multiplication[78-80], increasing Moiré fringe density by employing small initial notation or mismatch[81,82].

Post[67] also employed large initial rotation and large mismatch for small strain problems and showed that by using orthogonal grids for both the specimen and the analyser, the strain parameters can be obtained from a single photograph of Moiré fringes and the susceptibility of shear strain to small rotation is eliminated. Post called his method the grid analyser method.

The analysis of finite strain by Moiré fringes has been discussed by Duffey and Mesmer[83], Martin and Ju[84].

The works presented here extend the grid analyser method to the analysis of finite strain in the case of arbitrary initial mismatch and initial rotation. A number of definitions frequently used in the grid analyser method are presented at the beginning of the next section.

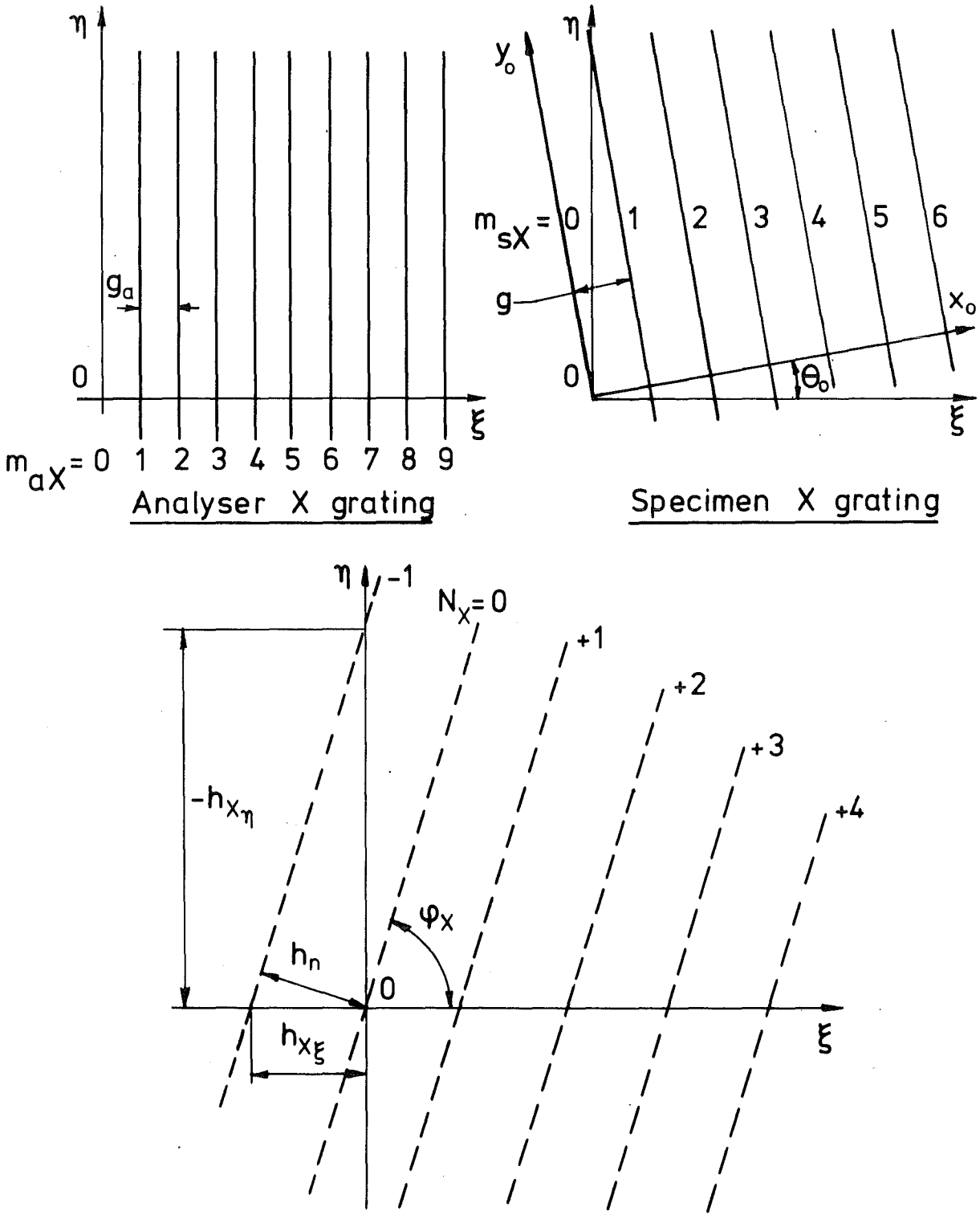

Fig. 4·3 MOIRÉ FRINGE FOR THE X GRATING

4.3 NOMENCLATURE

In the grid analyser method a grid consisting of two gratings at right angles is used for both the specimen and the analyser. (Figs. 4.3 and 4.4)

a. Grid directions.

Let the analyser grid directions be (ξ,η).

Let the undeformed specimen grid directions be (x_o, y_o) and the deformed specimen grid directions be (x,y).

b. Name of gratings and fringes.

The analyser grating at right angles to ξ and the specimen grating at right angles to x_o are called the X gratings.

Similarly the gratings normal to η and y_o are the Y gratings. The Moiré fringes produced by $\{^{X}_{Y}\}$ gratings are called the $\{^{X}_{Y}\}$ family.

c. Grating index and Fringe order.

The index notation and indicial equation. Firstly consider two gratings of the same kind. The bars of a grating are given an arbitrary integer index sequence, say increasing in the positive co-ordinate direction (Fig. 4.3). Let m_s, m_a be the index of the specimen and the analyser grating respectively.* Without loss of generality put m_s, $m_a = 0$

* Unless otherwise specified, subscripts s and a stand for specimen and analyser respectively.

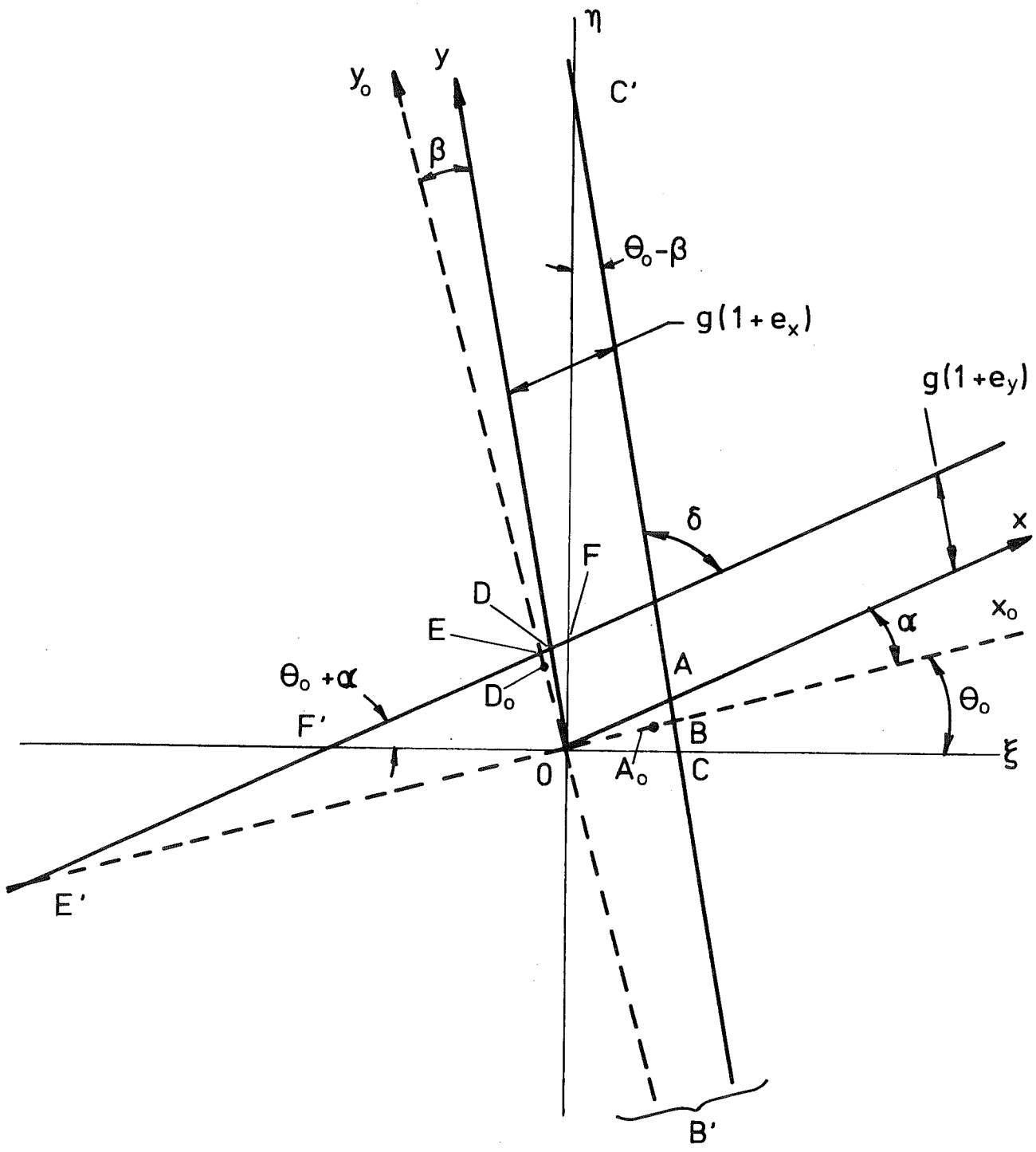
η
y
y_o
C'
β
$\theta_o-\beta$
$g(1+e_x)$
$g(1+e_y)$
δ
x
F
D
E
x_o
α
A
$\theta_o+\alpha$
D_o
θ_o
F'
B
ξ
0
A_o
C
E'
B'

Fig. 4·4

at the origin.

The primary Moiré fringe is the locus of points satisfying the indicial equation

$$N = m_a - m_s$$

where N is the order of the Moiré fringe.

In practice a grating consists of alternate opaque and transparent bars of finite width, however, in the geometric theory of light interference the opaque bars can be considered as lines of negligible width separated at a distance equal to the pitch, thus Moiré fringes shown in Fig. 4.3 are bright Moiré fringes.

Following the index notation, the analyser and specimen X gratings are given indices m_{aX}, m_{sX} respectively, and similarly indices m_{aY}, m_{sY} are assigned to the Y gratings.

The Indicial equation gives:

$$N_X = m_{aX} - m_{sX}$$
$$N_Y = m_{aY} - m_{sY} \qquad (4.1)$$

where N_X, N_Y are fringe orders of the X and Y families.

Without loss of generality put m_{aX}, m_{sX}, m_{aY}, m_{sY} equal to zero at the origin, giving N_X, N_Y = 0 at the origin.

d. Grid pitch.

Let g be the original specimen pitch

g_a be the analyser pitch.

The initial mismatch λ is defined by: $g_a = \frac{g}{1+\lambda}$ or $\lambda = \frac{g}{g_a} - 1$.

e. Angular relation.

Referring to the analyser grid directions ξ, η; x_o, y_o are at angle θ_o to ξ,η respectively. θ_o is called the initial rotation and is positive anticlockwise. x, y are at angles α, β relative to x_o, y_o respectively. According to conventional rule: α positive anticlockwise and β positive clockwise.

f. Fringe parameters.

The interfringe distance h_n is the normal distance between two fringes, h_n is always positive.

The fringe inclination of X, Y family with respect to ξ is ϕ_X, ϕ_Y respectively.

$$-\frac{\pi}{2} \leqslant \phi_X,\ \phi_Y \leqslant \frac{\pi}{2}$$

The fringe intercepts with an arbitrary axis are distances measured along the axis between two adjacent Moiré fringes, from one fringe to another fringe of next higher algebraic order, e.g. from $N_X = 0$ to $N_X = +1$, or $N_X = -2$ to $N_X = -1$. They are positive if the Moiré fringe orders increase in the positive direction of the axis.

To specify fringe intercepts, two subscripts are used:

* the first to indicate the Moiré family: X or Y
* the second to indicate the intercepting axis: e.g. ξ, η.

Similar interpretation and sign conventions apply to grating intercepts, except that three subscripts are used: the

first is used to indicate the analyser or the specimen grating (a or s), the other two have the same meanings as those of the fringe intercepts. For example from figs. 4.3 and 4.4:

$$h_{X\xi} > 0, \quad h_{X\eta} < 0$$

$$g_{aX\xi} > 0, \quad g_{sX\xi} > 0$$

$$g_{sX\eta} > 0, \quad g_{aX\eta} \to \infty$$

Fig. 4.4 is sketched for θ_o, α, $\beta > 0$. The following relations, however, are correct for any set of values α, β, θ_o if the sign conventions outlined above are taken into account.

When strain is zero, A and D coincide with A_o and D_o respectively.

$$OA = OA_o = OD = OD_o = g$$

Under strain, A_o moves to A, D_o moves to D,

$$OA = g_{sXx} = g(1 + e_x)$$

$$OD = g_{sYy} = g(1 + e_y)$$

$$OC = g_{sX\xi}, \quad OC' = g_{sX\eta}$$

$$OF = g_{sY\eta}, \quad OF' = -g_{sY\xi} \qquad \text{(A)}$$

$$OB = g_{sXx_o}, \quad OB' = -g_{sXy_o}$$

$$OE = g_{sYy_o}, \quad OE' = -g_{sYx_o}$$

$$\gamma = \alpha + \beta = \frac{\pi}{2} - \delta$$

where e_x, e_y, γ or γ_{xy} are Lagrangian "engineering" strains. These are discussed in Appendix 3.

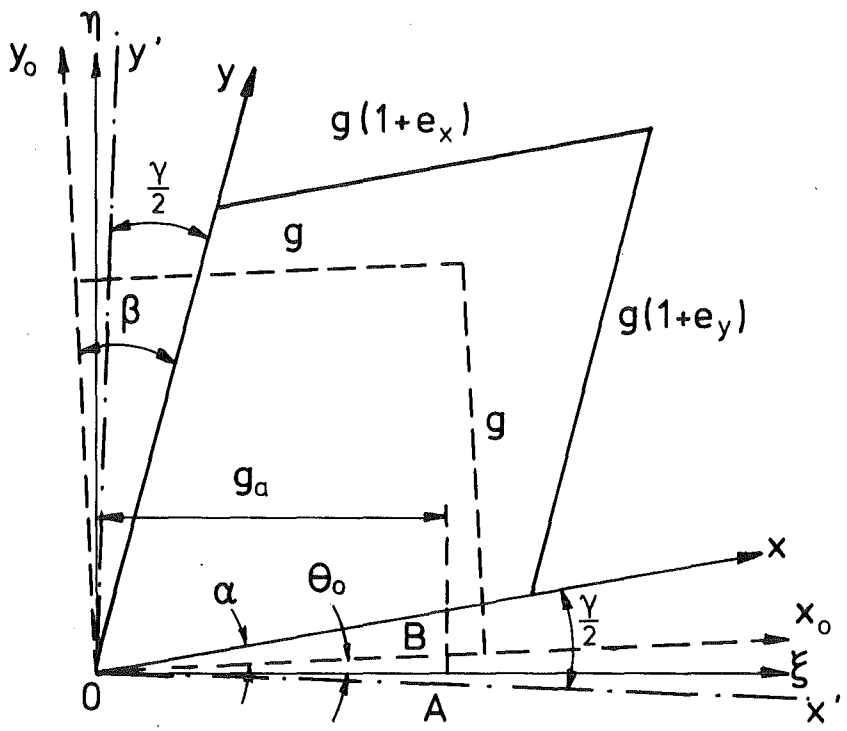
η
y_o
y'
y
$g(1+e_x)$
$\frac{\gamma}{2}$
g
β
$g(1+e_y)$
g
g_a
x
α
θ_o
$\frac{\gamma}{2}$
x_o
B
ξ
0
A
x'

Fig. 4·5

4.4 INTERPRETATION OF STRAIN

As the gratings of the specimen grid are originally at right angles, the Lagrangian engineering shear strain γ is directly related to the deformed specimen grid angle δ. Therefore the Moiré grid analyser method is suitably related to the Lagrangian engineering strains. The analysis given by Post[67] refers to axes x', y' at angle $\frac{\gamma}{2}$ to x, y respectively, (Fig. 4.5). For small strain x', y' can be considered as coincident to (x,y). However when strain is finite this approximation introduces large error and x', y' are not readily constructed.

The method presented here uses the Moiré fringe intercepts with grid analyser axes ξ, η to evaluate the Lagrangian engineering strains. Other strain descriptions can be found from these quantities as shown in Chapter 2 and Appendix 3.

4.5 INDICIAL EQUATIONS AND FRINGE INTERCEPTS

Assuming the strain field is homogeneous, the Moiré fringes of the same family are parallel and equidistant. The indicial equation (4.1) outlined in section 4.3.C is used.

Referring to any system of orthogonal axes (p,q) we have:

$$N_X \, h_{Xp} = m_{aX} \, g_{aXp} = m_{sX} \, g_{sXp}$$
$$N_X \, h_{Xq} = m_{aX} \, g_{aXq} = m_{sX} \, g_{sXq} \qquad (4.2)$$

i.e. at points of interception of Moiré fringes with an axis, p say, the co-ordinates can be expressed as a multiple of

fringe intercepts or a multiple of grating intercepts. Equation (4.2) can be readily verified for axis ξ and x_o in Fig. 4.3. Equation (4.1) and (4.2) give:

$$\frac{1}{h_{Xp}} = \frac{1}{g_{aXp}} - \frac{1}{g_{sXp}}$$

$$\frac{1}{h_{Xq}} = \frac{1}{g_{aXq}} - \frac{1}{g_{sXq}} \qquad (4.3)$$

Similar relations hold for the Y family.

Two convenient systems of orthogonal axes are (ξ,η) and (x_o,y_o); however, it was found that (ξ,η) is more useful.

4.6 LAGRANGIAN ENGINEERING STRAINS IN TERMS OF MOIRÉ FRINGE INTERCEPTS WITH ξ, η.

a. Homogeneous strain.

In equation (4.3) replace p, q by ξ, η and note that as $g_{aX\eta} \to \infty$ we have:

$$\frac{1}{h_{X\xi}} = \frac{1}{g_{aX\xi}} - \frac{1}{g_{sX\xi}}$$

$$\frac{1}{h_{X\eta}} = -\frac{1}{g_{sX\eta}} \qquad (3.4)$$

where $$g_{aX\xi} = g_a = \frac{g}{1+\lambda}$$

$g_{sX\xi}$ and $g_{sX\eta}$ can be obtained from Fig. 4.4 as follows:

* from triangle OAC.

$$\frac{OC}{\sin\delta} = \frac{OA}{\sin\left[\delta + (\alpha + \theta_o)\right]}$$

and by geometrical relations listed in (A):

$$g_{sX\xi} = \frac{g(1 + e_X)\cos\gamma}{\cos(\theta_o - \beta)}$$

* similarly from triangle OCC':

$$g_{sX\eta} = \frac{g(1 + e_X)\cos\gamma}{\sin(\theta_o - \beta)}$$

Substituting these relations into equation (4.4) we have:

$$\frac{1}{h_{X\xi}} = \frac{1}{g}\left[(1 + \lambda) - \frac{\cos(\theta_o - \beta)}{(1 + e_X)\cos\gamma}\right]$$

$$\frac{1}{h_{X\eta}} = \frac{-\sin(\theta_o - \beta)}{g(1 + e_X)\cos\gamma} \qquad (4.5)$$

giving

$$\tan(\theta_o - \beta) = \frac{-\frac{g}{h_{X\eta}}}{1 + \lambda - \frac{g}{h_{X\xi}}} \qquad (4.6)$$

and on eliminating $(\theta_o - \beta)$ using:

$$\sin^2(\theta_o - \beta) + \cos^2(\theta_o - \beta) = 1$$

we have:

$$(1 + e_X)^2 \cos^2\gamma\left[\left(\frac{g}{h_{X\eta}}\right)^2 + \left(1 + \lambda - \frac{g}{h_{X\xi}}\right)^2\right] = 1 \qquad (4.7)$$

Similar relations hold for the Y family where $(\theta_o + \alpha)$ and e_y replace $(\theta_o - \beta)$ and e_x respectively:

* from triangle ODF:

$$g_{sY\eta} = \frac{g(1 + e_y)\cos\gamma}{\cos(\theta_o + \alpha)}$$

* from triangle OFF':

$$g_{sY\xi} = \frac{-g(1 + e_y)\cos\gamma}{\sin(\theta_o + \alpha)}$$

giving:

$$\frac{1}{h_{Y\eta}} = \frac{1}{g}\left[1 + \lambda - \frac{\cos(\theta_o + \alpha)}{(1 + e_y)\cos\gamma}\right] \qquad (4.8)$$

$$\frac{1}{h_{Y\xi}} = \frac{\sin(\theta_o + \alpha)}{g(1 + e_y)\cos\gamma}$$

therefore:

$$\tan(\theta_o + \alpha) = \frac{\frac{g}{h_{Y\xi}}}{1 + \lambda - \frac{g}{h_{Y\eta}}} \qquad (4.9)$$

and:

$$(1 + e_y)^2 \cos^2\gamma \left[\left(\frac{g}{h_{Y\xi}}\right)^2 + \left(1 + \lambda - \frac{g}{h_{Y\eta}}\right)^2\right] = 1 \qquad (4.10)$$

From equation (4.6) and (4.9), $(\theta_o - \beta)$ and $(\theta_o + \alpha)$ can be found from fringe intercepts, giving:

$$\gamma = (\theta_o + \alpha) - (\theta_o - \beta) \qquad (4.11)$$

or using values of tan $(\theta_o + \alpha)$ and tan $(\theta_o - \beta)$ to evaluate tanγ :

$$\tan\gamma = \frac{\tan(\theta_o + \alpha) - \tan(\theta_o - \beta)}{1 + \tan(\theta_o + \alpha)\tan(\theta_o - \beta)} \qquad (4.12)$$

Equations (4.7), (4.10) and (4.11) show that the Lagrangian engineering strains e_x, e_y, γ can be evaluated in terms of the fringe intercepts $h_{X\xi}$, $h_{X\eta}$, $h_{Y\xi}$, $h_{Y\eta}$ independently of θ_o.

As a consequence, relative rotation between the specimen and the analyser is immaterial in the evaluation of strains. This conclusion is in agreement with Post[67] Martin and Ju[84].

Lagrangian and Eulerian finite strain tensors can be obtained from Lagrangian engineering strain quantities using equations (2.25) and (2.28) of Appendix 3.

b. Non homogeneous strain.

When the strain field is not homogeneous, the values e_x, e_y, γ vary and so do the fringe intercepts. They should be replaced by partial derivatives which are obtained by graphical or numerical differentiation, as follows:

$$\frac{1}{h_{X\xi}} = \frac{\partial N_X}{\partial \xi}, \quad \frac{1}{h_{X\eta}} = \frac{\partial N_X}{\partial \eta} \; ; \quad \frac{1}{h_{Y\xi}} = \frac{\partial N_Y}{\partial \xi}, \quad \frac{1}{h_{Y\eta}} = \frac{\partial N_Y}{\partial \eta}. \qquad (4.13)$$

Equations (4.5) to (4.12) have been derived for a case of finite strain and of arbitrary initial mismatch and initial

rotation and thus serve as a unified treatment of previous works on Moiré fringe strain analysis.

4.7 APPROXIMATION FOR SMALL STRAIN

a. Normal strains

From equation (4.7) we have:

$$(1+e_x)^2 = \frac{\sec^2\gamma}{\left\{1+\left[2\lambda+\lambda^2+\left(\frac{g}{h_{X\xi}}\right)^2+\left(\frac{g}{h_{X\eta}}\right)^2-2(1+\lambda)\frac{g}{h_{X\xi}}\right]\right\}} \qquad (4.14)$$

if γ is small and if the term in square bracket is small and is put as e':

$$\begin{aligned}(1+e_x)^2 &\simeq (1-\tfrac{\gamma^2}{2})^{-2}\ (1+e')^{-1}\\ &\simeq 1+\gamma^2-e'+e'^2\end{aligned} \qquad (4.15)$$

Furthermore if γ^2 is small compared to e' and if e'^2 is neglected:

$$\begin{aligned}e_x &\simeq -\frac{e'}{2}\\ &= -\lambda+(1+\lambda)\frac{g}{h_{X\xi}}-\tfrac{1}{2}\left[\lambda^2+\left(\frac{g}{h_{X\xi}}\right)^2+\left(\frac{g}{h_{X\eta}}\right)^2\right]\end{aligned} \qquad (4.16)$$

similarly

$$e_y = -\lambda+(1+\lambda)\frac{g}{h_{Y\eta}}-\tfrac{1}{2}\left[\lambda^2+\left(\frac{g}{h_{Y\eta}}\right)^2+\left(\frac{g}{h_{Y\xi}}\right)^2\right] \qquad (4.17)$$

These approximations are satisfactory only if:

* strains are small

* shear strain is small compared to normal strain

i.e. in directions close to principal strain directions.

b. Shear strain γ

By equations (4.6), (4.9) and (4.12):

$$\tan\gamma = \frac{(1+\lambda)\left[\frac{g}{h_{Y\xi}} + \frac{g}{h_{X\eta}}\right] - \left[\frac{g^2}{h_{X\xi}\,h_{Y\xi}} + \frac{g^2}{h_{X\eta}\,h_{Y\eta}}\right]}{(1+\lambda)^2 - (1+\lambda)\left[\frac{g}{h_{X\xi}} + \frac{g}{h_{Y\eta}}\right] + \left[\frac{g^2}{h_{X\xi}\,h_{Y\eta}} - \frac{g^2}{h_{X\eta}\,h_{Y\xi}}\right]} \qquad (4.18)$$

If second order of terms such as $\frac{g}{h_{Y\xi}}$ . . . can be neglected:

$$\tan\gamma \simeq \left(\frac{g}{h_{Y\xi}} + \frac{g}{h_{X\eta}}\right)\left\{1 + \left[\lambda - \left(\frac{g}{h_{X\xi}} + \frac{g}{h_{Y\eta}}\right)\right]\right\}^{-1} \qquad (4.19)$$

$$\simeq \left(\frac{g}{h_{Y\xi}} + \frac{g}{h_{X\eta}}\right)\left[1 - \lambda + \left(\frac{g}{h_{X\xi}} + \frac{g}{h_{Y\eta}}\right)\right] \qquad (4.20)$$

furthermore, if $\lambda - \left(\frac{g}{h_{X\xi}} + \frac{g}{h_{Y\eta}}\right) \ll 1$,

$$\tan\gamma \simeq \frac{g}{h_{X\eta}} + \frac{g}{h_{Y\xi}} \qquad (4.21)$$

Equations (4.16) and (4.21) are applicable only for small strains but are useful for the error analysis presented later. They resemble expressions derived by Post[67].

An example on the use of these approximation equations is given in Appendix 6.

4.8 INITIAL PATTERN OF MOIRÉ FRINGES - ZERO STRAIN

By studying effects of varying mismatch λ and initial rotation θ_o on the initial patterns we can derive useful properties of Moiré patterns. When strain is zero the initial Moiré pattern consists of two families of orthogonal, equispaced straight lines. They can be described by the fringe inclination with respect to ξ and the interfringe distance h_{ni}. (The subscript i stands for "initial".)

a. Fringe inclination with respect to ξ.

From Fig. 4.3 we have:

$$\tan \phi_{Xi} = \left[-\frac{h_{X\eta}}{h_{X\xi}} \right]_i \qquad (4.22)$$

In equation (4.5) put e_x, e_y, γ equal to zero and substitute values of $[h_{X\eta}]_i$ and $[h_{X\xi}]_i$ into equation (4.22):

$$\tan \phi_{Xi} = \frac{1 + \lambda - \cos \theta_o}{\sin \theta_o} \qquad (4.23)$$

similarly:

$$\tan \phi_{Yi} = \frac{-\sin \theta_o}{1 + \lambda - \cos \theta_o}$$

where $$-\frac{\pi}{2} \leqslant \begin{pmatrix} \phi_{Xi} \\ \phi_{Yi} \end{pmatrix} \leqslant \frac{\pi}{2}$$

Consider $\frac{\partial \phi_{Xi}}{\partial \lambda}$ and $\frac{\partial \phi_{Xi}}{\partial \theta_o}$:

$$\frac{\partial \phi_{Xi}}{\partial \lambda} = \cos^2 \phi_{Xi} \cdot \frac{1}{\sin \theta_o}$$

$$\frac{\partial \phi_{Xi}}{\partial \theta_o} = \frac{\cos^2 \phi_{Xi}}{\sin^2 \theta_o} [1 - (1 + \lambda) \cos \theta_o] \qquad (3.24)$$

i.e. $\frac{\partial \phi_{Xi}}{\partial \lambda}$ always has the same sign as θ_o but $\frac{\partial \phi_{Xi}}{\partial \theta_o}$ may be positive or negative depending on relative magnitudes of λ and θ_o.

If $\lambda \geq 0$, $(1 + \lambda - \cos \theta_o)$ is always ≥ 0, the relationship of ϕ_{Xi} and ϕ_{Yi} with θ_o are shown in Table 4.1.

b. Initial interfringe distance h_{ni}.

From Fig. 4.3:

$$\frac{1}{(h_{ni})^2} = \frac{1}{(h_{X\xi})_i^2} + \frac{1}{(h_{X\eta})_i^2}$$

$$= \frac{1}{g^2} [(1 + \lambda - \cos \theta_o)^2 + \sin^2 \theta_o] \qquad (4.25)$$

giving:

$$\frac{\partial h_{ni}}{\partial \theta_o} = g[(1 + \lambda - \cos \theta_o)^2 + \sin^2 \theta_o]^{-\frac{1}{2}} (1 + \lambda)(-\sin \theta_o)$$

$$\frac{\partial h_{ni}}{\partial \lambda} = g[(1 + \lambda - \cos \theta_o)^2 + \sin^2 \theta_o]^{-\frac{1}{2}} [-(1 + \lambda - \cos \theta_o)] \qquad (4.26)$$

In practice $|\lambda| < .30$ [66], thus $1 + \lambda > 0$.

However, when $\lambda < 0$, $1 + \lambda - \cos \theta_o$ may be positive, negative or zero.

Therefore: * $\frac{\partial h_{ni}}{\partial \theta_o}$ always has opposite sign to θ_o.

* if $\lambda > 0$, $\frac{\partial h_{ni}}{\partial \lambda}$ is always negative.

In general, for varying λ and θ_o, h_{ni} may increase or decrease. The relationships of fringe intercepts and fringe inclination with respect to θ_o for a constant $\lambda > 0$ is shown in Table 4.1. They are derived from equations (4.5), (4.8), (4.23), (4.25) and from above observations.

Table 4.1

θ_o	-	0	+
ϕ_{Xi}	-	$\frac{\pi}{2}$	+
ϕ_{Yi}	+	0	-
$[h_{X\xi}]_i$	+	h_{ni}	+
$[h_{X\eta}]_i$	+	∞	-
$[h_{Y\xi}]_i$	-	∞	+
$[h_{Y\eta}]_i$	+	h_{ni}	+

From Table 4.1 it can be seen that, if $\lambda > 0$

* $h_{X\xi}$, $h_{Y\eta}$, "<u>parallel intercepts</u>", are always positive.
* $h_{X\eta}$, $h_{Y\xi}$, "<u>cross intercepts</u>", have opposite sign to and same sign as θ_o, respectively.

c. <u>Determination of sign of θ_o by small analyser rotation</u>.

By equation (4.26) the sign of $\frac{\partial h_{ni}}{\partial \theta_o}$ is always opposite to that of θ_o. If the analyser is given a small anticlockwise

rotation (i.e. $\delta\theta_o < 0$):

* if $\theta_o > 0$, $\frac{\partial h_{ni}}{\partial \theta_o} < 0$ i.e. $\delta h_{ni} > 0 \rightarrow h_{ni}$ increases

* if $\theta_o < 0$, $\frac{\partial h_{ni}}{\partial \theta_o} > 0$ i.e. $\delta h_{ni} < 0 \rightarrow h_{ni}$ decreases

Opposite relations hold for a clockwise rotation of θ_o.

The procedure to determine the sign of θ_o is as follows:

Analyser rotation	Variation of h_{ni}	Sign of θ_o
anticlockwise	increase	+
	decrease	-
clockwise	increase	-
	decrease	+

Once the sign of θ_o is determined, correct signs of the cross fringe intercepts and the Moiré fringe family can be specified according to Table 4.1.

4.9 SUBSEQUENT MOIRÉ PATTERNS UNDER HOMOGENEOUS STRAIN

Under strains e_x, e_y, γ, the (x_o, y_o) axes are deformed into (x,y), giving effectively two new gratings:

* the X grating, of pitch $= g(1 + e_x)$ i.e. of mismatch λ_x, where:

$$\lambda_x = \frac{g(1 + e_x)}{g_a} - 1 = (1 + \lambda)(1 + e_x) - 1$$

$$\simeq \lambda + e_x \text{ for small } e_x, \lambda \qquad (4.27)$$

and at an orientation of:

$$\theta_X = \theta_o - \beta \text{ with respect to } \eta \qquad (4.28)$$

* similarly for the Y grating:

$$\lambda_Y = (1+\lambda)(1+e_y) - 1$$
$$\simeq \lambda + e_y \qquad (4.29)$$
$$\theta_Y = \theta_o + \alpha \text{ with respect to } \xi \qquad (4.30)$$

Therefore the X and Y Moiré fringe families follow the rules laid down for initial patterns with proper values of mismatch and rotation.

If λ is positive and substantially large so that $\lambda > |e_x|$ or $|e_y|$, then:

$$\lambda_X,\ \lambda_Y > 0$$

by equation (4.26) and considering variation of h_n with respect to λ alone,

* if normal strain is tensile: $\delta\lambda_X$ or $\delta\lambda_Y > 0$, h_n decreases

* if normal strain is compressive, h_n increases.

However, the overall change of h_n, ϕ_X, ϕ_Y is also affected by variation of θ_X, θ_Y i.e. by variation of θ_o, α, β.

Consider the case of the specimen being continuously deformed from a "strain free" condition; α, β always increase in magnitude and keep same sign. Possible changes of θ_X, θ_Y are listed in Table 4.2.

Table 4.2

	θ_o	+	-
α	+	$\theta_Y > 0$	$\lvert\alpha\rvert < \lvert\theta_o\rvert \rightarrow \theta_Y < 0$ $\lvert\alpha\rvert > \lvert\theta_o\rvert \rightarrow \theta_Y > 0$
	-	$\lvert\alpha\rvert < \theta_o \rightarrow \theta_Y > 0$ $\lvert\alpha\rvert > \theta_o \rightarrow \theta_Y < 0$	$\theta_Y < 0$
β	+	$\lvert\beta\rvert < \theta_o \rightarrow \theta_X > 0$ $\lvert\beta\rvert > \theta_o \rightarrow \theta_X < 0$	$\theta_X < 0$
	-	$\theta_X > 0$	$\lvert\beta\rvert < \lvert\theta_o\rvert \rightarrow \theta_X < 0$ $\lvert\beta\rvert > \lvert\theta_o\rvert \rightarrow \theta_X > 0$

From this table, signs of θ_X or θ_Y change when $\alpha = -\theta_o$ or $\beta = \theta_o$ (but not both as this implies $\gamma = (\theta_o - \alpha) - (\theta_o - \beta) = 0$).

At this instant, from consideration of fringe inclinations (Table 4.1), one fringe family becomes parallel to ξ or η and on further deformation it becomes more aligned with the other Moiré family.

This would pose two problems:

* confusion of two families if both are viewed or photographed at the same time.

* proper signs of cross fringe intercepts have to be accounted for.

To reduce magnitudes of α, β the specimen grid should be printed nearly parallel to the principal strain axes, however, this is not generally possible. Alternatively, θ_0 could be varied by rotating the analyser to ensure $|\theta_0|$ always greater than $|\alpha|$ and $|\beta|$, but a large θ_0 would make the fringes too dense. As shown by Post[67] the grid analyser method is susceptible to fringe confusion which may affect the accuracy obtainable by this method. Other essential factors affecting accuracy in determining fringe intercepts are also discussed in Appendix 5.

4.10 EXPERIMENTAL ERRORS IN DETERMINING THE FRINGE INTERCEPTS

The four essential steps in Moiré fringe analysis adopted here are:

a. producing Moiré fringes, by superimposing the analyser grid onto the specimen grid.

b. recording Moiré fringes, by photography.

c. reproducing Moiré fringes, by an optical system (Nikon shadow graph).

d. measuring fringe intercepts and evaluating strains.

In some cases steps a and b are reduced to photographing the specimen grid. The experimental procedures are described in a case study (Appendix 6). The error in part a is small if the grids are of high quality and photoengraving techniques are used for printing specimen grid. The photo-sensitive layer should be of sufficient resolution and of good bonding to the specimen surface when etching is not employed.

In part b errors may arise from:

* lens defects
* gap effect due to perspective
* analyser and camera plane not parallel
* uneven expansion or shrinkage in processing of negatives.

etc . . .

In part c the error may be due to the optical system. However, in the Nikon Shadow graph the negative is moved so that a reference point is on the optical axis of the optical system, and the distance traversed between any two reference points is measured by the micrometers and is thus not affected by lens defects.

Errors in part d may arise from:

* measurements of fringe intercepts, especially in locating the centre of fringes, where the accuracy depends on the sharpness, contrast of fringes and favourable fringe inclinations.
* estimation of partial derivatives such as $\frac{\partial N_X}{\partial \xi}$ where the strain field is not homogeneous.

The two types of errors are reduced by graphical plotting or numerical differentiation.

It can be seen that whenever an optical system is employed in Moiré fringe analysis it should be of high quality. With care, and by obtaining distinct fringes at favourable inclinations to ξ, η the error of the Moiré grid analyser technique is small as indicated by the case study.

4.11 ERROR ANALYSIS

Section (4.5) showed that strain parameters can be evaluated in terms of the fringe intercepts, the initial mismatch λ and the grid pitch g. The error in g can be included in the error in λ. Therefore, we need to investigate only effects of errors in λ and fringe intercepts on strains.

a. Error in value of λ : $\delta\lambda$.

* on normal strain.

The error is approximated by equation (4.16):

$$[\delta\epsilon_x]_\lambda \simeq -\delta\lambda\,(1 + \frac{g}{h_{X\xi}}) \qquad (4.40)$$

where $\frac{g}{h_{X\xi}}$ is usually small compared to unity.

The resulting absolute error in normal strain is approximately $-\delta\lambda$, therefore, when normal strains are small the relative error could be large. Values of mismatch should be determined accurately, and this suggests the use of a grid of high quality, preferably a master or a contact copy of the master.

* on shear strain.

Equation (4.20) gives:

$$[\delta \tan\gamma]_\lambda \simeq [\frac{g}{h_{Y\xi}} + \frac{g}{h_{X\eta}}]\ (-\delta\lambda) \qquad (4.41)$$

i.e. percentage error of strain is of order of $\delta\lambda$; shear strain is less sensitive to error in λ than normal strain.

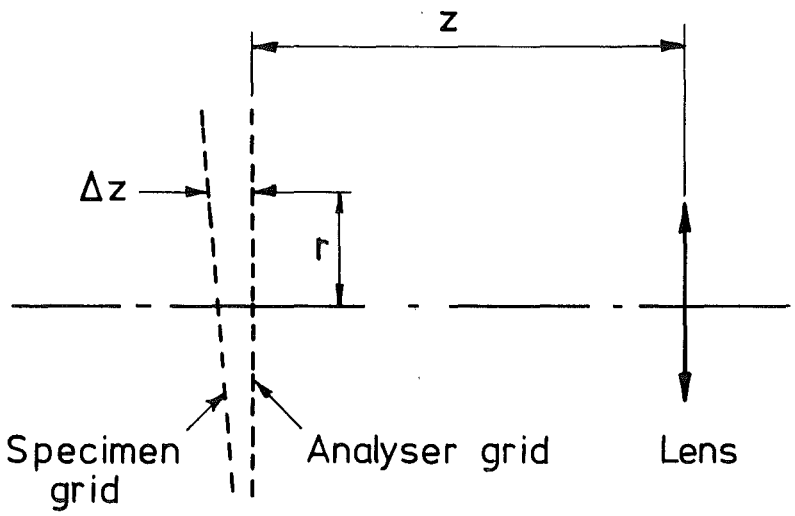

Fig. 4·6 GAP EFFECT

b. Error in fringe intercepts δh

Equations (4.16) and (4.21) give:

$$\left.\begin{aligned} [\delta e_x]_h &\simeq g(1+\lambda)\,\frac{\delta h}{h_{X\xi}} \\ [\delta \tan\gamma]_h &\simeq g\left(\frac{\delta h}{h_{X\eta}}+\frac{\delta h}{h_{Y\xi}}\right) = \delta h\left(\frac{g}{h_{X\eta}}+\frac{g}{h_{Y\xi}}\right) \end{aligned}\right\} \qquad (4.42)$$

as g is small, the absolute error in normal and shear strain due to δh is effectively reduced giving the relative error of the order δh, e.g.:

$$\frac{[\delta \tan\gamma]_h}{\tan\gamma} \simeq \delta h$$

Aside from errors in values of λ and fringe intercepts, there are two inherent errors in Moiré surface strain analysis: "gap effect" and neglect of displacement ω normal to the plane.

c. Gap effect.

Assume the analyser is nearer to the eye or the camera lens. If the analyser and the specimen are not in intimate contact, the perspective effect of the eye or of the camera lens makes the specimen pitch appear to be smaller, i.e. the gap effect is equivalent to a negative value of mismatch λ. The "fictitious strain" introduced by the gap effect can be shown to be[85]:

$$\epsilon_r = \frac{\Delta z}{z} + \left(\frac{r}{z}\right)\frac{\partial(\Delta z)}{\partial r} \qquad (4.43)$$

where (Fig. 4.6): ϵ_r = fictitious strain.

z = distance between analyser and camera lens

Δz = gap between specimen and analyser at the point considered

r = radial distance of the point to the optical axis of the camera lens.

It can be seen that it is essential to ensure intimate contact between the analyser and the specimen. When the displacement normal to the specimen surface is not uniform the analyser in fact rides on peaks, and the error due to the gap effect is unavoidable. The error is small if the camera lens is at a great distance from the specimen. Note that as the mismatch introduced by gap effect is negative, the resulting error is positive from equation (4.40).

d. Neglect of partial derivatives of **w** in strain expressions.

The error is illustrated by interpreting Moiré fringes as curves of constant displacement normal to the analyser grating (when there is no relative rotation between the analyser and the specimen)[63].

$$(1 + e_x)^2 = (1 + \frac{\partial u}{\partial x})^2 + (\frac{\partial v}{\partial x})^2 + (\frac{\partial w}{\partial x})^2 \qquad (4.44)$$

In techniques of Moiré surface strain measurement $(\frac{\partial w}{\partial x})$, $(\frac{\partial w}{\partial y})$ are not accounted for; the R.H.S. of (4.44) is thus reduced. (Moiré techniques to study surface topography do give these quantities).

The error in e_x due to neglect of $(\frac{\partial w}{\partial x})^2$ is approximately $-\frac{1}{2}(\frac{\partial w}{\partial x})^2$, i.e. it tends to reduce error due to gap effect.

4.12. CONCLUSION

Lagrangian engineering strains and hence Lagrangian and Eulerian finite strain tensors can be evaluated from Moiré fringe intercepts with grid analyser axes (ξ,η) independently of the angular relation between the analyser grid and the specimen grid.

The analyser can thus be rotated until a desirable Moiré pattern is obtained, i.e. of sharp contrast and with sufficient density fringes at favourable fringe inclinations to ξ and η. The mismatch λ can also be varied to obtain the desired Moiré pattern but its values should be accurately known.

Fringe confusion, mainly induced by shear strain, can be reduced by printing the specimen grid close to principal strain directions if possible. Alternatively, a single grating analyser which can be rotated through 90° exactly may be used; or two families separated and the contrast improved by "spatial filtering" as devised by Chiang[86], using high quality lenses to reduce errors introduced by the optical system used for filtering. Post's technique of aligning a long light source parallel to one fringe family to separate it from the other is not suitable for a non-homogeneous finite strain field, in which Moiré fringes change slopes drastically.

There is a possibility of using the analyser grid as a measuring scale of fringe intercepts when the ratios such as $\frac{h_{x\varepsilon}}{g}$ are large, eliminating any distortion introduced by the optical systems.

The Moiré grid analyser method presented is suitable for the intermediate range of strain covered by strain gauges and the grid method: between 1% and 25% strain.

CHAPTER 5

CHARACTERISATION TESTS IN UNIAXIAL TENSION

5.1 INTRODUCTION

The general photomechanical relationship can be investigated in two parts:

1) the relationship between the fringe order per unit optical path N and the difference of the secondary principal values of the mechanical state tensor λ_{ij}.

2) the relationship between the isoclinics and the secondary principal directions of λ_{ij}.

The investigation of the first part is presented here. The second part is discussed in the next chapter.

In the investigation of the first part of the photomechanical relationship, a mechanical state is chosen such that the stress and strain field are uniform and that the stress can be statically determined from loading and geometry of the test piece. These requirements are met in the uniaxial plane stress state.

The mechanical behaviour of polycarbonate of bisphenol A is also investigated in uniaxial stress for the purpose of stress analysis in biaxial stress state and for the purpose of evaluating polycarbonate of bisphenol A* as a model material.

* Referred to as polycarbonate from now on.

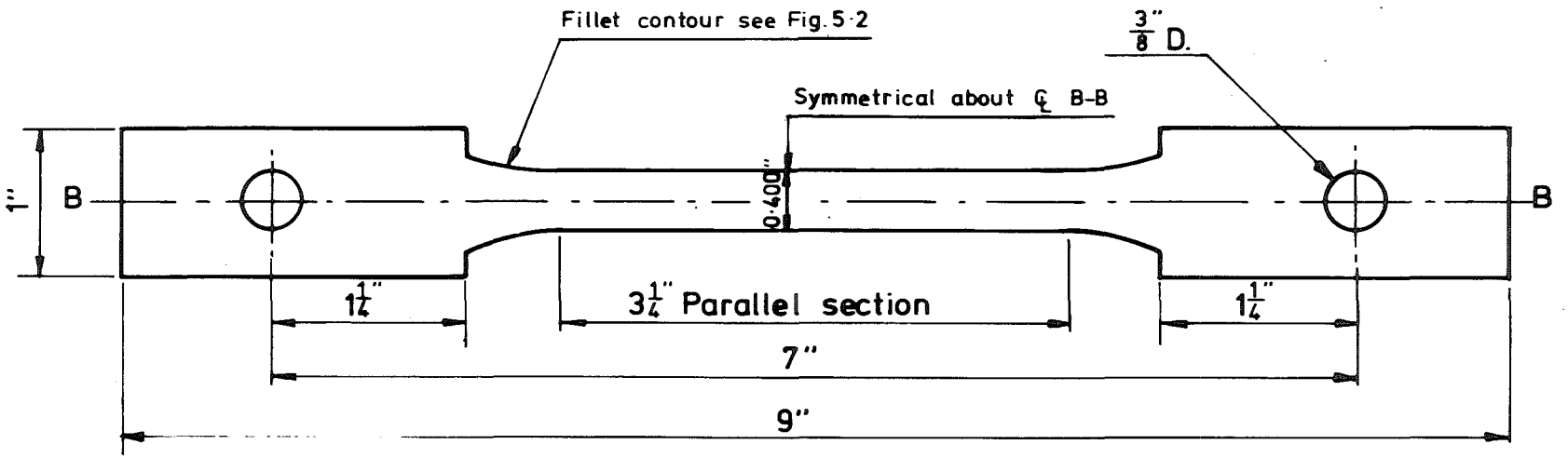

Fig. 5·1 TENSILE TEST PIECE

5.2 CHOICE OF CHARACTERISATION TESTS

Instability in the compression test, especially when post elastic behaviour is concerned, requires the test piece to be short and stubby which makes it difficult to realise plane stress condition and to obtain uniform stress field.
From the point of view of molecular structure, the chain segment mobility is not greatly affected by the sign of the stress. Tension tests, therefore, reflect the mechanical behaviour in compression. Uniaxial tensile tests also suffer instability but before this occurs, sufficiently large deformation has taken place. Plane stress condition and uniform stress field are easily obtained in tension.
Thus uniaxial tensile tests were selected for characterisation tests.

In linear viscoelastic materials, characterisation tests that are usually employed are: creep test, stress relaxation test, constant strain rate test and dynamic mechanical tests. The theory of linear viscoelasticity can be used to interrelate these tests and to relate them to a complex mechanical state [87-89]. The Boltzmann superposition principle can also be applied.
When glassy polymers undergo large deformation, the time dependence of deformation is usually non-linear with respect to the applied stress[90-91]. Constant strain rate, creep tests and stress relaxation tests are commonly used to characterise such

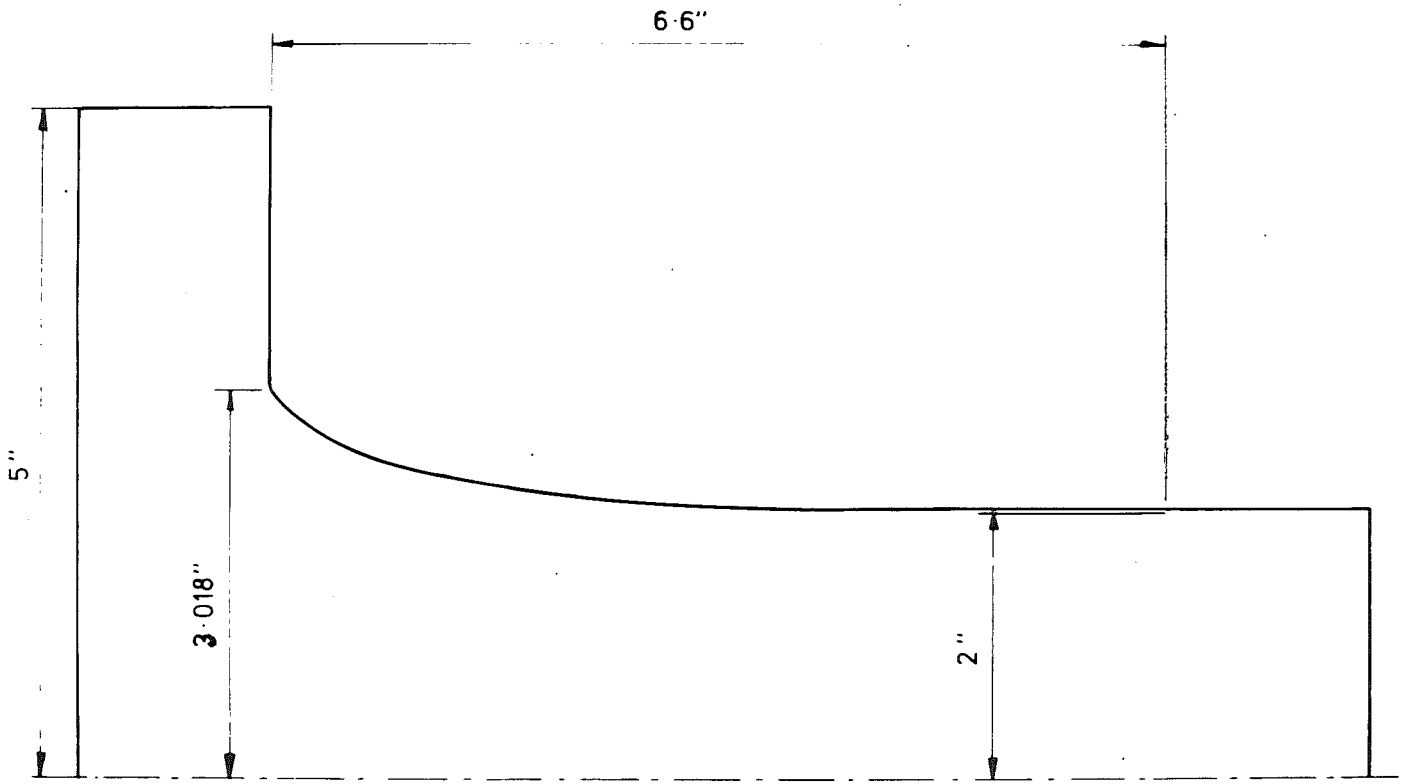

Scale 10 : 1

Fig. 5·2 OPTIMUM FILLET PROFILE

materials. The last two were used for polycarbonate.

It is not simple to differentiate between time-dependent and time-independent inelastic deformation in polymers even at room temperature because the ratio $\frac{T\,room}{T_g}$ of most polymers is large (approximately .69 for polycarbonate of bisphenol A). The role of thermal energy in chain mobility, hence the time dependent portion of deformation, is significant. Time dependence of deformation requires that the history of loading be known and data be recorded against time.

In creep test or stress relaxation test, a step imput of stress or strain is supposed to be applied.
In view of the fact that the time taken to reach full load in step imput creep and stress relaxation has not been standardised, tests are called creep test or stress relaxation test when the loading condition (stress or strain respectively) is constant with time, irrespective of the time taken to reach the full load condition.

5.3 MATERIAL

Polycarbonate of bisphenol A was obtained from Farbenfabriken Bayer in $\frac{1}{4}$" thick, 12" square compression moulded sheets under the trade name Makrolon. Similar sheets of $\frac{3}{16}$" thick was also supplied by Sharples Engineering Co. They will be referred to as Bayer Makrolon and Sharples Makrolon. Extruded sheets of .040" thick 24" × 48" size of the trade name

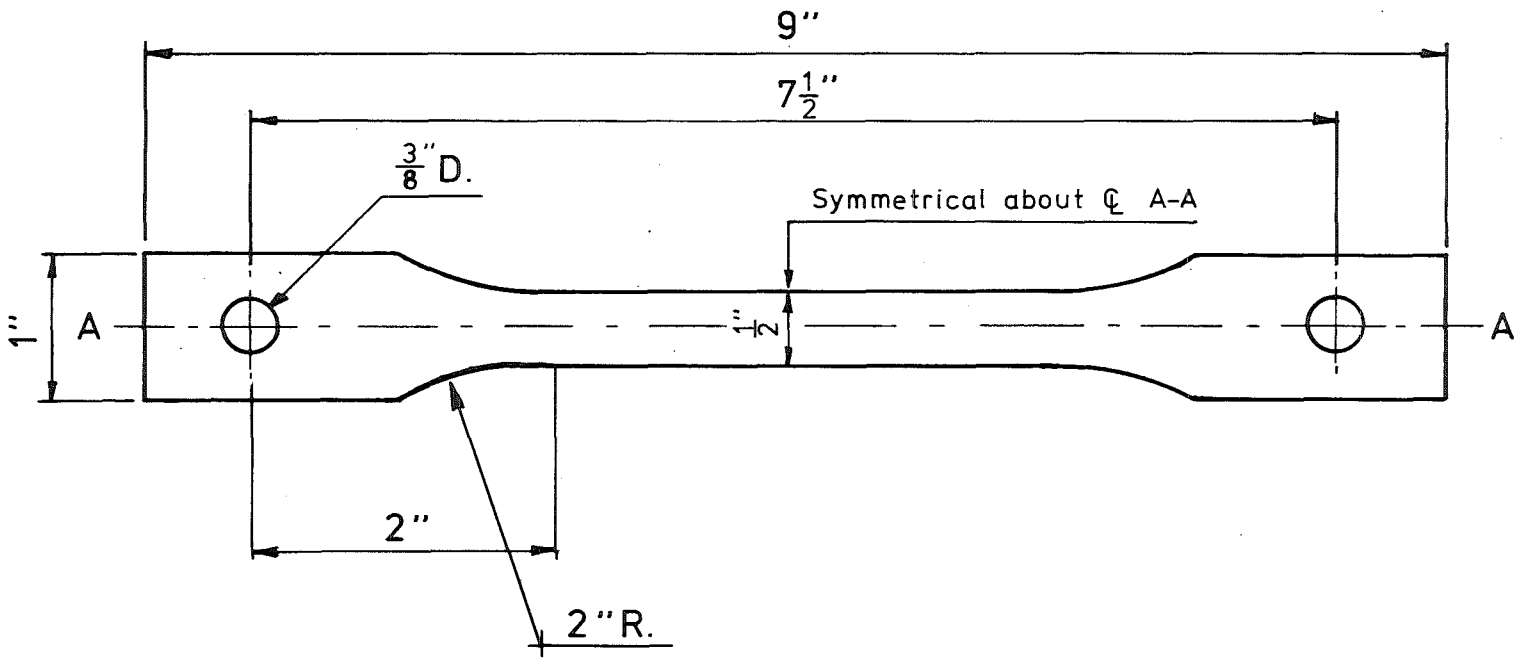

Fig. 5·3 MAKROLON CALIBRATION TEST PIECE

Lexan were obtained from General Electric Company. Lexan and Bayer Makrolon sheets were transparent. Some of Sharples Makrolon sheets required polishing and they were amber compared with water clear Lexan and bluish clear of Bayer Makrolon.

The compression moulded sheets exhibited very small residual birefringence and did not require annealing. A large area of the extruded Lexan sheets had large residual birefringence and only regions of residual fringe order 0 to 1 were used. Some sheets were annealed (150°C for 24 hours). The machining was done on a universal milling machine taking very light cut to avoid machining stress, or on a router using templates and spigots of decreasing diameters, so that final machining was in steps of .005". The edges were hand-dressed with fine grade emery paper.

Published properties of polycarbonate of bisphenol A are given in references 18, 51, 52, no strain rate or loading programme was mentioned and a tensile stress-strain curve with a sharp yield point was given. Preliminary tests indicated that at the nominal yield stress, deformation was concentrated to a small "slip band", the fringe pattern and strain distribution was non-uniform and rendered the establishment of a photomechanical relationship meaningless.

5.4. DESIGN OF TEST PIECE

The scarcity of the material influenced the design of the

test piece and choice of experiments to a great extent. In photoelasticity a calibration test piece is usually a simple tensile test piece having a parallel section with the radius of fillet small and a free square corner provided. When the inelastic behaviour of the material is investigated premature failure due to the stress (or strain) concentration at the fillet should be avoided.

Fillet contour free of stress concentration was designed by Lansard[92]; Heywood[21] also discussed some optimum fillet contours. A test piece having a fillet contour of Lansard's design was initially adopted (Figs. 5.1 and 5.2). The stress concentration due to the fillet revealed by the fringe pattern was very small. However, at high stress the local stress concentration due to tool marks along the parallel section and the fillet affects the uniformity of the fringe pattern in the shank and its symmetry in the transition region. As a tape controlled milling machine was not available, the Lansard fillet contour was very difficult to reproduce.
Because the stress concentration factor decreases with increasing inelasticity[10], a simple circular fillet contour having an elastic stress concentration factor of 1.112 was chosen (Fig. 5.3). It was found that a milling cutter of radius larger than 2" tended to leave high residual stress. This test piece did not have a free square corner, thus the fringe order had to be followed from the zero load condition.

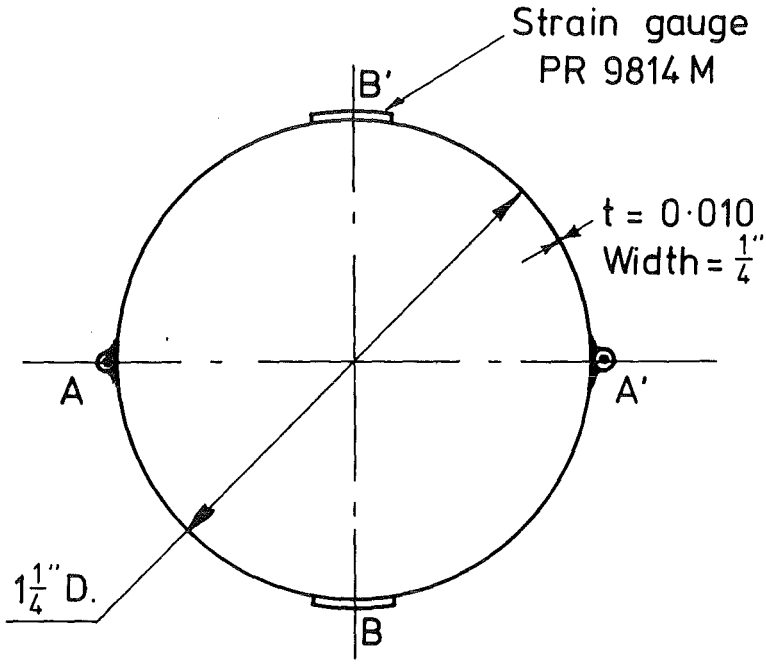

Fig.5·4 RING GAUGE

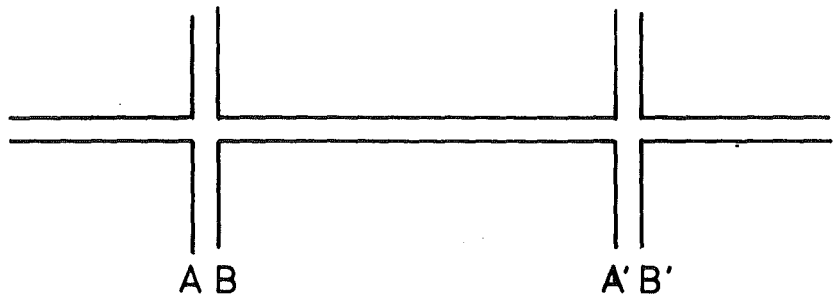

Fig. 5·5 IMAGE OF GAUGE MARKS ON THE SCREEN OF THE NIKON SHADOWGRAPH.

It was also found that symmetry of the fringe pattern was easily obtained when the fit between the hole and the pin was light press fit and the parallel section was symmetrical with respect to the centre line of the holes.

5.5 STRAIN MEASUREMENT

A number of techniques were employed to measure strain. The homogeneous strain field in the parallel section allows long gauge length to be used,

1. ring gauge: (Fig. 5.4)

Two pins AA' were diametrically soldered on a brass ring ($1\frac{1}{4}$" O.D., .010" thick). Two electric resistance strain gauges BB' were applied (circumferentially and diametrically opposed) at right angles to the diameter AA'. The ring gauge was clamped to the test piece with AA' on the centre line of the test piece. On pulling the ring gauge by pins AA', the strain registered by the strain gauges BB' was found proportional to the displacement of AA' (δ_A) i.e. proportional to the Lagrangian engineering strain $e_A = \frac{\delta_A}{AA'}$. The constant of proportionality m_R was of order $\frac{1}{20}$.
The constant m_R was found to be independent of clamping force on the pins. The ring gauge was used satisfactorily up to $e_A = .0650$. However, it was found that when the ring gauge was applied to the polycarbonate test piece, the clamping required to prevent slip of the pins affected the uniform fringe pattern of the parallel section. The ring gauge was used only

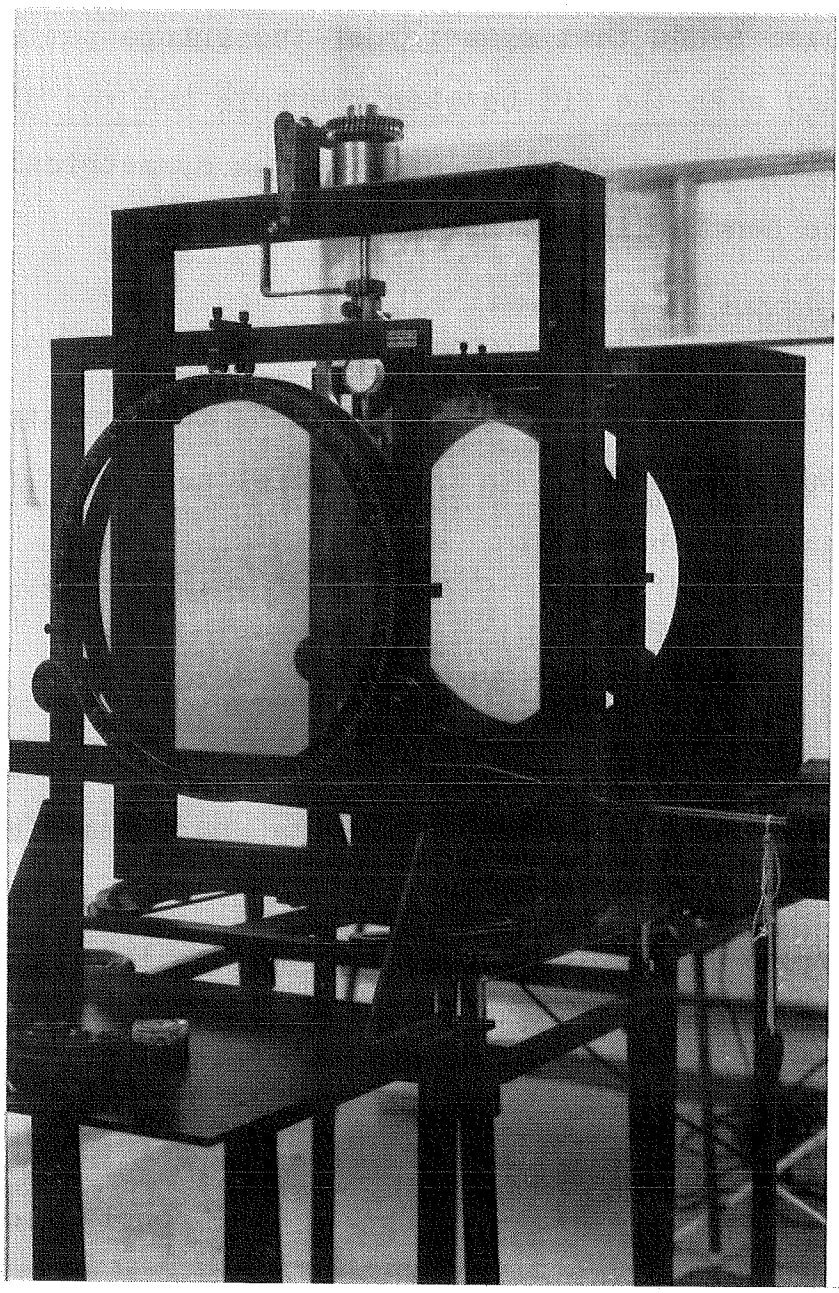

Fig. 5·6 (a) POLARISCOPE

in a few tests.

2. Cathetometers or travelling microscope.

Gauge lengths of approximately 8 cm were scribed onto the test pieces. The displacement of the gauge marks was measured either by two cathetometers or by a travelling microscope, all having a vernier of $\frac{1}{100}$ mm. Readings were reproducible within $\frac{2}{100}$ mm provided that the instruments were firmly supported.

While this method is accurate for strain above .0100 it was found to be somewhat tiring on the eyes.

3. by photography.

Gauge marks were scribed onto the test pieces. Photographs of the test piece were taken under the zero load condition and under subsequent deformation. A scale was used to account for any small change of the distance between the camera lens and the test piece. With careful processing and storage of the negative (20°C) and using thick estar base film (4" × 5" Kodak Plux-X Pan) the dimensional change of the film was insignificant. The negatives were later projected on the Nikon shadowgraph screen and the gauge length measured.

In measuring distances between gauge marks, the same side of the image of gauge marks was used: e.g. AA' or BB' (Fig. 5.5). This procedure would eliminate errors due to variation in width of image of gauge marks by deformation or by variation in exposing and developing the negatives. At least three readings

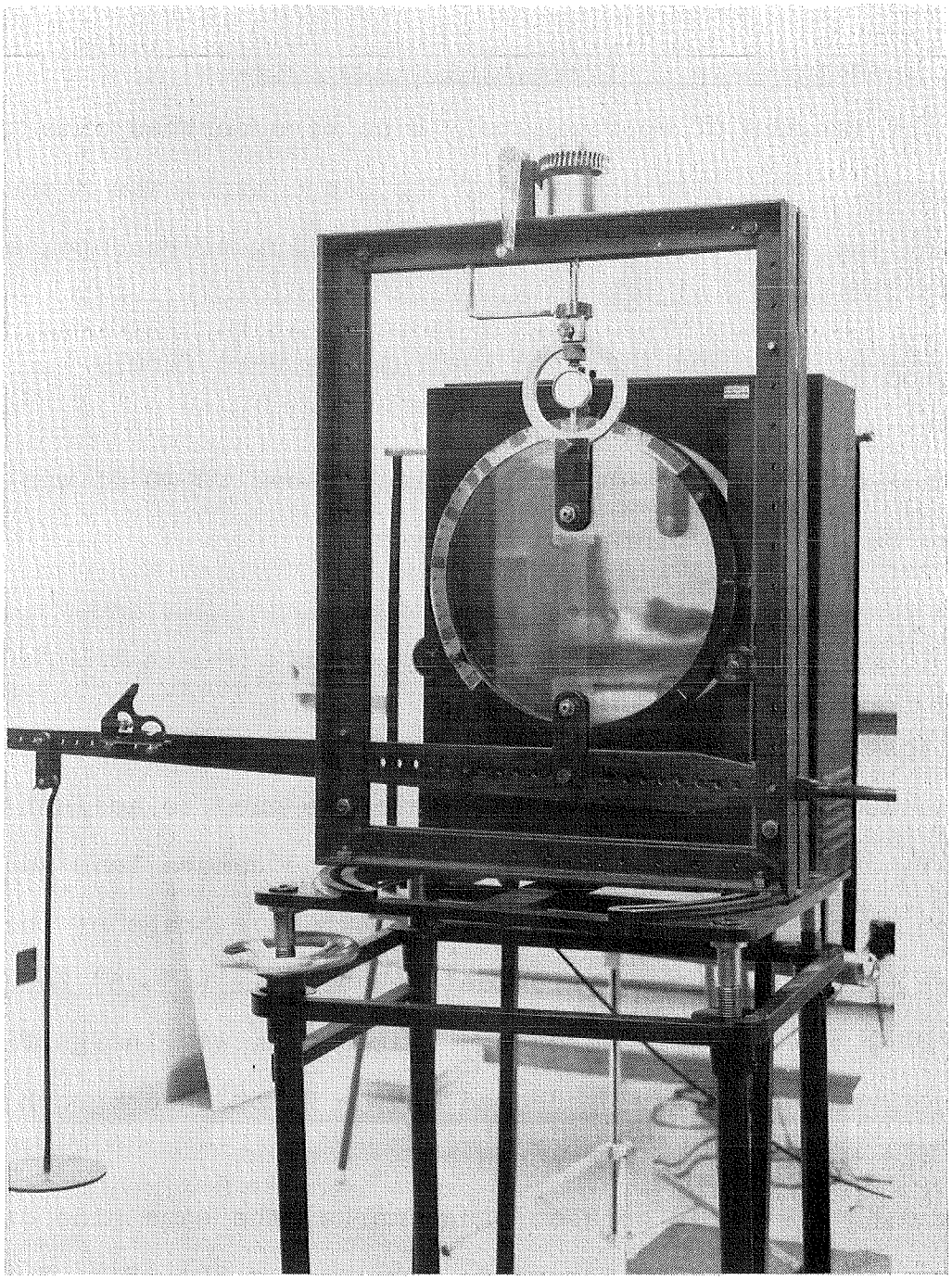

Fig. 5·6 (b) LOADING FRAME.

were taken for each reference line, the deviation from the mean reading was always less than 2×10^{-4} in.
This method was particularly useful in strain freezing experiments during which the test piece was kept at around 150°C.

4. by Moiré fringe method.

The Moiré fringe method presented in Chapter 4 was also employed in this homogeneous strain case, especially when transverse strain was required. The Moiré fringe was photographed and analysed as outlined in Appendix 7. The Vina-top resist was found to adhere to polycarbonate, even in the necking region. A violet dye (methyl violet) was used to increase the contrast of the Moiré fringes. Otherwise the specimen grid was photographed with high contrast film (Kodaklith ortho or Kodaklith Royal ortho) and Moiré fringes were produced later by superimposing the analyser grid onto the image of specimen grid (negative) on the table of the Nikon shadowgraph.

Photographs were taken by a Linhoff Kardan-color 4" × 5" camera with a 150 mm Symmar lens.

STRAIN MEASURE USED. Various strain descriptions are presented in Appendix 3. In a photomechanical relationship the principal strain difference $(\epsilon_1 - \epsilon_2)$ (normal incidence) is of more importance than either ϵ_1 or ϵ_2*. In tensile tests $(\epsilon_1 - \epsilon_2)$ does not vary much with different strain description.

* ϵ_1 is the axial strain, ϵ_2 is the transverse strain.

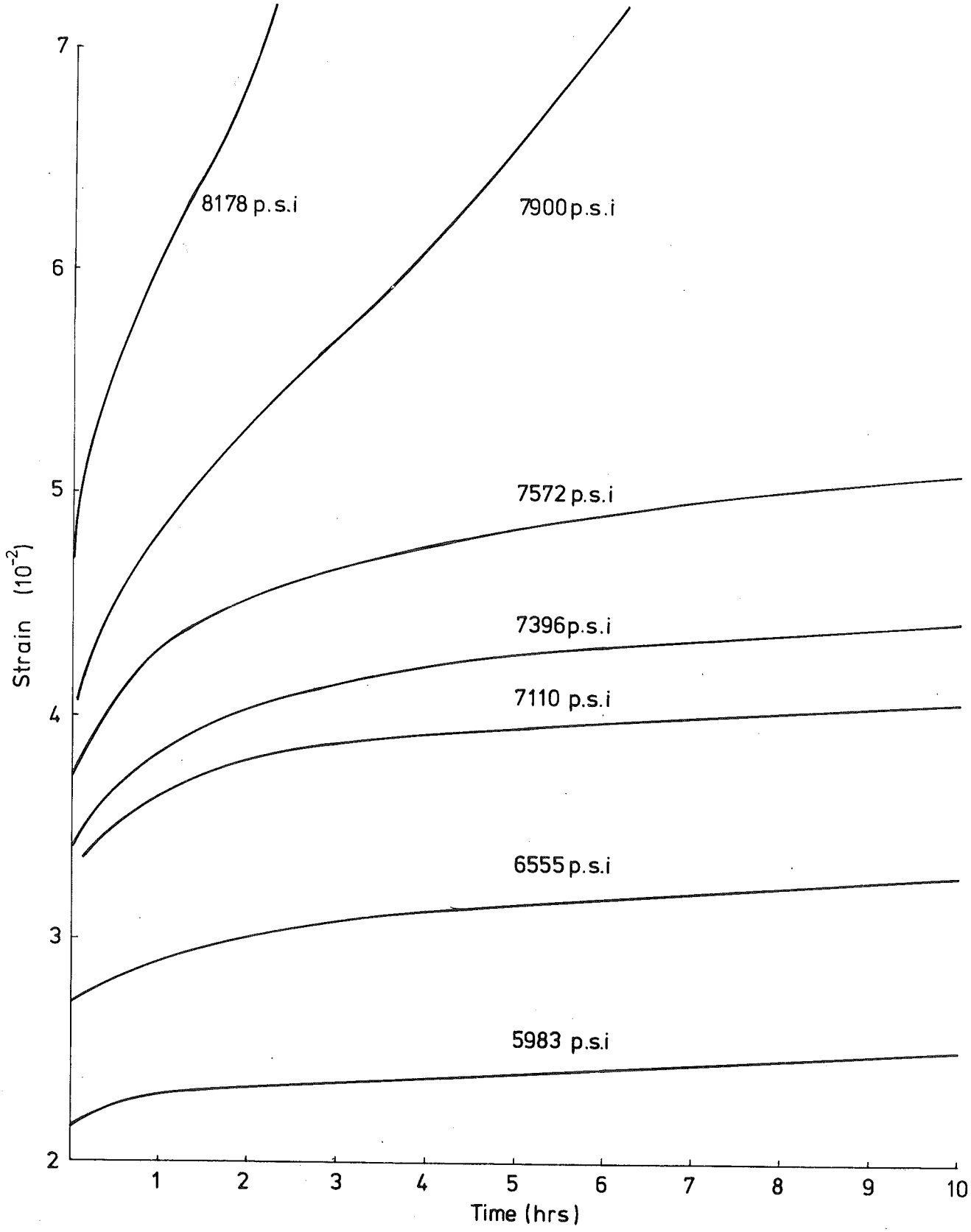

Fig.5·7 STRAIN CREEP

For purpose of stress analysis in incompressible material natural or logarithmic strain is preferable. Seth[43] also showed that this strain measure is a compromise between Lagrangian finite strain tensor and Eulerian finite strain tensor. For $-.1000 < e < .1000$ it can be shown that the corresponding $\epsilon^N = \log(1 + e)$ is always algebraically smaller than e. The maximum error in this range is 5%. Therefore, the error in $(e_1 - e_2)$ is much smaller

e.g. $e_1 = .1000 \quad \epsilon_1^N = .0953$

$e_2 = -.0500 \quad \epsilon_2^N = -.0513$

$\therefore \; e_1 - e_2 = .1500 \quad \epsilon_1^N - \epsilon_2^N = .1466$

error = 2.3%

Preliminary tests indicated that in tensile tests without necking, the range of axial strain e_1 is within .1000. Therefore, Lagrangian engineering strains were used to report test results, with ϵ_1, ϵ_2 replacing e_1, e_2.

5.6 EXPERIMENTAL METHODS AND APPARATUS

The tensile test piece was loaded in the loading frame of a diffused light polariscope at constant temperature 20°C, the relative humidity was 45% to 55%.

a. The polariscope (Fig. 5.6(a)).

The polariscope had a white light source and a "blue" light source which gave monochromatic green light when a Kodak

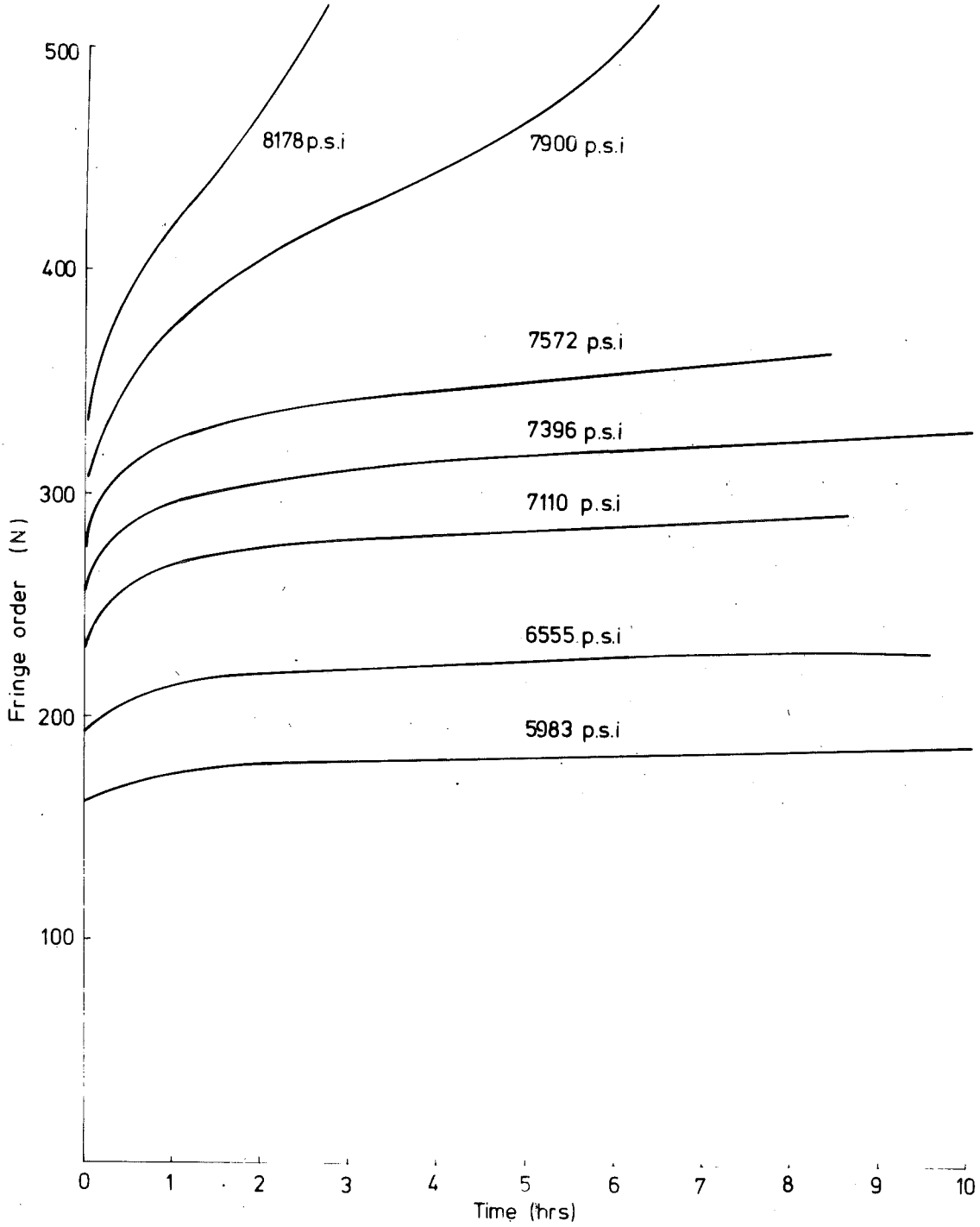

Fig 5·8 FRINGE CREEP

Wratten 77 filter was used. The polariser P and the first quarter wave plate Q_1 together with the light box were mounted on a transportable table. This arrangement permits the polariscope to be arranged on two sides of the "stress" freezing oven for birefringence studies. The polariscope had a $16\frac{1}{2}$" diameter field.

b. The loading frame (Fig. 5.6)

The loading frame was fixed to the base of a rigid frame and the base could be raised or lowered by a chain-sprocket arrangement. A loading beam with an arm length 60" was pin jointed through a roller bearing to one side of the loading frame and this could also be pin jointed to the other side of the loading frame in stress relaxation tests.

A hand driven worm gear was provided to strain the test piece in stress relaxation tests and to level the loading beam in creep tests.

c. Loading

The test piece was bolted between serrated circular grips housed in loading forks with the upper fork and lower fork pin jointed to a proving ring (5000 lbs capacity) and to the loading team respectively.

No premature failure at the holes of the test piece was found.

d. Fringe order

For a thickness of $\frac{1}{4}$" the fringe order observed in some

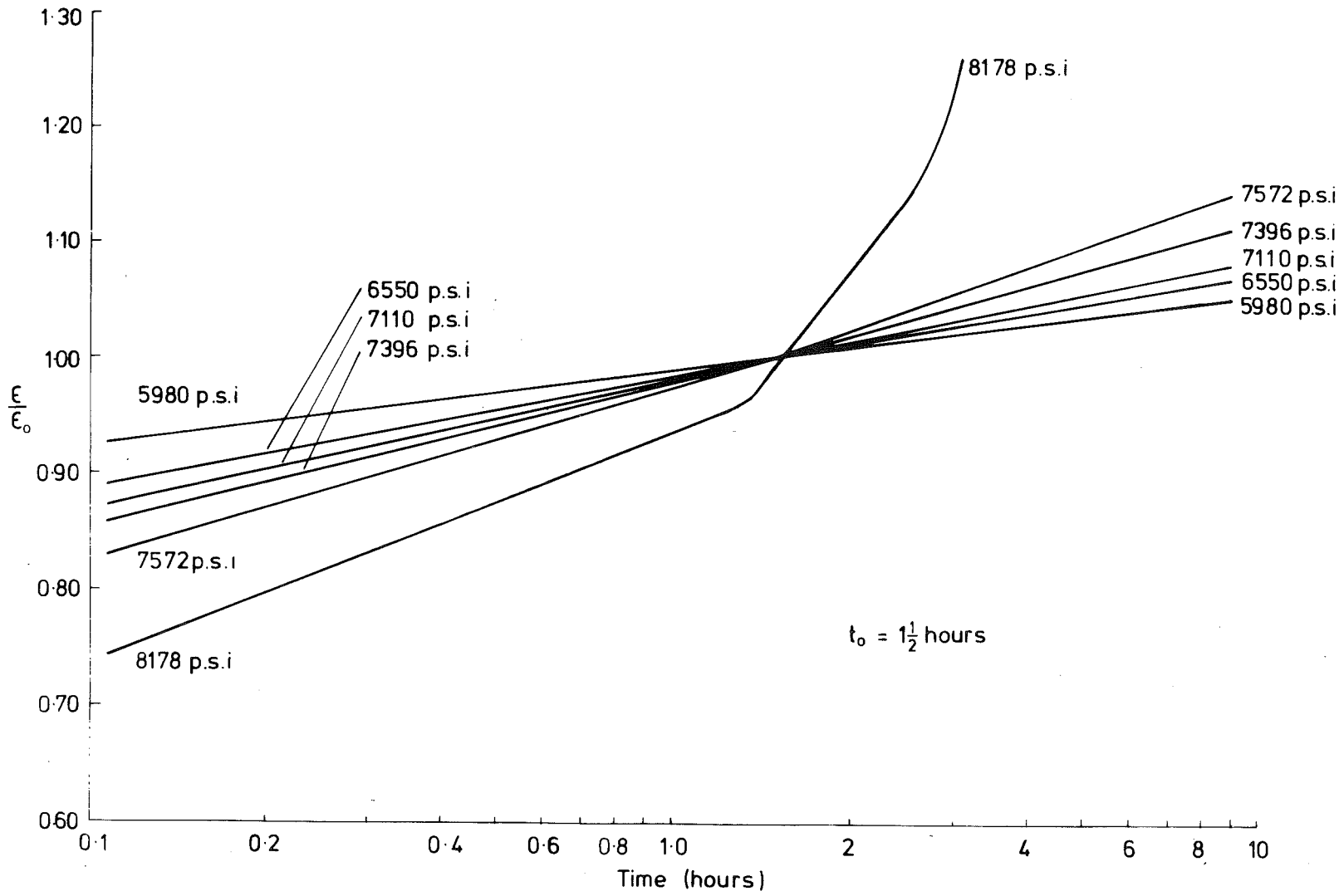

Fig. 5·9 NORMALIZED STRAIN CREEP

experiments exceeded 100, the use of a compensation strip or a Babinet-Soleil compensation was not practical. The fringe order was observed from the zero load condition, thus the integral fringe order was determined. In the case of .040" sheet, a compensation strip of fringe order 24 was used. The fractional fringe order was obtained by Tardy's method of compensation. In calculating N the current thickness h was measured or considered to be:

$$h = h_0 (1 + \epsilon_2)$$

$$\simeq h_0 (1 - \tfrac{1}{2}\epsilon_1)$$

5.7 CREEP TESTS

5.7.1 Loading programme.

Preliminary creep tests showed that at stress levels up to 3300 psi, no substantial strain creep and fringe creep was observed. The loading rate therefore does not affect the strain and fringe response below this stress level. Above this stress level the load was increased in steps of approximately 800 psi for a duration of 2 minutes. During this time interval the fractional fringe order was determined and a photograph of the test piece taken if required.

The time taken to complete loading, therefore, increases with stress level. Reference time was chosen at the instant of loading being completed.

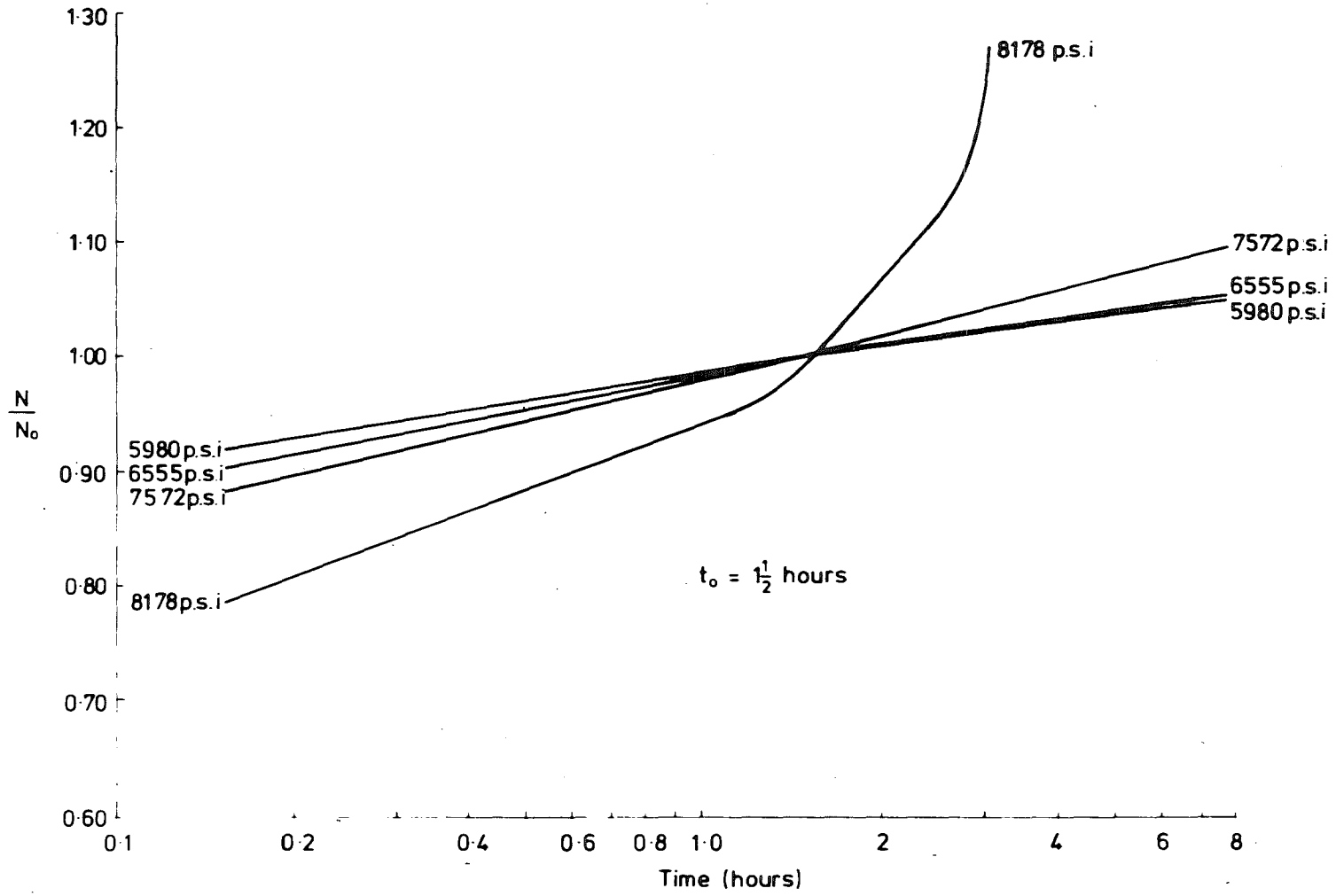

Fig. 5·10 NORMALIZED FRINGE CREEP

The insensitivity of strain and fringe with respect to time at stresses below 3300 psi permits adjustment to be made at the beginning of the loading programme, to ensure centering of the test piece and uniform and symmetrical fringe pattern in the parallel and transition section of the test piece respectively.

5.7.2 Choice of stress levels.

The fringe creep was also found to be very small at 5000 psi (5% of initial value after 72 hours). Published "tensile strength" of polycarbonate is of order 9000 - 10,000 psi; preliminary tests in the Hounsfield tensometer showed that tensile test pieces failed at about 9000 psi. The range of stress investigated in creep tests was thus chosen to be from 5000 psi to 8100 psi. It should be noted that creep tests conducted here are constant load tests, the stress quoted was based on initial area.

It was found that at stresses above 8200 psi failure occurred after too short a period to allow birefringence data to be recorded.

5.7.3 The concept of Normalized creep curves.

Cloud[19] observed that the absolute fringe order is more sensitive to the test procedure and conditions of the test piece than the amount of optical and mechanical creep i.e. fringe and strain creep. Cloud subsequently suggested the concept of

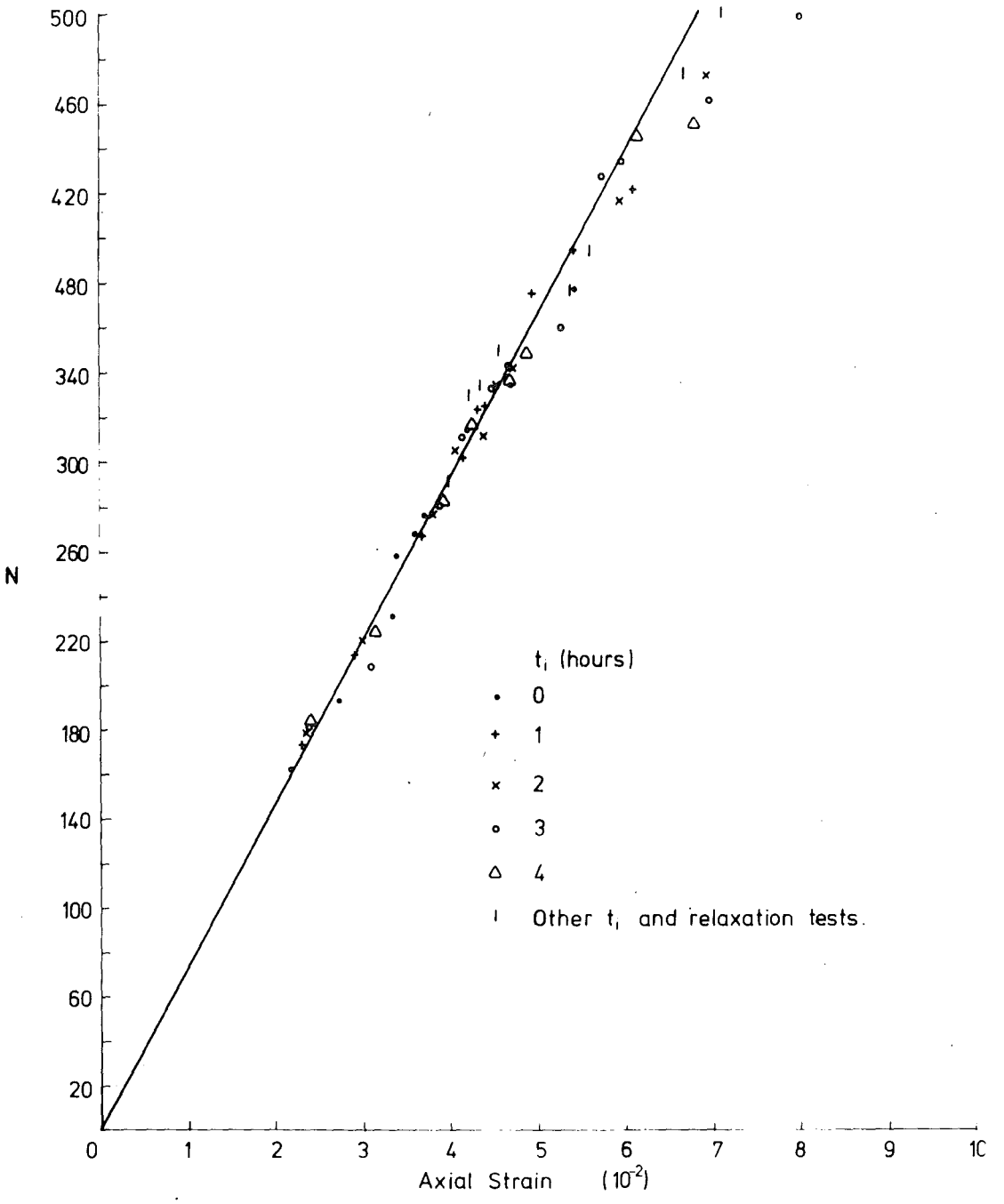

Fig. 5·11 FRINGE ORDER — AXIAL STRAIN FROM CREEP TESTS.

"normalized optical creep" defined by:

$$\Omega(t) = \frac{R(\lambda_o, t)}{R(\lambda_o, t_o)} = \frac{N(\lambda_o, t)}{N(\lambda_o, t_o)}$$

where $\Omega(t)$ = normalized optical creep.

R = relative retardation.

N = fringe order per unit optical path.

λ_o = wavelength in vacuo of observing light.

t_o = an arbitrary reference time.

Similarly, "normalized mechanical creep" $\exists(t)$ is defined as:

$$\exists(t) = \frac{\epsilon(\sigma_o, t)}{\epsilon(\sigma_o, t_o)}$$

where $\epsilon(\sigma_o, t)$ = strain at time t in a creep test at stress level σ_o.

$\epsilon(\sigma_o, t_o)$ = strain at time t_o in the same creep test.

In this study t_o was chosen to be $1\frac{1}{2}$ hour. The primary stage of most creep curves took place within this time.

The concept of normalized creep curves also reduces effects of errors in readings of strain and fringe order in the primary creep stage.

Furthermore it provides a means to determine whether the behaviour of the material is linear viscoelastic; a linear viscoelastic material has creep curve of the form:

$$\epsilon(t) = \sigma f(t)$$

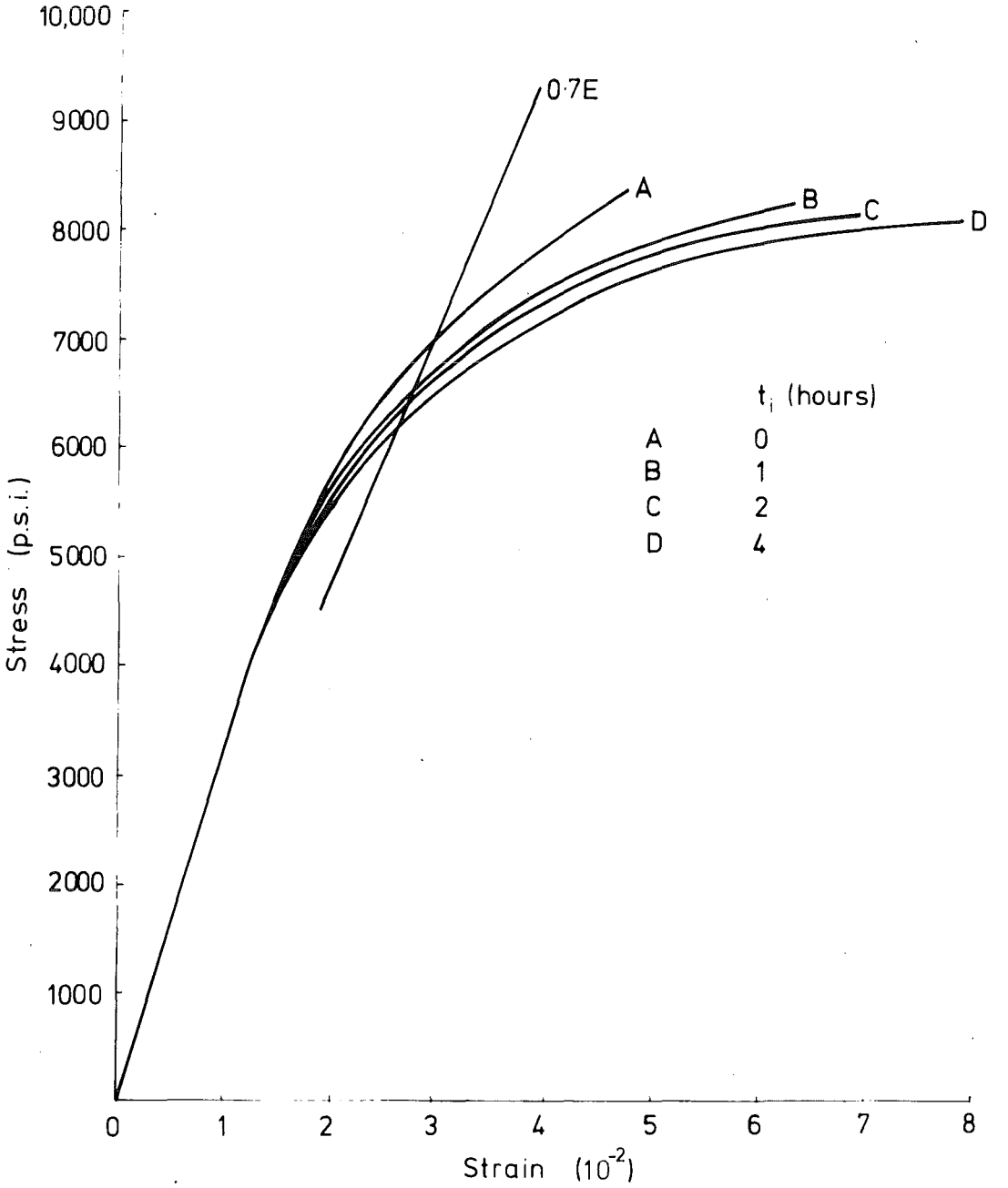

Fig. 5·12 ISOCHRONOUS STRESS STRAIN CURVES FROM CREEP TESTS.

therefore: $$\exists(t) = \frac{\sigma f(t)}{\sigma f(t_o)} = \frac{f(t)}{f(t_o)}$$

i.e. the normalised strain creep is only a function of time, independent of the stress.

5.7.4 Results of creep tests.

The strain creep and fringe creep curves and their normalised curves are plotted in Figs. 5.7 - 5.10.

The creep curves can be roughly divided into the primary, secondary and tertiary stages, similar to high temperature creep curves of metals. Within the 10 hours duration no tertiary stage was observed for stresses lower than 7700 psi. Some tests were continued for a longer period but it was found that after about 10 hours crazy cracks and tool marks affect greatly the uniform fringe pattern in the parallel section. As both strain and fringe order were of interest, readings beyond 10 hours are not reported.

At high stress and for completed loading the fringe order increases very rapidly. Because the integral fringe order had to be followed at normal incidence, no strain reading was taken until the rate of fringe creep was slow enough to permit the photography or the measurement of gauge length completed without missing an increase of the integral fringe order.

The strain and fringe creep curves resemble each other; the resemblance is clearly shown in their normalised creep

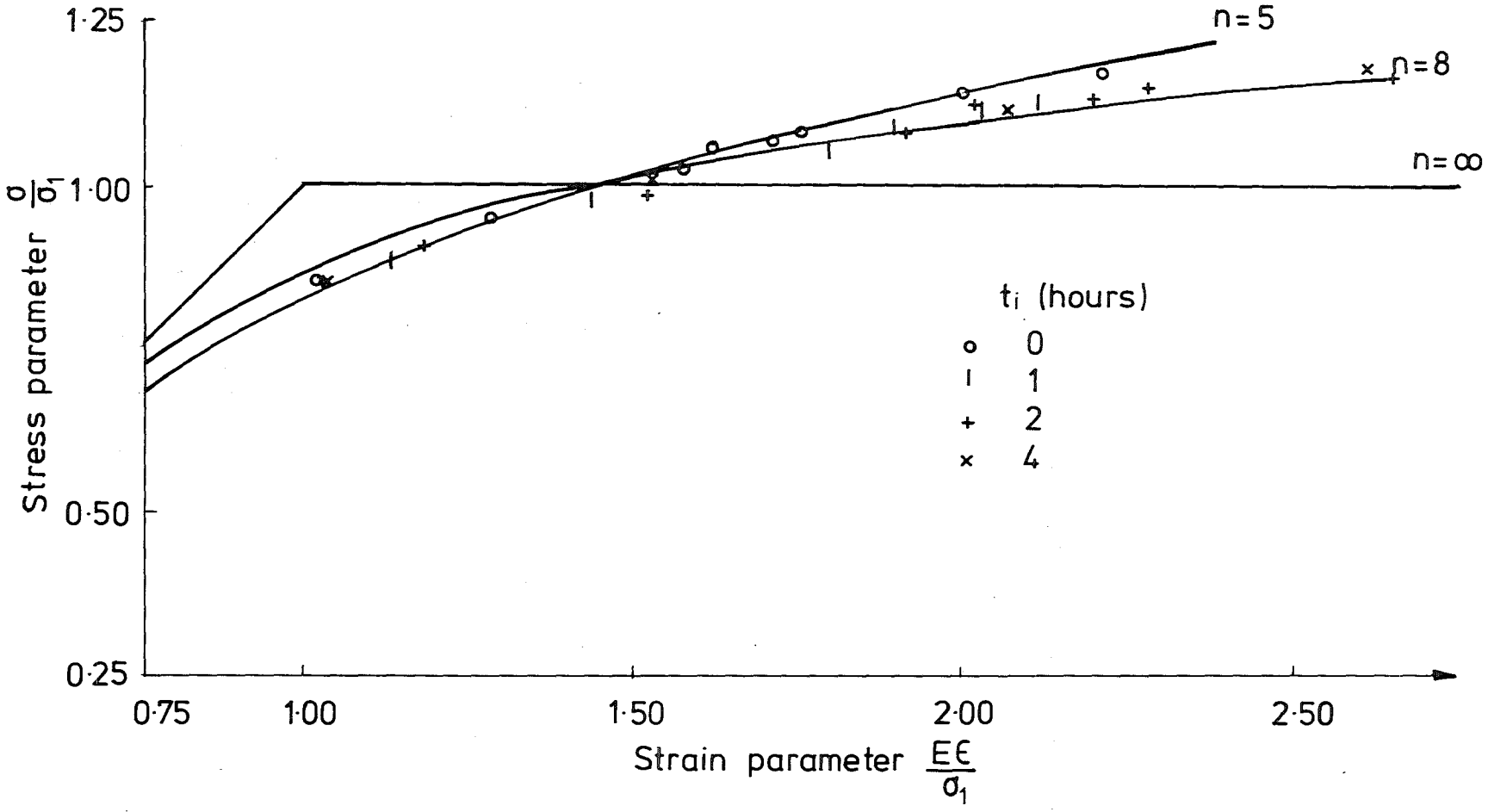

Fig. 5·13 RAMBERG-OSGOOD FORM OF ISOCHRONOUS STRESS STRAIN CURVES.

curves. This suggests that the fringe order is proportional to the axial strain.

The values of the fringe order N and the axial strain ϵ_1 are plotted in Fig. 5.11. A linear relationship between N and ϵ_1 can be established. The scattering accounts for a variation of the gradient of order $\pm 5\%$, probably due to the sensitivity to conditions of the test pieces and conditions of the tests.

Assume for the moment that the transverse strain ϵ_2 is equal to ($-\frac{1}{2}$ axial strain), the linear relationship between N and ϵ_1 tentatively suggests that N is proportional to $(\epsilon_1 - \epsilon_2)$, at least in tensile creep tests, irrespective of the strain level and the time considered.

During the recovery period after a creep test, readings of N and ϵ_1 also agreed with the above linear relationship.

5.7.5 Isochronous stress-strain curves.

Strain ϵ_1 for different stress levels at constant time t_i* = 0, 1, 2, 3, 4 hours was tabulated and the isochronous stress-strain curves plotted (Fig. 5.12). For t_i = 0, 1 hours the isochronous curves are influenced by primary creep, and for t_i = 3,4 hours they are influenced by tertiary creep at high stresses.

* The subscript i stands for "isochronous".

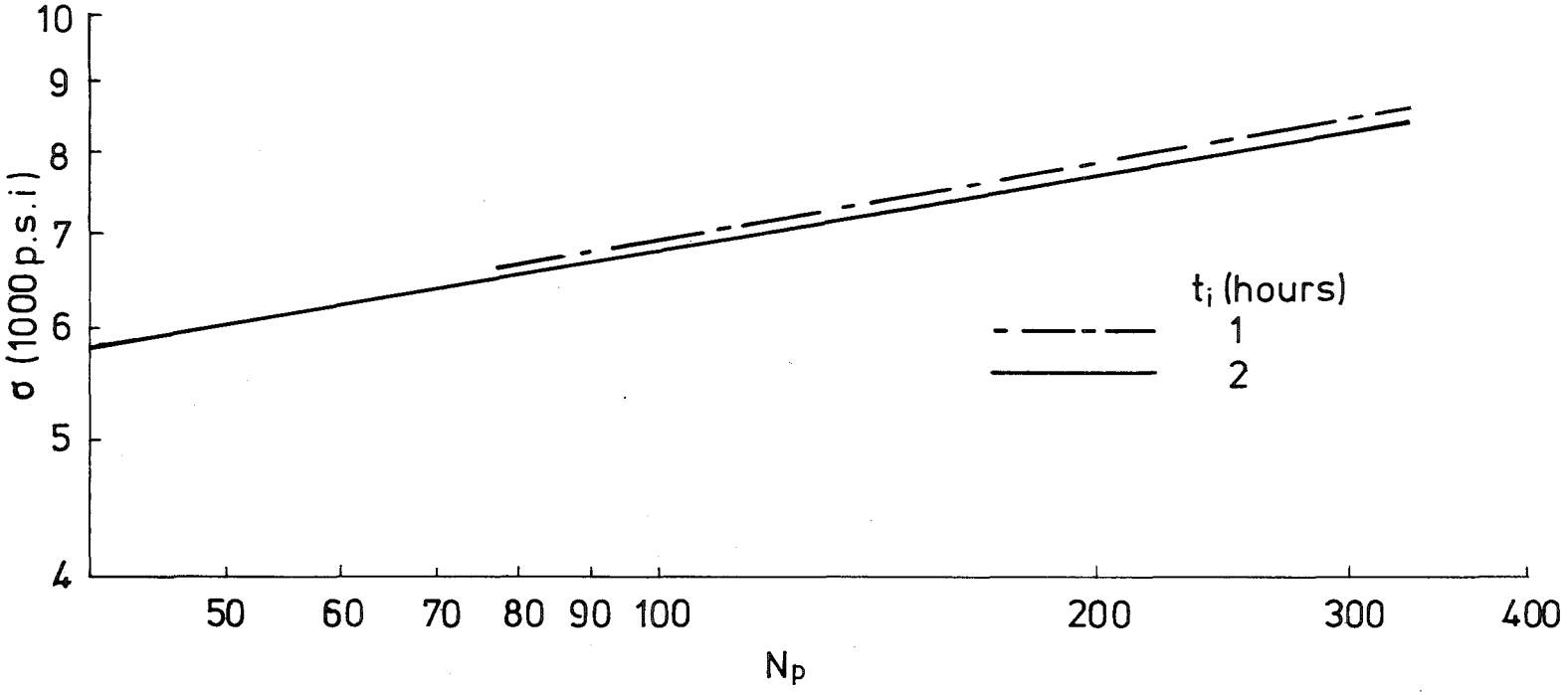

Fig. 5·14 INELASTIC FRINGE ORDER – STRESS

The isochronous curves tend to become parallel to the strain axis with increasing times t_i. This is in agreement with observations by Shanley[93]. The Ramberg-Osgood equation[30] was used to describe these isochronous stress strain curves where m was chosen to be 0.7

$$\frac{E\epsilon}{\sigma_1} = \left(\frac{\sigma}{\sigma_1}\right) + \frac{3}{7}\left(\frac{\sigma}{\sigma_1}\right)^n$$

i.e. σ_1 is determined by the intersection of the isochronous stress-strain curve and the line of gradient $0.7E$.

The coefficient n was found to vary from 5 to 8 (Fig. 5.13). The tendency of isochronous curves to flatten at large strain as t_i increases, implies that n also increases. Therefore, the Ramberg-Osgood equation with a constant n was found not to be a good description of the isochronous curves. This is also evidenced by constant strain rate tests obtained by Brill (Fig. 5.4 in reference 20). The Ramberg-Osgood equation is, however, useful to compare results with other researchers. The use of $\sinh^{-1}$ curve as outlined by Smith and Sidebottom[94] would be a better representation of isochronous stress-strain curves.

5.7.6 Non-linear behaviour of polycarbonate.

The normalised creep curves clearly indicated that the time independence of strain and fringe order is non-linear. The non-linearity of mechanical behaviour of polycarbonate was mentioned by Haward and Thackray[95]. Cloud[19] studied

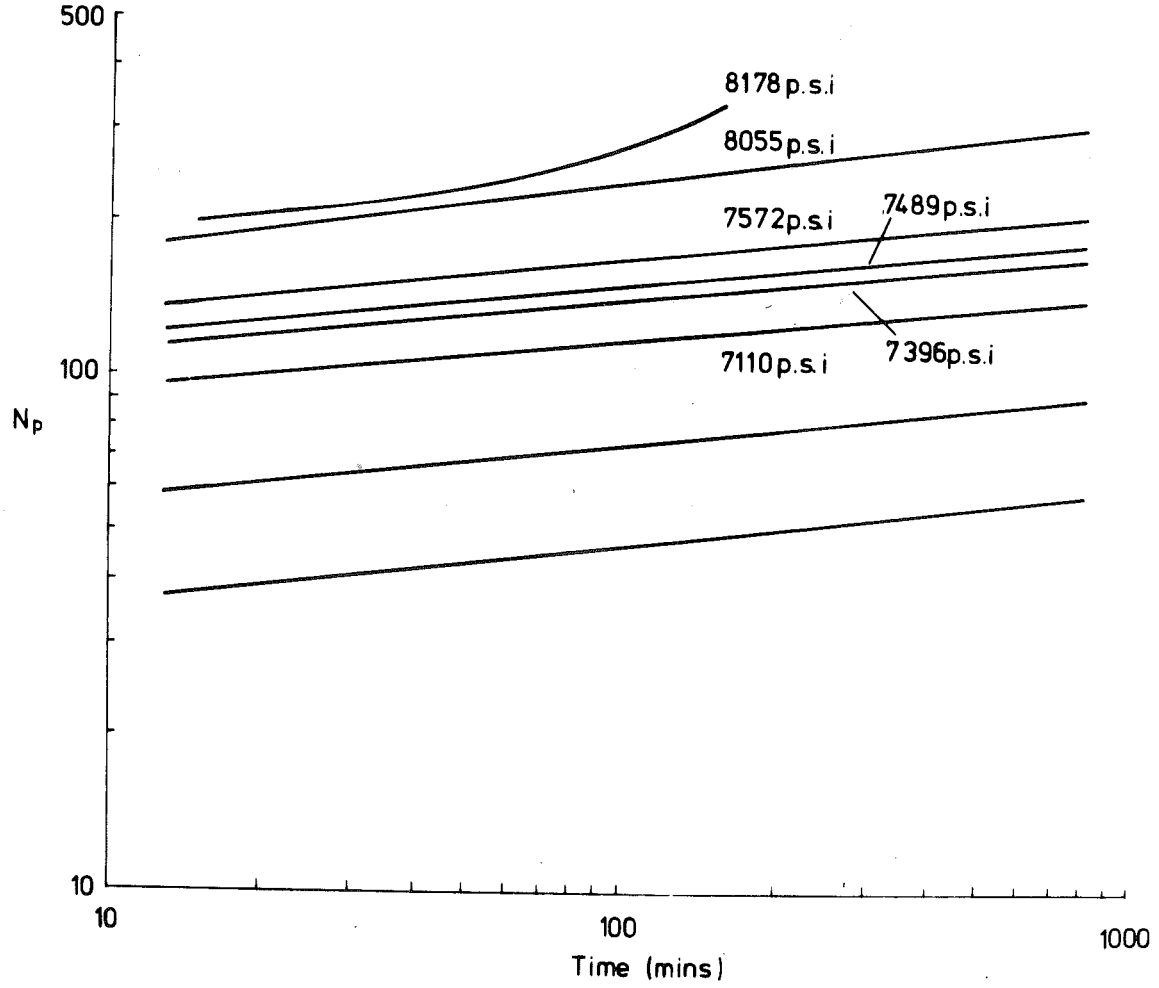

Fig 5·15 VARIATION OF INELASTIC FRINGE ORDER WITH TIME

optical creep of polycarbonate only in stress range 0 - 3200 psi.

As the readings in fringe order N were more readily obtainable than strain, N was used to study stress and time dependence of polycarbonate properties. Consider N to consist of an elastic part N_e and inelastic part N_p:

$$N = N_e + N_p$$

where $N_e = C_\sigma \sigma$

C_σ = "elastic" stress-fringe coefficient, obtained in calibration tests for stresses below 3300 psi.

σ = axial stress in tensile creep tests.

N_p was evaluated for time t_i = 1, 2 hours and plotted in figure 5.14 against stress σ. A linear relationship of log N_p and log σ could be established, indicating that N_p is proportional to $\sigma^{5.3}$.

The values of N_p obtained in creep curves (Fig. 5.8) were also evaluated and are plotted against time in Fig. 5.15 (inelastic fringe creep curve). Except at stress level 8178 psi, where the primary and tertiary creep were pronounced, linear relationship was obtained between log N_p and log t indicating that N_p is proportional to $t^{.13}$.

5.8 STRESS RELAXATION TESTS

Stress relaxation tests can be used to verify the conclusion

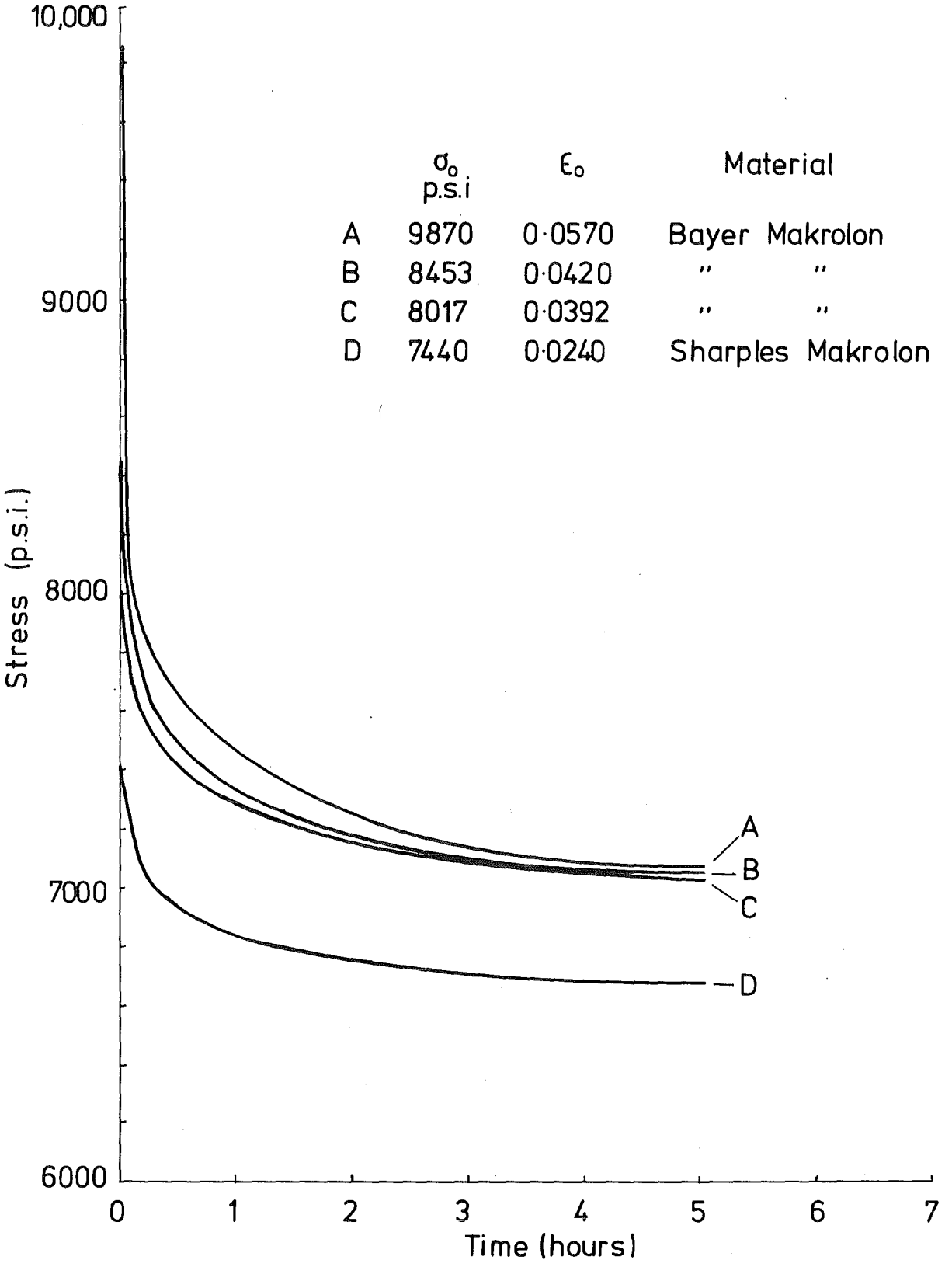

Fig. 5·16 STRESS RELAXATION CURVES

derived from creep tests that the fringe order N is a function of $(\epsilon_1 - \epsilon_2)$ and is independent of stress and time.

5.8.1 Experimental procedures.

Test pieces were strained in the loading frame by the worm gear, with the loading beam pin jointed at both ends to the loading frame. The load was indicated by the proving ring.

Because the stress decreases upon completing the straining, higher initial stress levels were used in stress relaxation tests than in creep tests. Creep tests indicate that the amount of stress relaxed for stress levels lower than 7000 psi would be small; this was also in agreement with stress relaxation tests carried out by Brill[20]. The highest stress level was only limited by the non-uniform appearance of the fringe pattern in the parallel section of the test piece.

Three test pieces were tested in stress relaxation with initial true stress 9870, 8450 and 7440 psi. In these tests the straining rate during straining period was approximately .0060 per minute.

A fourth one was allowed to creep for 3 hours before stress relaxation proceeded (at true stress level 8830 psi) and a fifth test piece was loaded in the same manner in creep tests to a true stress level 8190 psi and relaxation was permitted to begin upon completion of loading.

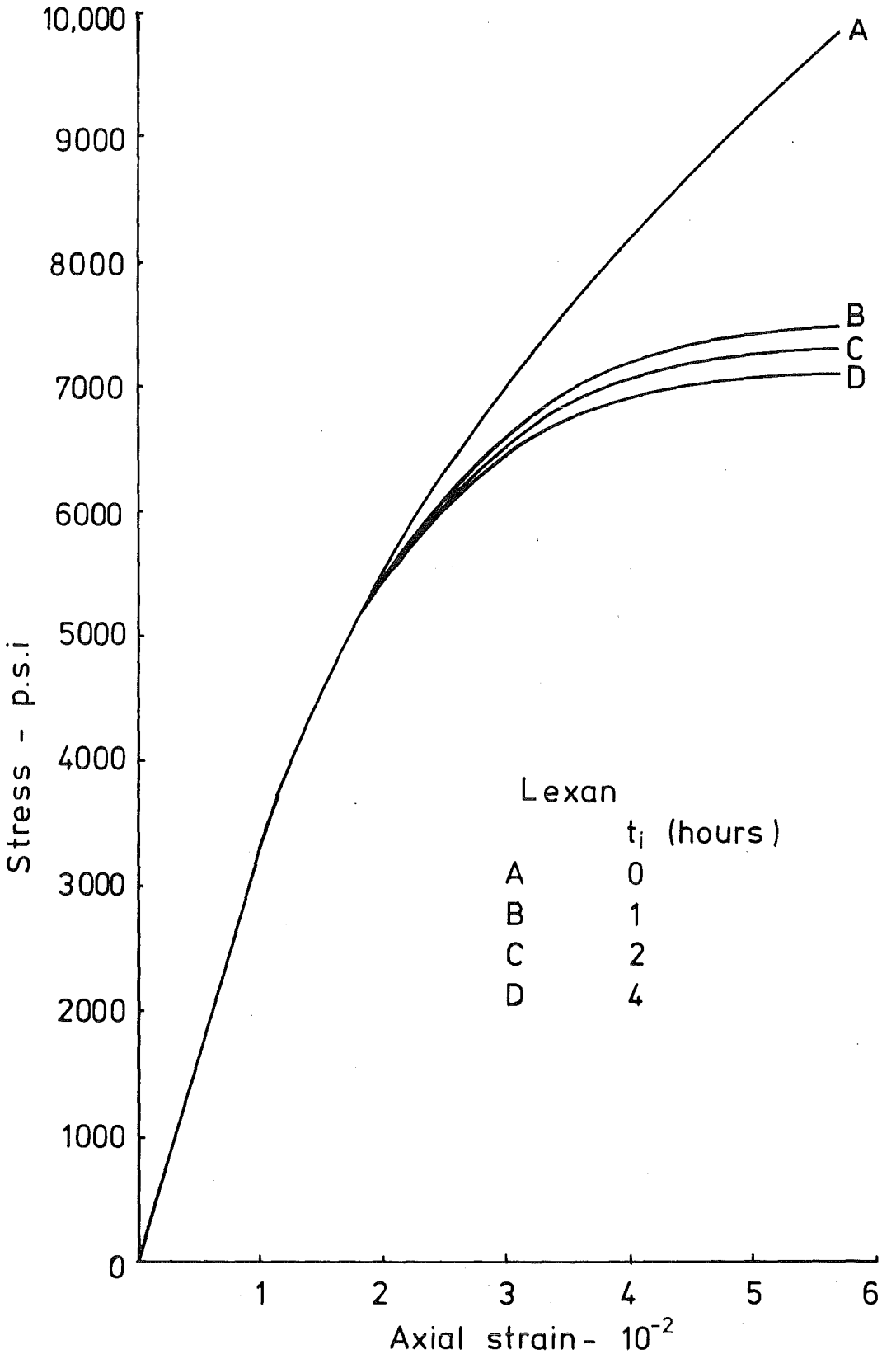

Fig. 5·17 ISOCHRONOUS STRESS-STRAIN CURVES FROM STRESS RELAXATION TESTS.

Preliminary tests confirmed that axial strain remained essentially constant when total elongation was kept constant. Therefore, only a few readings of gauge length or photographs were taken, whereas stress and fringe order were more frequently recorded.

5.8.2 Fringe order - strain relationship.

The fringe order was found to remain essentially constant during stress relaxation tests. An increase of $\frac{\delta N}{N} = 1\%$ was observed over the first two hours for the test of initial stress 9870 psi (much smaller changes were observed with other tests). Corresponding small change of strain was also found for the above test. The changes in N and axial strain were probably due to adjustment in relative strain distribution in the parallel section and filleted section with decreasing stress.

The fringe order N and axial strain obtained in these tests were also plotted in Fig. 5.11, together with data from creep tests.

The fact that both fringe order and axial strain were constant in stress relaxation tests confirmed that fringe order is a function of strain only. Figure 5.11 indicated that a linear relationship between N and ϵ_1 could be established. However, the value of the strain fringe coefficient C_ϵ should be obtained from a test in which both ϵ_1 and ϵ_2 are measured.

The tendency of data in the vicinity of $\epsilon_1 = .0700$ to lie

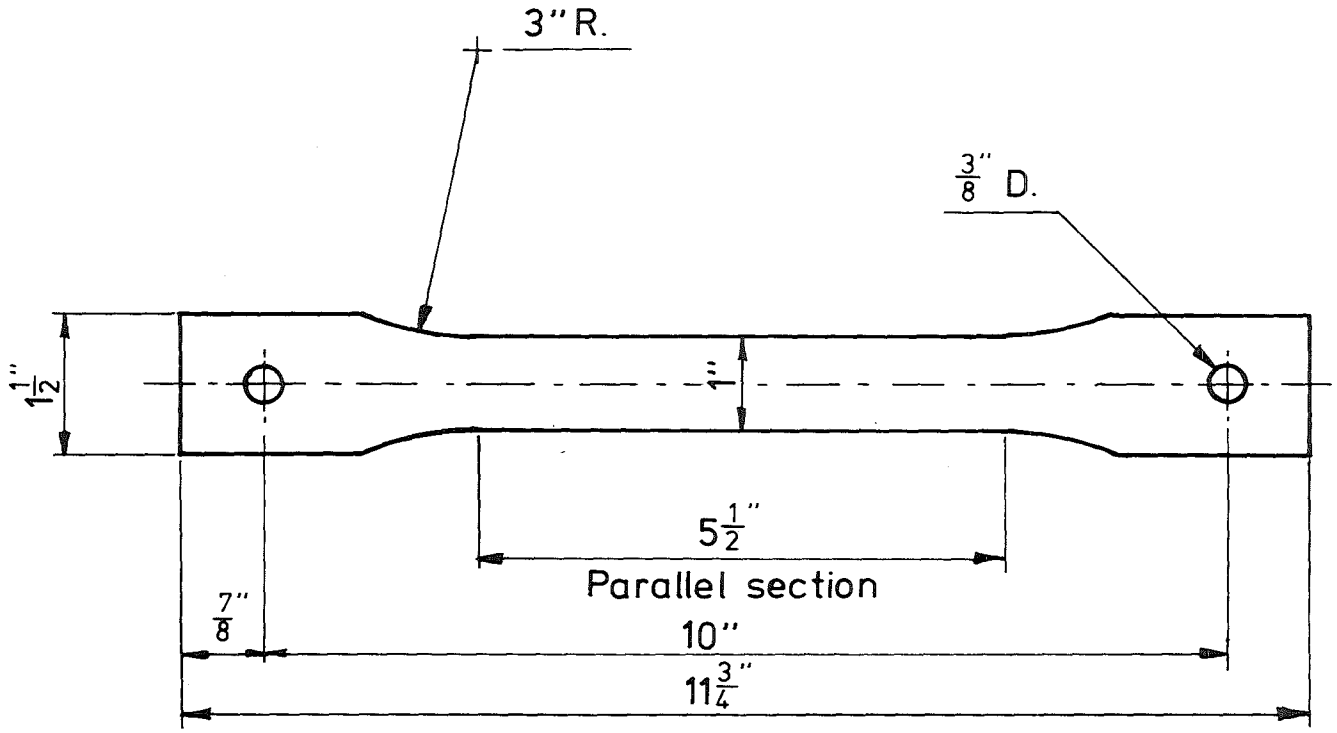

Fig. 5·18 UNIAXIAL TENSILE TEST PIECE - (LARGE)

to the right of the straight line indicated C_ϵ tends to decrease slightly at large strain.

5.8.3 Variation of stress - stress relaxation curves.

Stress relaxation curves are plotted in Fig. 5.16. Initially the rate of decrease in stress is very large but it becomes small after 2 hours, even for a high initial stress. Furthermore, over a 4 hour interval the curves for high stress levels of 9870, 8830, 8950, 8190 approach 7000 psi.
The isochronous stress strain curve for t_i = 0, 1, 2, 4 hours are shown in Fig. 5.17. They appear to be flatter than the corresponding curves from creep tests. (Fig. 5.12).

5.9 TENSILE TESTS TO OBTAIN THE STRAIN - FRINGE COEFFICIENT AND POISSON'S RATIO.

Creep and stress relaxation tests at 20°C clearly show that the fringe order N is proportional to the axial strain; the maximum axial strain investigated was .0800. It is necessary to measure both the axial strain ϵ_1 and the transverse strain to verify the relationship:

$$N = C_\epsilon (\epsilon_1 - \epsilon_2) \quad \text{(normal incidence)}.$$

During such a test the "Poisson's" ratio was also determined. the Poisson's ratio is defined as:

$$\nu = -\frac{\epsilon_2}{\epsilon_1}$$

If a large strain range was investigated, as carried out by

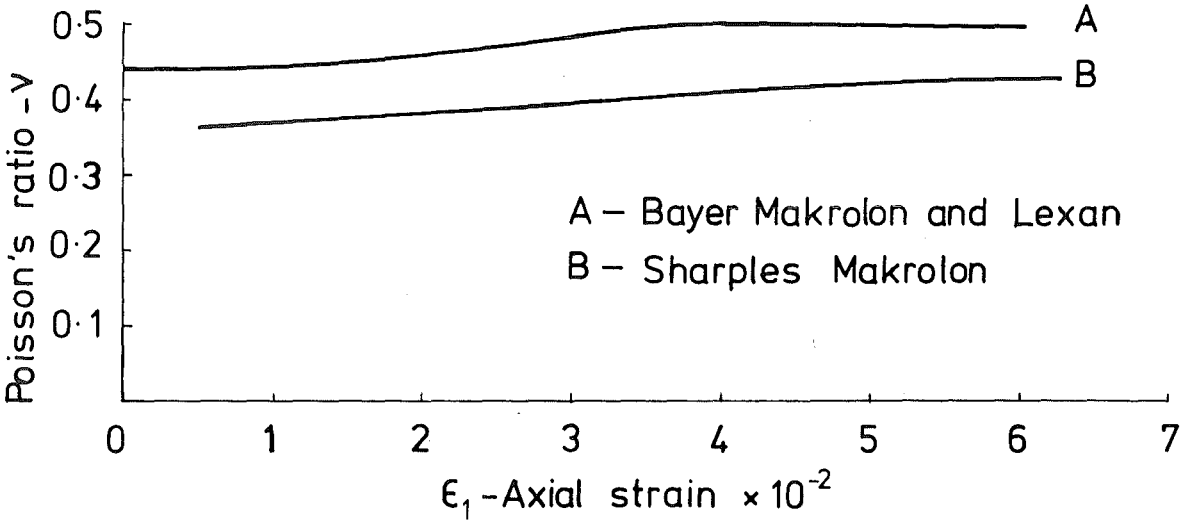

Fig. 5·19 VARIATION OF POISSON'S RATIO WITH AXIAL STRAIN

Brill[20], other definitions of Poisson's ratio by Bahuaud and Boivin[95,96] would be more meaningful.

Test pieces of $5\frac{1}{2}$" parallel section and 1" shank were used for the study of C_ϵ and ν (Fig. 5.18). Grid of 133 L.P.I was photoengraved on these test pieces for the Moiré fringe strain analysis. Axial strain obtained by measuring a gauge length of 4" provided a check on that obtained by Moiré fringes. In some tests a circle of 1" diameter was scribed for the purpose of obtaining ϵ_1 and ϵ_2 by photography. The loading programme was considered not to be critical in view of observations from creep and stress relaxation tests.

Results are shown in Figs. 5.19 and 5.20.

Poisson's ratio was found to be very sensitive to errors in ϵ_1 and ϵ_2. Sharples Makrolon gave low ν compared to Lexan and Bayer Makrolon, and tended to be more rigid and "brittle". Fig. 5.20 confirmed that N is linearly proportional to $(\epsilon_1 - \epsilon_2)$ at least up to $\epsilon_1 - \epsilon_2 = .0700$ but there was a tendency for C_ϵ to decrease slightly thereafter. This is in agreement with results obtained by Brill[20], who showed that the curve N against $(\epsilon_1 - \epsilon_2)$ started to curve to the right at $(\epsilon_1 - \epsilon_2) \simeq .1000$. It should be noted that at large strain the fringe patterns in Brill's test pieces were non-uniform. From Fig. 5.20, strain fringe coefficient $C_\epsilon = 5.60 \times 10^3$ fringe/inch. From Fig. 5.11, assuming an average Poisson's ratio of .40, C_ϵ

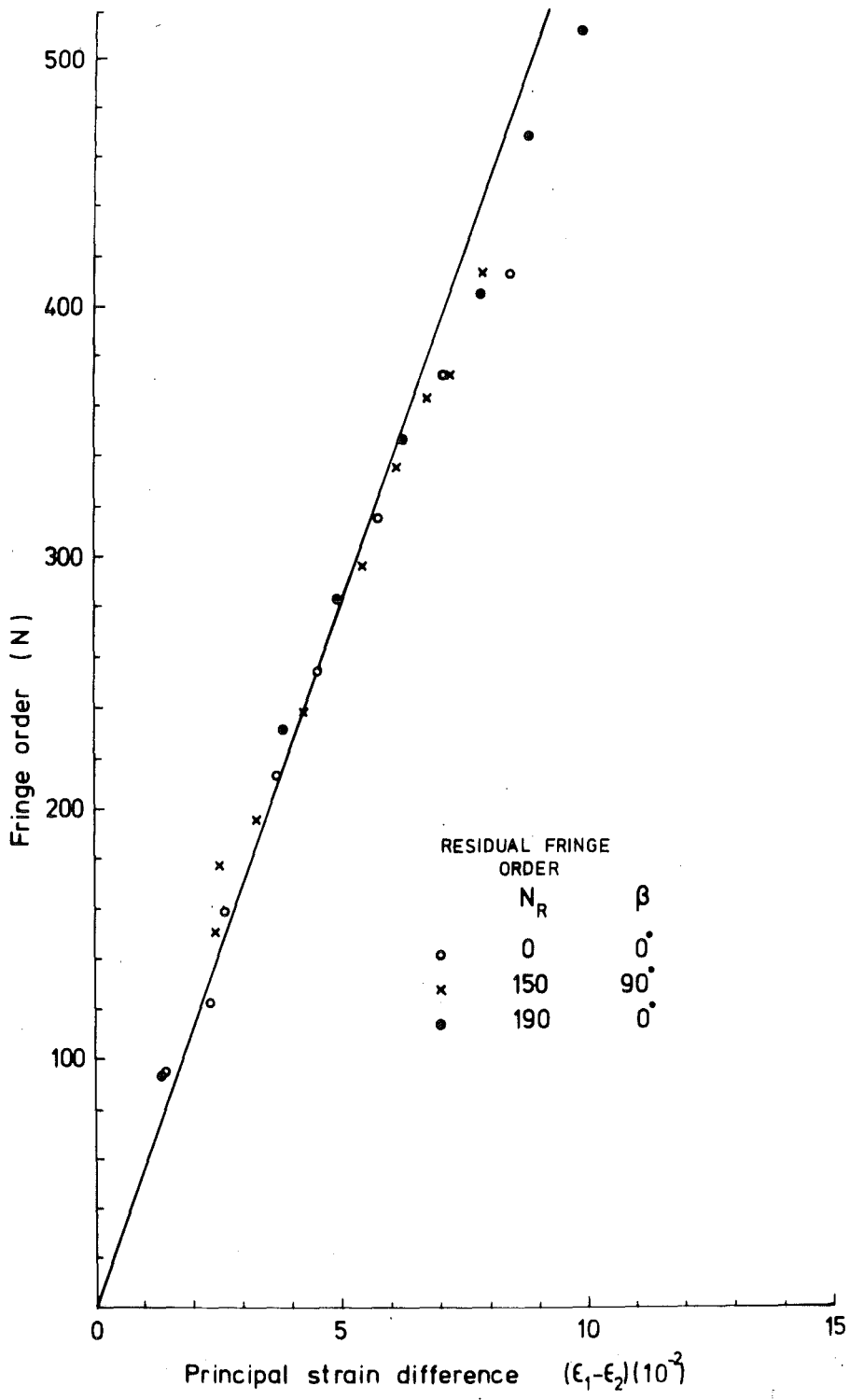
500
400
300
200
100
Fringe order (N)
0
5
10
15
Principal strain difference $(\epsilon_1-\epsilon_2)(10^{-2})$
RESIDUAL FRINGE ORDER
N_R
β
0
0°
150
90°
190
0°

Fig. 5·20

was found to be 5.20×10^3 fringe/inch.

5.10 CONCLUSIONS

At room temperature the fringe order per unit thickness N can be considered linearly proportional to the principal strain difference. Thus the strain-fringe coefficient C_ϵ can be considered constant, independent of stress and its history. C_ϵ decreases slightly at $(\epsilon_1 - \epsilon_2)$ greater than .0700. The range of N and $(\epsilon_1 - \epsilon_2)$ investigated was large in comparison to that involved in photoelasticity but was small in comparison to that given in Appendix 2. This justifies the use of equation (2.9) and Lagrangian engineering strains in the photomechanical relationship. Brill[20] investigated photomechanical relationship for polycarbonate in a larger range of N and ϵ by using data in the non-uniform region of fringe order and strain. In view of the scattering of data due to conditions of characterisation tests and test pieces, only data obtained with uniform fringe order and strain was used in this study.

Polycarbonate was also found to be non-linear in regard to the stress dependence of inelastic deformation or inelastic fringe order. From the Ramberg-Osgood equation of creep isochronous stress strain curve, polycarbonate could be used to simulate the stress strain curve of materials having the Ramberg-Osgood parameter n = 5 to 8. Isochronous stress-strain curves from stress relaxation tests had a stress level approximately 7000 psi as the asymptotic value and thus would be more

suitable to simulate a flat stress strain curve in the inelastic range.

CHAPTER 6

MEANING OF ISOCLINICS AND STRAIN FREEZING EXPERIMENTS.

6.1 INTRODUCTION

In order to investigate the relationship between the secondary principal stress and strain axes and the isoclinics it is necessary to introduce non-coaxiality or mechanical non-coincidence between the stress tensor and the strain tensor. Inelastic mechanical non-coincidence can be effected by non-proportional loading as carried out by Frocht and co-workers [10a,12,13] in experiments on thin walled tubes subjected to tension, torsion and internal pressure. Mechanical non-coincidence can also be introduced by straining, in a uniaxial state for simplicity, a test piece which has been inelastically strained in another direction. The residual strain may be due to room temperature loading (cold stretching)[10a,20] or to the "frozen" strain in a thermal cycle (strain "freezing")[14].

It is also essential to obtain a homogeneous strain field, statically determinate stress field, uniform fringe order and distinct isoclinic directions. For polycarbonate of bisphenol A, experiments reported in Chapter 5 showed that it is not possible to obtain a homogeneous large residual strain and birefringence by cold stretching*, at least not in a wide enough

* Brill[20] obtained reasonably uniform necking in a $\frac{1}{8}$" wide test piece.

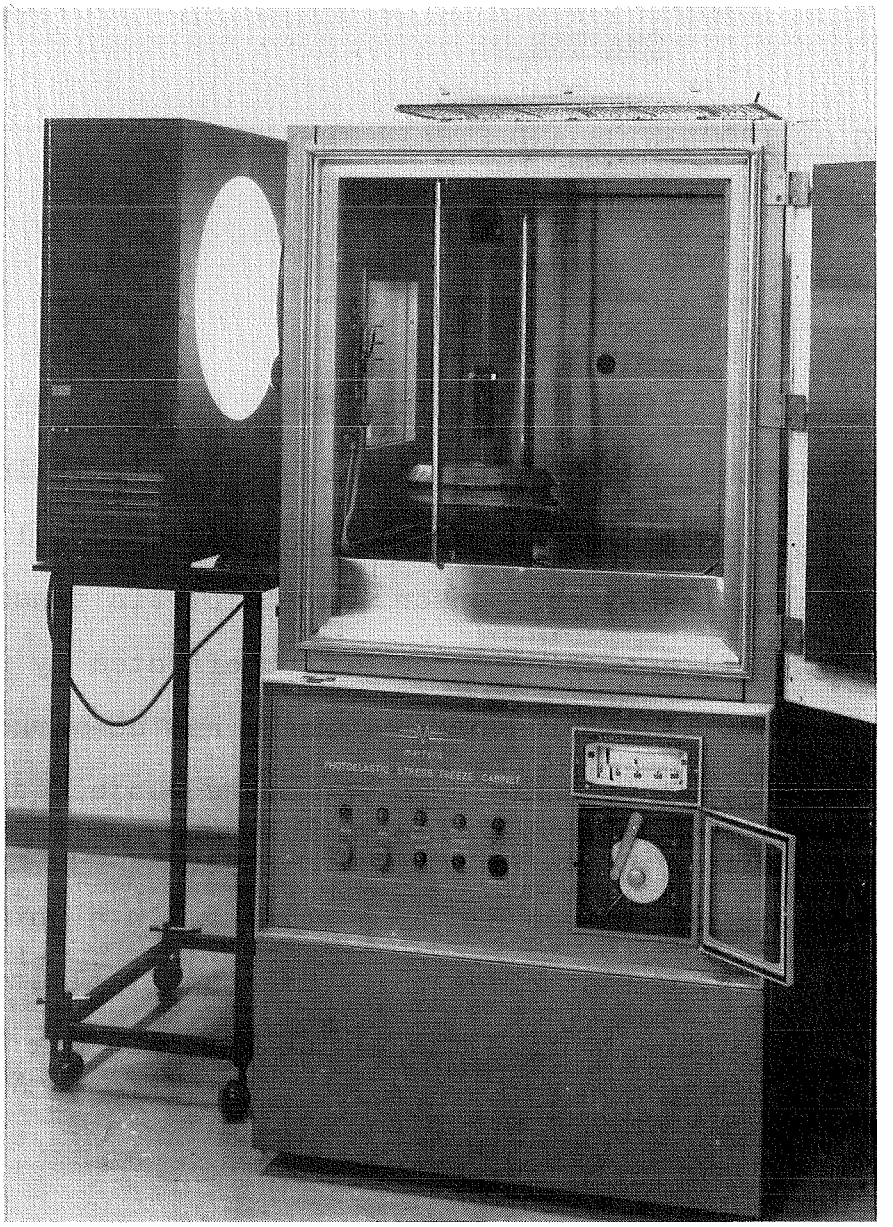

Fig. 6·1 STRAIN FREEZING OVEN.

test piece to allow a second test piece to be cut from the first, with its load line at a relatively large angle to the load line of the initial test piece.
It was, therefore, decided to obtain residual strain and birefringence by strain freezing. The experiments on strain freezing are presented first, followed by plane stress tests on the meaning of isoclinics.

6.2 STRAIN "FREEZING" EXPERIMENTS

The term "stress freezing" has been used in photoelasticity to indicate the process of loading a test piece through a thermal cycle, the maximum temperature of which is in the vicinity of the glass transition temperature of the polymer (above room temperature), so that on returning to room temperature and on removal of the load, residual birefringence is "frozen" into the test piece; no macroscopic stress is frozen in such a process, only birefringence and strain. Therefore, the term "strain freezing" is more appropriate to describe the process.

6.2.1 Experimental methods and apparatus

The strain freezing experiments were carried out in an oven of 2' × 2' × 2' capacity (Fig. 6.1). The oven had two double glass windows ($11\frac{1}{4}$" × $11\frac{1}{4}$") on opposite sides to allow birefringent observations (fringe order and isoclinics) to be observed with the polariscope described in Chapter 5. It

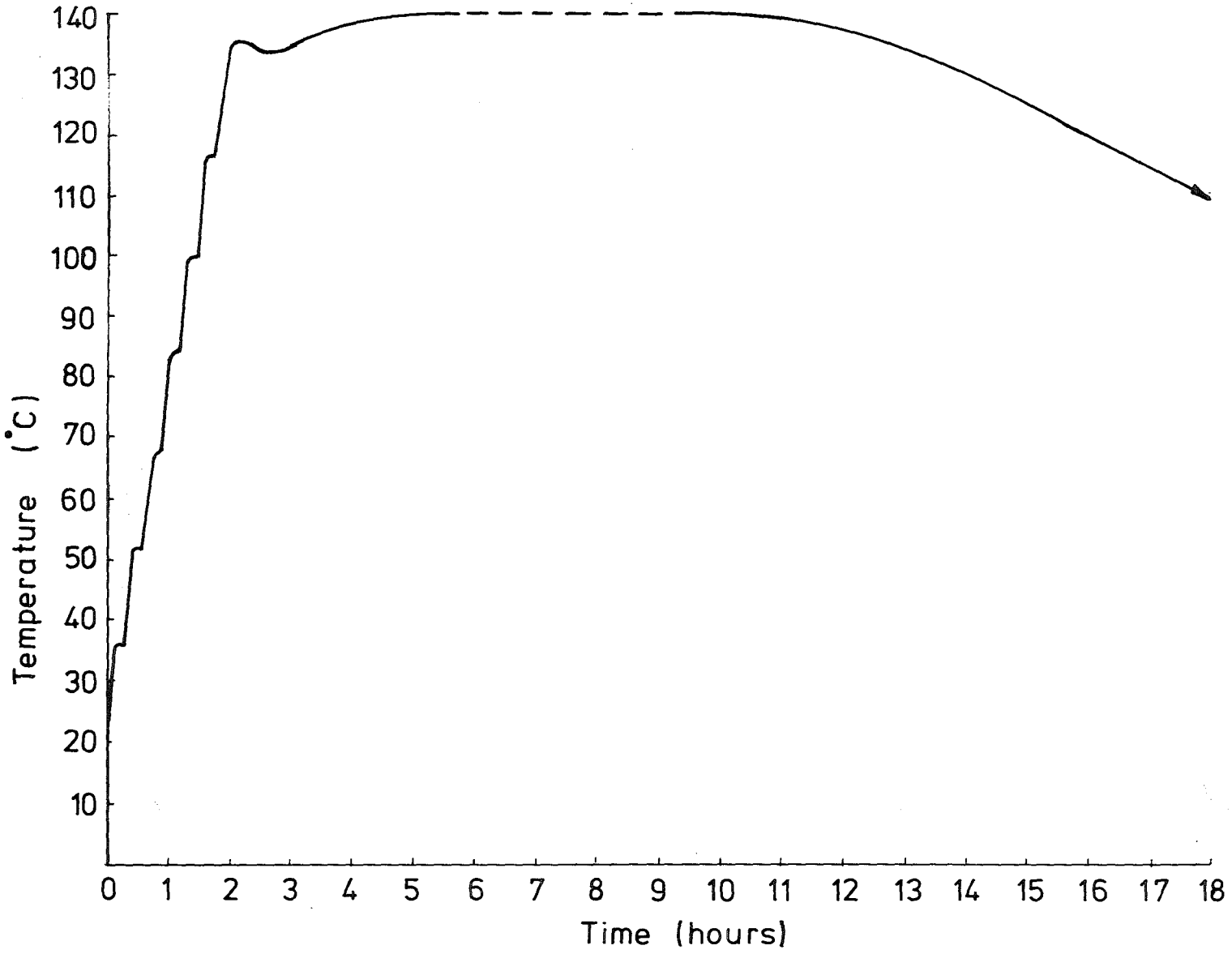

Fig. 6·2 THERMAL CYCLE FOR STRAIN FREEZING EXPERIMENTS.

was equipped with a Transistrol temperature control unit which controlled temperature within .5 C°, up to 200°C. The thermal cycle was effected by a cam. The oven had two heating elements: a booster to be used for the first 2 hours only and a heater to be used throughout the cycle. The air was circulated by a fan and cooling was effected by natural cooling, with heaters off. A typical thermal cycle is shown in Fig. 6.2. When the booster was switched off, temperature increased slowly to the maximum temperature and soaking time was therefore not precisely defined. The initial set cooling rate was 5C° per hour. However, below 70°C the natural cooling rate of the oven was less than 5C° per hour, in which case the oven could be switched off without upsetting the cycle.

The test pieces (Figs 5.3 and 5.18) were loaded by dead weight in a loading frame inserted in the oven. As a check on the cam controller, the temperature was recorded by a Brown-Honeywell recorder from thermocouples placed in the oven; thermometers were also used.

The strain was measured by photographing scribed-gauge marks and scribed circles as described in Chapter 5, except that the polariscope light source was used with the crossed plane polariscope set up to give a dark background. A steel ruler was provided as a scale to take into account any shift in the lens-to-test piece distance.*

* It can be shown that thermal expansions of the ruler, and of polycarbonate, if isotropic, do not affect the principal strain difference $(\epsilon_1 - \epsilon_2)$.

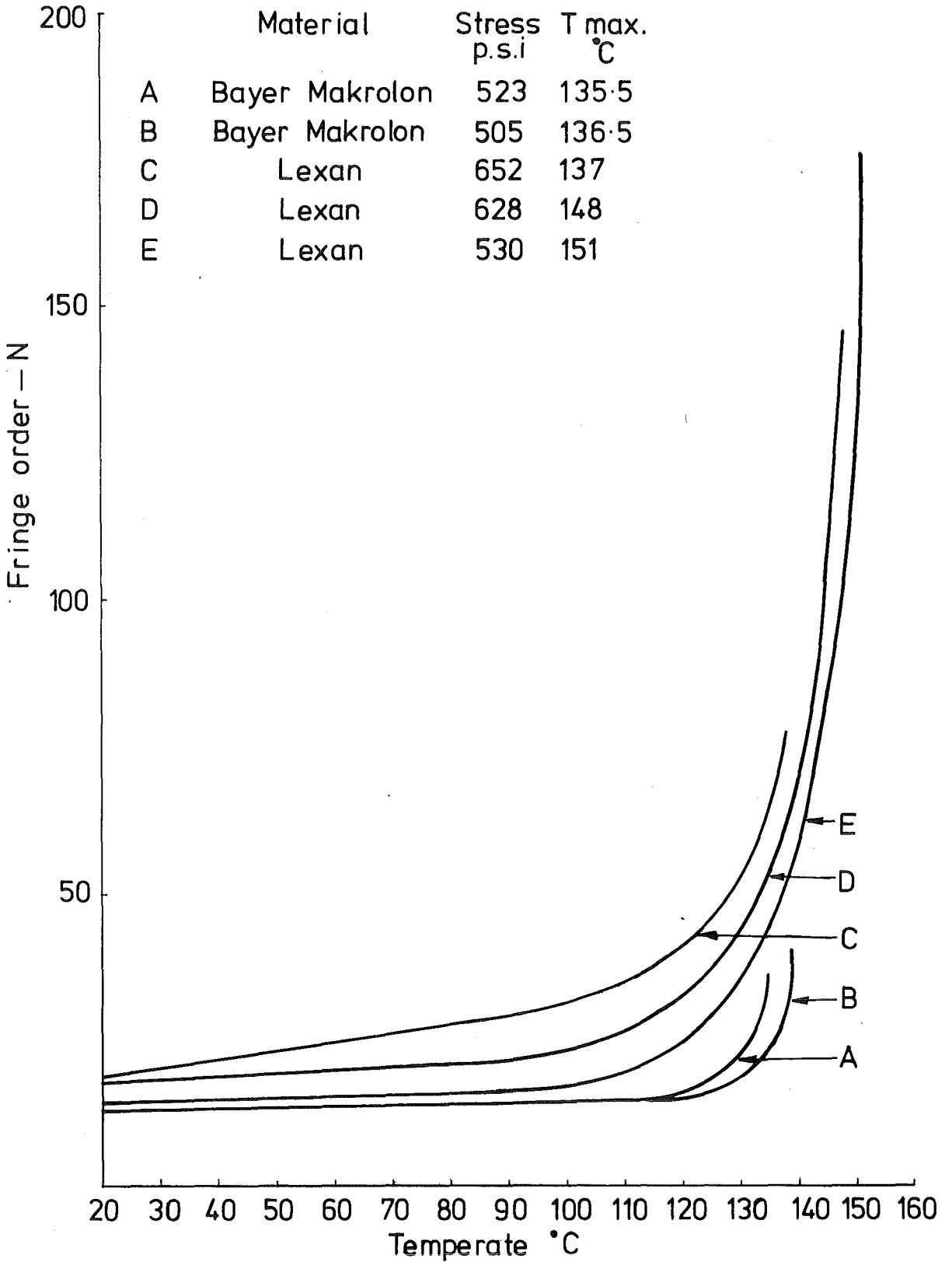

Fig. 6·3 FRINGE ORDER VARIATION WITH TEMPERATURE DURING HEATING PERIOD

Guided by the strain freezing experiments of Hunter and Schwarz[32], a stress level of 1000 psi and T_{max} of 280°F were chosen for preliminary experiments. However, it was found that after 5 hours of heating, crazing cracks developed and affected the fringe pattern in the parallel section. Compression moulded Bayer Makrolon was more sensitive to crazing than extruded Lexan. Furthermore, serrated grips used for room temperature gripping were found unsuitable for strain freezing experiments.

Thin abestos was inserted between the test piece and the flat face of the circular grips to avoid premature failure at the grips. The stress range was between 500 psi to 750 psi to obtain sufficiently large frozen strain and birefringence and yet to avoid crazing.

6.2.2 Variation of birefringence and strain with temperature

The variation of fringe order N during the heating period and under constant load is shown in Fig. 6.3. For a given initial stress level, N increases very slowly up to a temperature in the vicinity of 110°C; the gradient of N with temperature becomes very large as temperature approaches the glass-transition temperature range of polycarbonate (145°C - 150°C). An increase in the initial stress level shifts the N - T curve in the vertical direction as expected. However, for a similar stress level, the curves for Bayer Makrolon and Lexan are different (curve A and E in Fig. 6.3), at least in the

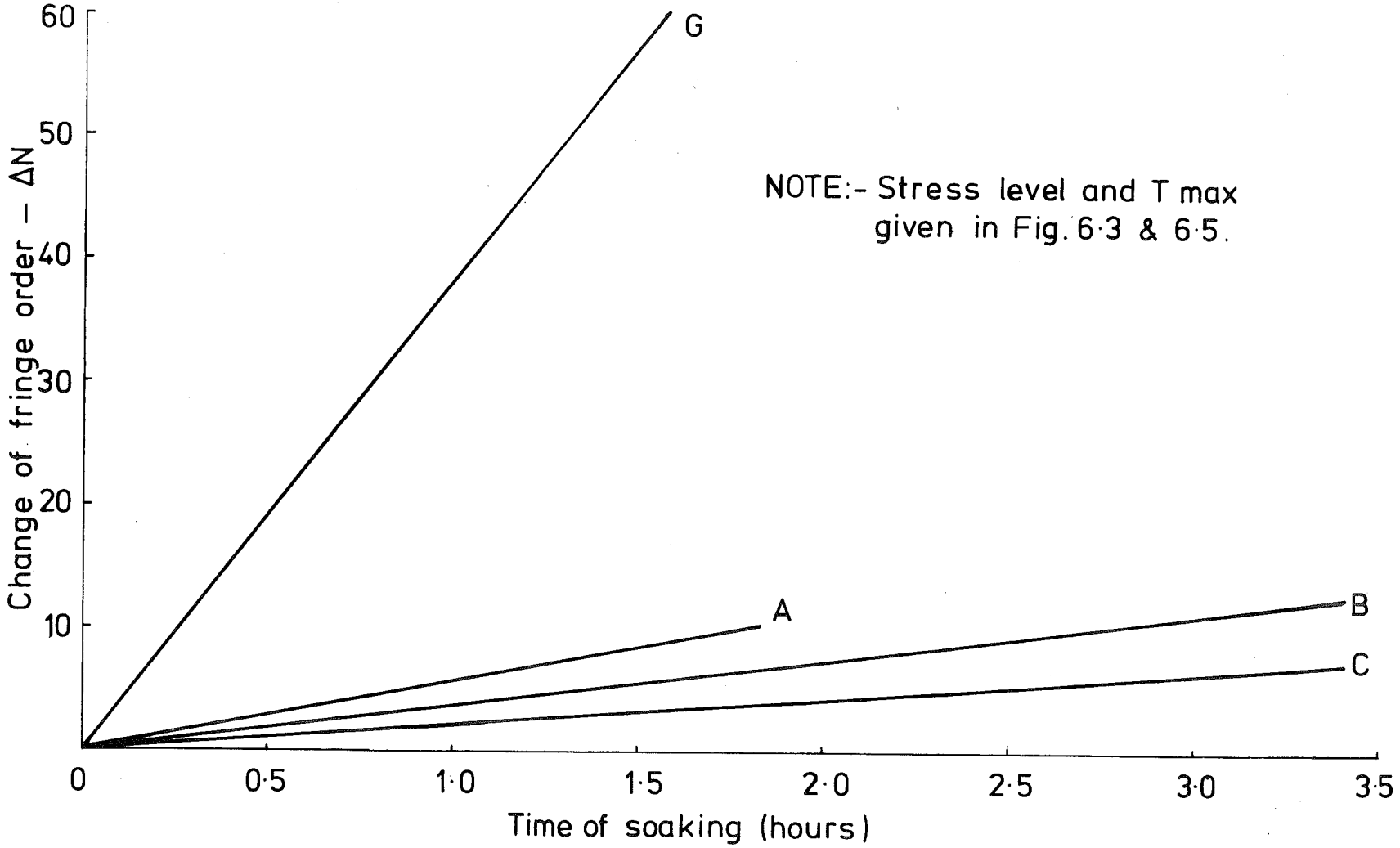

Fig. 6·4 VARIATION OF N DURING SOAKING PERIOD

temperature range below 136°. The discrepancy was probably due to different initial states of the two types of polycarbonate and would diminish when temperatures approached the T_g range.

The fringe order continued to increase during the soaking period, and the increase ΔN is found to be proportional to the time of soaking (Fig. 6.4). However, for the thermal cycle adopted, it was found that most of the increase in fringe order took place during the heating period, and that a small increase in T_{max} resulted in a large increase in N. N was also increased by increasing stress or by increasing soaking time but these methods led to more crazing.

During the cooling period, N was found to increase when temperature was still higher than T_g and thereafter remained essentially constant. At the end of the thermal cycle, on removal of the load, a decrease of N was observed. It was found that (Table 6.1 of Appendix 7):

$$N_{max} = N_0 + N^R \qquad (6.1)$$

where N_{max} = maximum fringe order during the thermal cycle.

N_0 = initial fringe order.

N^R = residual or frozen fringe order.

From Fig. 6.3, it can be seen that:

$$N_{max} >> N_0 \qquad (6.2)$$

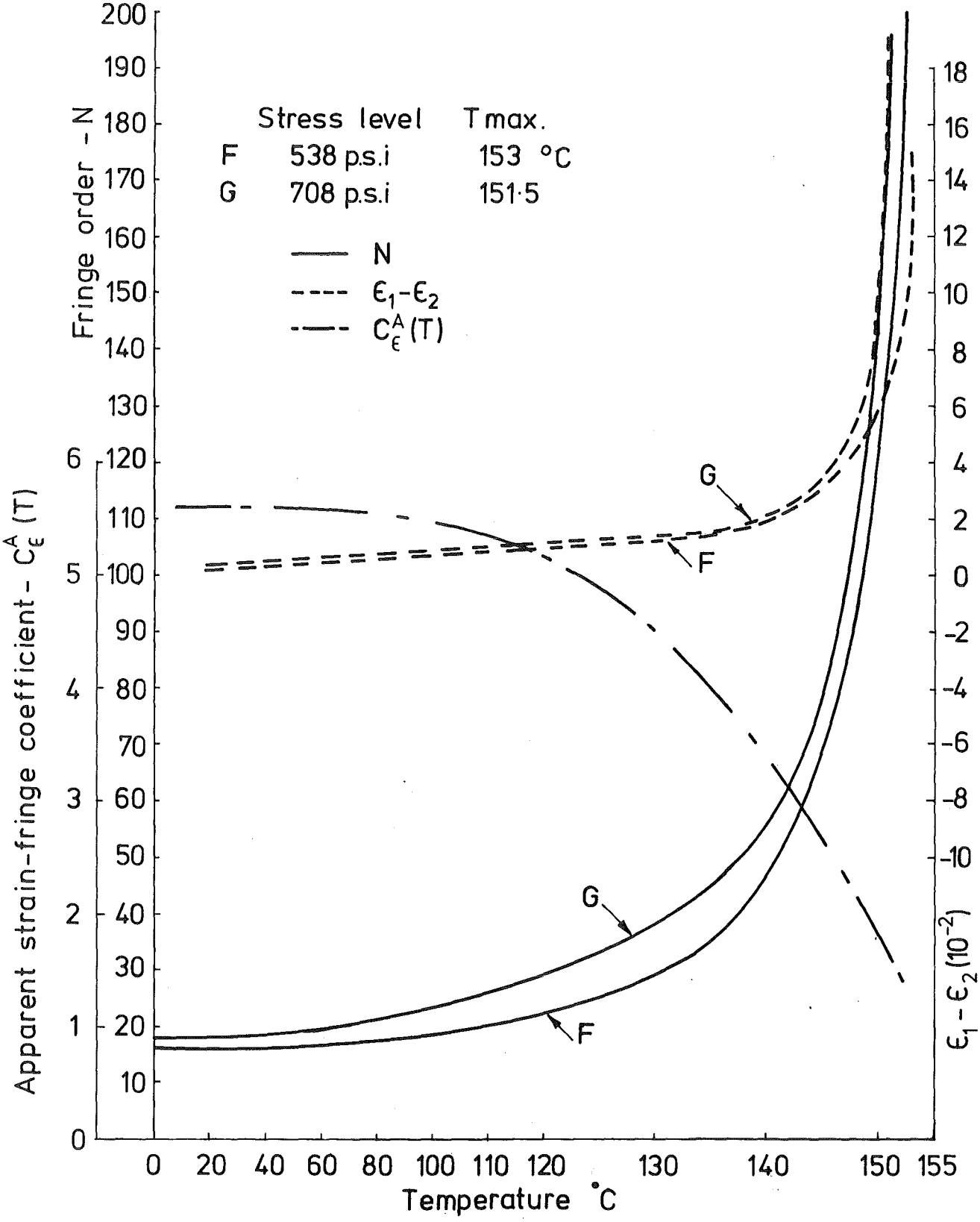

Fig.6·5 VARIATION OF FRINGE ORDER, PRINCIPAL STRAIN DIFFERENCE AND APPARENT STRAIN-FRINGE COEFFICIENT WITH TEMPERATU

Therefore, if a large N^R is desired without inducing crazing, a thermal cycle having large T_{max}, low stress and short soaking time should be chosen. It was found that a T_{max} in the 150 - 155°C range was suitable for this purpose.

Excessive deformation was found when T_{max} was greater than 155°C, however, this depends also on the stress level and initial state of the test piece.

The variation of principal strain difference $(\epsilon_1 - \epsilon_2)$ with temperature follows a similar pattern to that of fringe order, as shown in Fig. 6.5, in which the temperature scale above 120°C is lengthened because of large variation of strain and fringe order. Typical data for a test is given in Table 6.2 of Appendix 7; a summary of results of other tests is given in Table 6.1 of Appendix 7.

6.2.3 Apparent and residual strain-fringe coefficients.

During the heating period, the ratio of $\frac{N}{\epsilon_1 - \epsilon_2}$ was evaluated at different temperatures. This ratio is called the apparent strain-fringe coefficient.

$$C_\epsilon^A(T) = \frac{N}{(\epsilon_1 - \epsilon_2)} \qquad (6.3)$$

where T is the temperature during the heating period. $C_\epsilon^A(T)$ decreased with temperature as shown in Fig. 6.5, i.e. the rate of increase of $(\epsilon_1 - \epsilon_2)$ with temperature, is greater than that of N. $C_\epsilon^A(T)$ is independent of the initial stress

level within the range investigated (500-750 psi).

The residual or frozen strain-fringe coefficient is defined as:

$$C_{\epsilon}^{R} = \frac{N^{R}}{(\epsilon_1^{R} - \epsilon_2^{R})} \quad * \qquad (6.4)$$

From Table 6.1 of Appendix 7 test pieces (A, B, C) and (E, G) showed that C_{ϵ}^{R} depended on T_{max}, irrespective of stress level and soaking time. These two groups of test pieces together with D and F indicated that C_{ϵ}^{R} decreases with increasing T_{max}. This follows from the facts that N^{R} is only slightly smaller than N_{max} and that the rate of increase of $(\epsilon_1 - \epsilon_2)$ with temperature is greater than that of N as observed above.

Only the apparent strain-fringe coefficient $C_{\epsilon}^{A}(T)$ and the residual strain-fringe coefficient C_{ϵ}^{R} were obtained from the strain-freezing experiments, but $C_{\epsilon}^{A}(T)$ can be related to the isothermal strain-fringe coefficient $C_{\epsilon}(T)$ as follows:

6.2.4 Relationship between $C_{\epsilon}^{A}(T)$ and $C_{\epsilon}(T)$.

Assume equation (4.2) apply for a case of isothermal deformation i.e.

$$N = C_{\epsilon}(T) \cdot (\epsilon_1 - \epsilon_2) \qquad \text{(normal incidence)} \quad (6.5)$$

where $C_{\epsilon}(T)$ is a function of temperature.

* Superscript R indicates residual or "frozen" quantity.

During the heating period of the thermal cycle, consider the increase in N in an increment of time:

$$\delta N = d\theta\left[\frac{\partial C_{\epsilon}(\theta)}{\partial \theta}\ (\epsilon_1 - \epsilon_2) + \frac{\partial(\epsilon_1 - \epsilon_2)}{\partial \theta}\ C_{\epsilon}(\theta)\right] \qquad (6.6)$$

where θ is a temperature parameter varying between room temperature and T. Fig. (6.5) shows that

$$\frac{\partial C_{\epsilon}(\theta)}{\partial \theta} << \frac{\partial(\epsilon_1 - \epsilon_2)}{\partial \theta}$$

therefore:

$$\partial N \simeq d\theta\ \frac{\partial(\epsilon_1 - \epsilon_2)}{\partial \theta}\ C_{\epsilon}(\theta)$$

$$\simeq \delta(\epsilon_1 - \epsilon_2)\ C_{\epsilon}(\theta)$$

The total change of N from room temperature to a temperature $\theta \leqslant T_{max}$ is given by:

$$\Delta N = \Sigma\ C_{\epsilon}(\theta)\ \delta(\epsilon_1 - \epsilon_2)$$

When θ is in the vicinity of T_g $\Delta N >> N_0$, thus:

$$N = N_0 + \Delta N$$

$$\simeq \Sigma\ C_{\epsilon}(\theta)\ \delta(\epsilon_1 - \epsilon_2)$$

The apparent strain fringe coefficient at the temperature θ as defined by equation (6.3) is given by:

$$C_{\epsilon}^{A}(T) = \frac{\Sigma\ C_{\epsilon}(\theta)\ \delta(\epsilon_1 - \epsilon_2)}{(\epsilon_1 - \epsilon_2)} \qquad (6.7)$$

the sum is effected from θ = room temperature to θ = T

As shown by Fig. 6.5 $C_{\epsilon}^{A}(T)$ decreases with temperature while $(\epsilon_1 - \epsilon_2)_T$ increases with T, indicating that $C_{\epsilon}(T)$ decreases with temperature, i.e.

$$C_{\epsilon}\ (\theta_2) \leqslant C_{\epsilon}\ (\theta_1)$$

where $\theta_1 < \theta_2 \leqslant T$

therefore: R.H.S of equation (6.7) $\geqslant C_{\epsilon}(T)\ \frac{\Sigma\ \delta(e_1 - e_2)}{(e_1 - e_2)_T}$ (6.8)

giving: $$C_{\epsilon}^{A}(T)\ \geqslant C_{\epsilon}(T)$$

As T approaches the temperature range 145 - 150°C, equation (6.7) indicates that the discrepancy between $C_{\epsilon}^{A}(T)$ and $C_{\epsilon}(T)$ would increase in order to keep $C_{\epsilon}^{A}(T)$ decreased in spite of the rapid increase in $(\epsilon_1 - \epsilon_2)_T$. Thus $C_{\epsilon}(T)$ would decrease with T, in agreement with the conclusion arrived at in Chapter 3.

The isothermal strain-fringe coefficient $C_{\epsilon}(T)$ could be obtained if the loading took place at temperature T (with the test piece already in thermal equilibrium at T), instead of being loaded at room tempterature in strain freezing tests.

6.2.5 Appearance of isoclinics.

When an extruded Lexan test piece was observed in the crossed plane polariscope, no definite isoclinic directions could be assigned as the test piece did not appear distinctly dark even when the fringe order was uniform and small. This was also observed in Bayer Makrolon and Lexan test pieces

that had been inelastically strained. This can be explained by assuming that the principal directions of the index tensor (Chapter 2) do not remain constant throughout the thickness of the test piece. While the rotation of these principal axes was small (found by rotating the analyser while the polariser was fixed) it would complicate the interpretation of isoclinics. However, when the frozen test piece was examined for isoclinics, the isoclinic direction in the parallel section was distinct and parallel to the axis of the test piece as expected. When distinct isoclinic direction is required it is desirable that residual fringe order and strain should be obtained by strain freezing.

6.3 TESTS ON MEANING OF ISOCLINICS

In elastic or linear-viscoelastic behaviour, non-proportional loading in plane stress without unloading is possible, either in a homogeneous biaxial plane stress as demonstrated by Mönch and Galster[97], or non-homogeneous plane stress as proved by Dill and Fowlke[38]. Stress concentration or non-linear behaviour would render these methods unsuitable for non-linear inelastic behaviour.

A large test piece was, therefore, strain frozen to obtain a large and homogeneous residual birefringence and strain field, smaller test pieces were then cut from it at various angles to its axis and were again uniaxially deformed, resulting in mechanical non-coincidence.

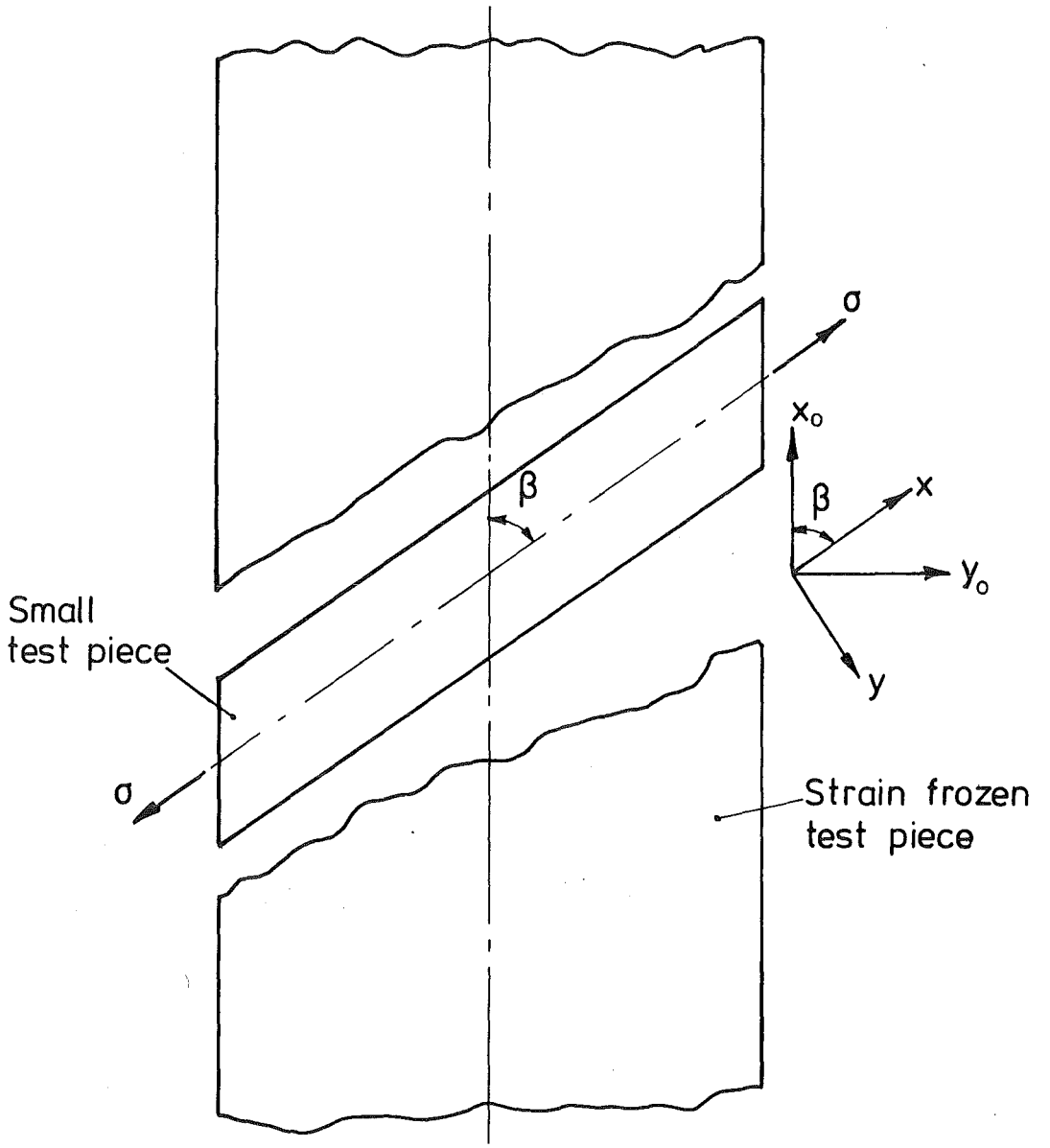

Fig. 6·6

6.3.1 Fringe order tensor

At this stage it is convenient to introduce the concept of "fringe order" tensor N_{ij}. It is a tensor such that

a) its secondary principal directions are parallel to isoclinic directions.

b) the difference of its secondary principal values is equal to the fringe order per unit optical path:

$$N_1' - N_2' = N \tag{6.9}$$

This concept is particularly useful when equation (2.9) is sufficient to describe the photomechanical relationship. Equation (2.9) can be written as:

$$N_{ij} = \frac{\omega c^2 a_1}{2V_0^3} \lambda_{ij} \tag{6.10}$$

6.3.2 Theoretical analysis of isoclinics tests

Let the strain frozen test piece have a uniform residual strain field represented by the strain tensor ϵ_{ij}^R which has principal values ϵ_1^R, ϵ_2^R along directions (x_0, y_0) (Fig. 6.6). Let N^R be its residual birefringence, then:

$$N^R = C_\epsilon^R (\epsilon_1^R - \epsilon_2^R) \tag{6.11}$$

or $$N_{ij}^R = C_\epsilon^R \epsilon_{ij}^R \tag{6.12}$$

Let a smaller test piece be cut off the strain frozen test piece at a direction β with respect to x_0 $(0^\circ \leqslant \beta \leqslant 90^\circ)$ and be subjected to a uniaxial tension at room temperature.

Let σ be the uniaxial stress and ϵ_{ij}^{σ} the strain tensor resulting from the application of σ.

Assume that the smaller test piece is isotropic so that principal values of ϵ_{ij}^{σ} are: ϵ_1^{σ} along x and ϵ_2^{σ} along y (and also ϵ_3^{σ} normal to plane (x, y)).

a. Total strain tensor.

Let ϵ_{ij}^{T} be the total strain tensor resulting from ϵ_{ij}^{R} and ϵ_{ij}^{σ}. The components of ϵ_{ij}^{T} referred to (x, y) can be shown to be:

$$\epsilon_x^T = \epsilon_1^{\sigma} + \tfrac{1}{2}[(\epsilon_1^R + \epsilon_2^R) + (\epsilon_1^R - \epsilon_2^R)\cos 2\beta]$$

$$\epsilon_y^T = \epsilon_2^{\sigma} + \tfrac{1}{2}[(\epsilon_1^R + \epsilon_2^R) - (\epsilon_1^R - \epsilon_2^R)\cos 2\beta] \qquad (6.13)$$

$$\epsilon_{xy}^T = \tfrac{1}{2}(\epsilon_1^R - \epsilon_2^R)\sin 2\beta$$

The principal strain directions of ϵ_{ij}^{T} are given by:

$$\tan 2\alpha = \frac{\sin 2\beta}{\cos 2\beta + \dfrac{\epsilon_1^{\sigma} - \epsilon_2^{\sigma}}{\epsilon_1^R - \epsilon_2^R}} \qquad (6.14)$$

b. Total fringe order tensor.

Assume that the fringe order tensor associated with ϵ_{ij}^{σ} is given by;

$$N_{ij}^{\sigma} = C_{\epsilon}\, \epsilon_{ij}^{\sigma} \qquad (6.15)$$

where C_{ϵ} is the strain-fringe coefficient at room temperature. The total fringe order tensor N_{ij}^{T} is assumed to be the sum of

N_{ij}^{R} and N_{ij}^{σ}:

$$N_{ij}^{T} = N_{ij}^{R} + N_{ij}^{\sigma}$$

by equations (6.12) and (6.15):

$$= C_{\epsilon}^{R}\, \epsilon_{ij}^{R} + C_{\epsilon}\, \epsilon_{ij}^{\sigma} \qquad (6.16)$$

Similarly to equation (6.13), components of N_{ij}^{T} referred to (x, y) axes are:

$$N_x = C_{\epsilon}\, \epsilon_1^{\sigma} + \tfrac{1}{2}\, C_{\epsilon}^{R}\, [(\epsilon_1^{R} + \epsilon_2^{R}) + (\epsilon_1^{R} - \epsilon_2^{R}) \cos 2\beta]$$

$$N_y = C_{\epsilon}\, \epsilon_2^{\sigma} + \tfrac{1}{2}\, C_{\epsilon}^{R}\, [(\epsilon_1^{R} + \epsilon_2^{R}) - (\epsilon_1^{R} - \epsilon_2^{R}) \cos 2\beta] \qquad (6.17)$$

$$N_{xy} = \tfrac{1}{2}\, C_{\epsilon}^{R}\, (\epsilon_1^{R} - \epsilon_2^{R}) \sin 2\beta$$

The principal directions of N_{ij}^{T} or isoclinics are given by:

$$\tan 2\theta = \frac{\sin 2\beta}{\cos 2\beta + \dfrac{C_{\epsilon}\, (\epsilon_1^{\sigma} - \epsilon_2^{\sigma})}{C_{\epsilon}^{R}\, (\epsilon_1^{R} - \epsilon_2^{R})}} \qquad (6.18)$$

(by equation (6.11):

$$= \frac{\sin 2\beta}{\cos 2\beta + \dfrac{C_{\epsilon}\, (\epsilon_1^{\sigma} - \epsilon_2^{\sigma})}{N^{R}}} \qquad (6.19)$$

the total fringe order, as given by equation (6.9), can be shown to be:

$$N^{T} = N^{R} \sqrt{1 + 2 \left[\frac{C_{\epsilon}(\epsilon_1^{\sigma} - \epsilon_2^{\sigma})}{N^{R}}\right] \cos 2\beta + \left[\frac{C_{\epsilon}(\epsilon_1^{\sigma} - \epsilon_2^{\sigma})}{N^{R}}\right]^{2}} \qquad (6.20)$$

In equations (6.18) and (6.20):

* $\theta = 0^\circ$ when $\beta = 0^\circ, 90^\circ$
* $N^T = N^R + N^\sigma \quad (\beta = 0^\circ)$
$= N^R - N^\sigma \quad (\beta = 90^\circ)$

i.e. only when $\beta = 0^\circ$ or 90° fringe orders N^R and N^σ can be algebraically added and the isoclinic direction remains unchanged under the application of σ.

c. Non dimensional forms.

Put:

$$r = \frac{\epsilon_1^\sigma - \epsilon_2^\sigma}{\epsilon_1^R - \epsilon_2^R}$$

$$r' = \frac{C_\epsilon(\epsilon_1^\sigma - \epsilon_2^\sigma)}{N^R} = \frac{C_\epsilon(\epsilon_1^\sigma - \epsilon_2^\sigma)}{C_\epsilon^R(\epsilon_1^R - \epsilon_2^R)} \qquad (6.21)$$

$$= r^C \cdot r \quad \text{where} \quad r^C = \frac{C_\epsilon}{C_\epsilon^R}$$

$$r^N = \frac{N^T}{N^R}$$

equations (6.14), (6.18) and (6.20) can be put as:

$$\tan 2\alpha = \frac{\sin 2\beta}{\cos 2\beta + r} \qquad (6.22)$$

$$\tan 2\theta = \frac{\sin 2\beta}{\cos 2\beta + r'} \qquad (6.23)$$

$$r^N = \sqrt{1 + 2r' \cos 2\beta + r'^2} \qquad (6.24)$$

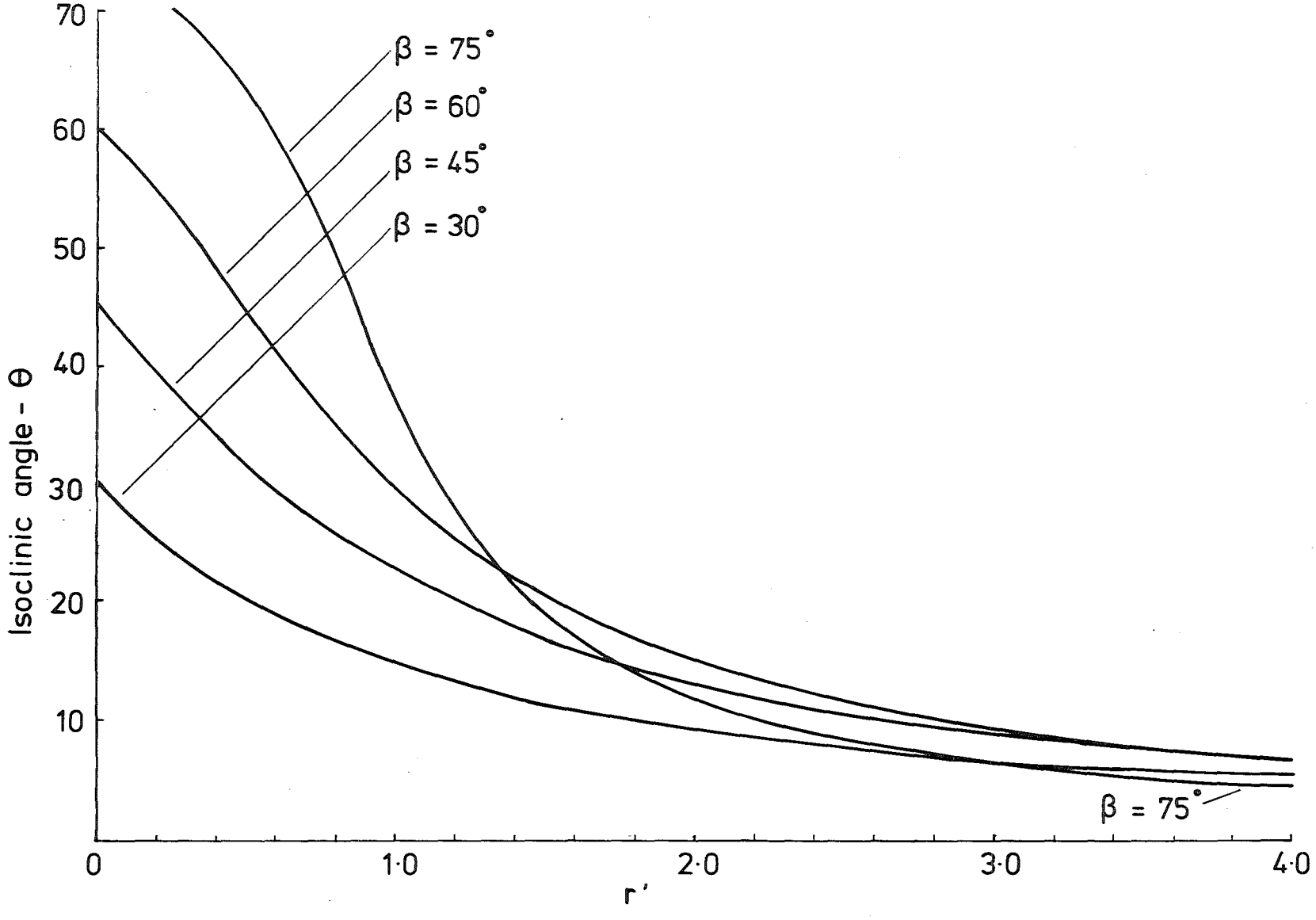

Fig. 6·7 VARIATION OF θ WITH r'

Consider the variation of θ and r^N with r', for a given β. (Note that variation of α with r is similar to that of θ with r').

d. Variation of θ with r'.

From equation (6.23)

$$\frac{\partial\,(\tan 2\theta)}{\partial r'} = \frac{-\sin 2\beta}{(\cos 2\beta + r')^2} \qquad (6.25)$$

$$\leqslant 0$$

The equality sign holds for $\beta = 0$ or $\frac{\pi}{2}$. For $\beta \neq 0$, θ always decreases. As a consequence of eqn. (6.25) and of similarity between (6.22) and (6.23):

$$\tan 2\theta < \tan 2\alpha < \tan 2\beta, \quad \text{as} \quad \frac{r'}{r} = \frac{C_\epsilon}{C_\epsilon^R} > 1 \text{ by Fig. 6.5.}$$

If r tends to ∞, r' also tends to ∞, equations (6.22) and (6.23) give: α, $\theta \to 0$, i.e: when the fringe order N^σ due to the application of stress σ is much larger than the frozen fringe order N^R, the isoclinic directions and principal strain directions approach principal stress directions. If this is to be avoided N^R should be comparable to the maximum N^σ in the isoclinic tests.

The variation of θ with r' is shown in Fig. 6.7 for different values of β.

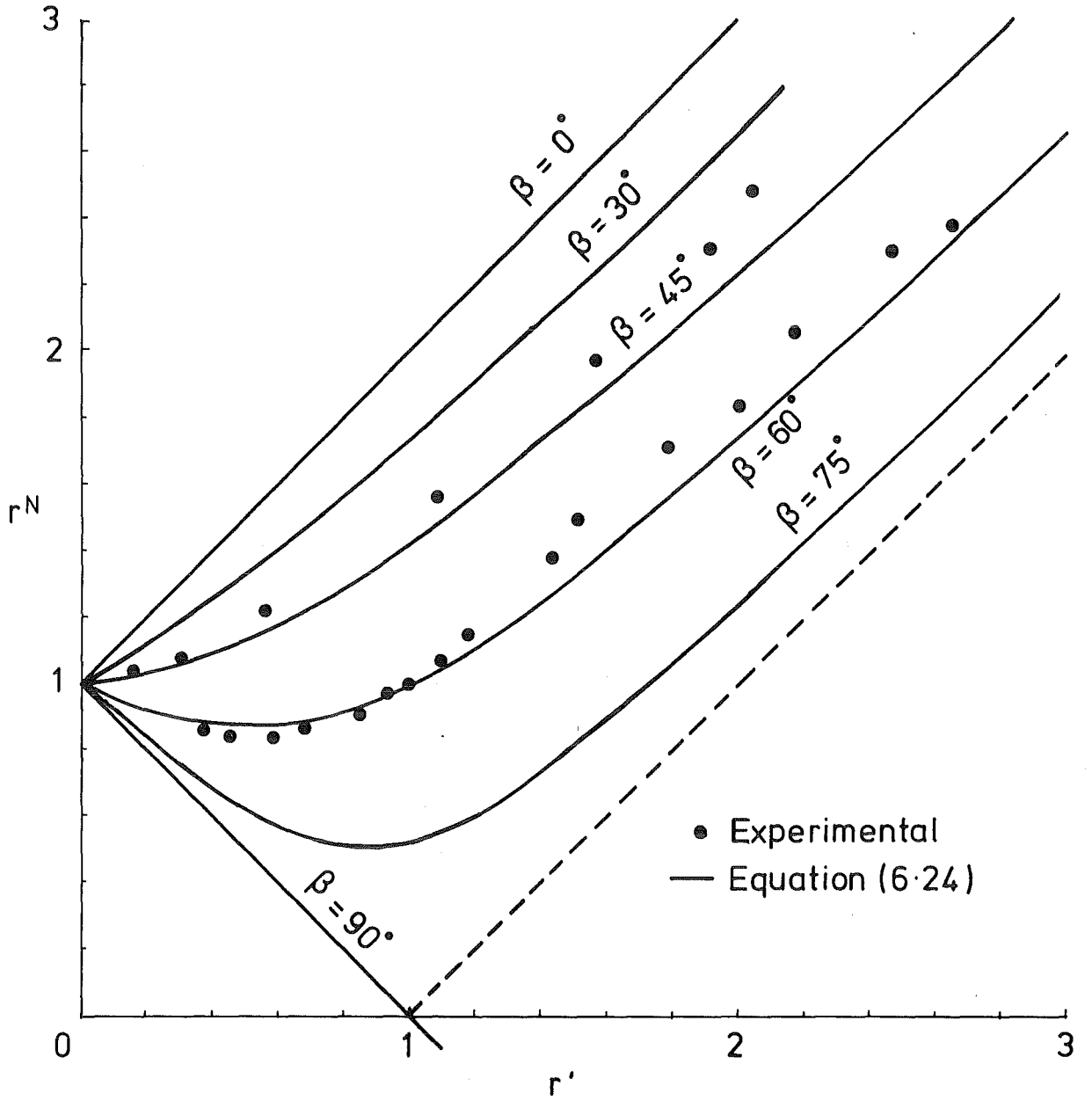

Fig. 6·8 VARIATION OF r^N WITH r'.

c. Variation of r^N with r'.

By equation (6.24):

$$\frac{\partial r^N}{\partial r'} = \frac{r' + \cos 2\beta}{\sqrt{1 + 2r' \cos 2\beta + r'^2}} \qquad (6.26)$$

as $r' > 0$, $\frac{\partial r^N}{\partial r'} = 0$ only if $\beta > \frac{\pi}{4}$ and $\cos 2\beta = -r'$, and it can be shown that this corresponds to a minimum. Equation (6.23) gives the corresponding $\tan 2\theta \to \infty$, i.e. when the total fringe order passes through a minimum, the isoclinic direction is 45°.

For $\beta < \frac{\pi}{4}$, $\frac{\partial r^N}{\partial r'}$ is always > 0 i.e. N^T always increases.

The variation of r^N with r' is shown in Fig. 6.8 for different values of β.

The analysis of effects of errors in β and θ on r' and of errors in r' on r^N is given in Appendix 8.

6.3.3 Experimental methods and apparatus.

In equations (6.21) to (6.24) the following quantities can be experimentally determined: $(\epsilon_1^\sigma - \epsilon_2^\sigma)$, $(\epsilon_1^R - \epsilon_2^R)$, N^R, N^T, α, θ, β, thus allowing r, r^N to be evaluated; r' and hence r^C are evaluated by (6.21) and (6.23).

a. Determination of principal strain difference and principal directions.

Let C_1 be a circle scribed onto the large test piece before it was strain frozen. After being strain frozen C_1

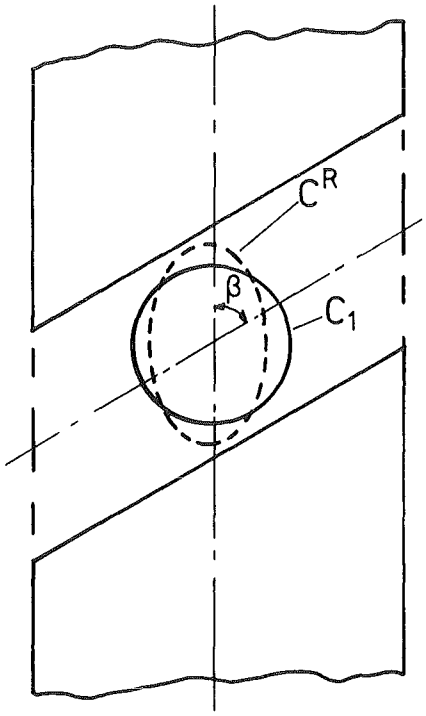

(a) Strain frozen test piece.

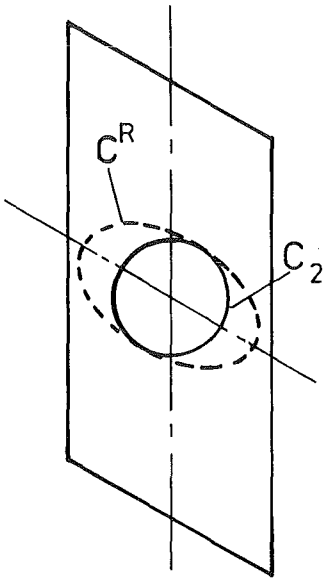

(b) Small test piece - undeformed

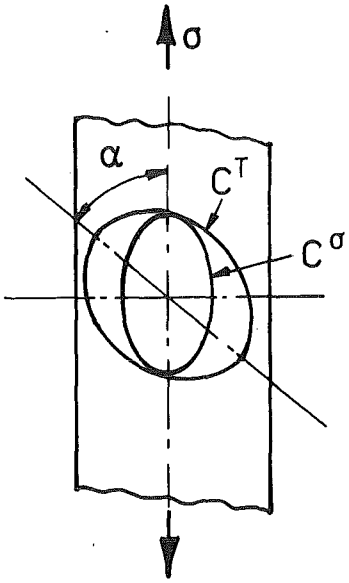

(c) Deformed small test piece.

Fig. 6·9

became an ellipse C^R (Fig. 6.9) $(\epsilon_1^R - \epsilon_2^R)$ could be determined from C_1 and C^R. A smaller test piece, the parallel section of which contained C^R, was cut off the large test piece; and a circle C_2 was scribed onto it. Under the application of stress on the small test piece, C^R and C_2 were deformed into C^T and C^σ respectively; α and $(\epsilon_1^\sigma - \epsilon_2^\sigma)$ could be determined from the major and minor axes of C^T and C^σ.

A large Lexan test piece ($5\frac{1}{2}$" wide) was used for strain freezing (Fig. 6.10). The strain freezing was carried out as outlined in part 6.2.1, except that the loading forks used as shown in Fig. 6.11 were different. The initial stress was 530 psi, and T_{max} was 151°C. The diameter of C_1 was 1" (nominal).

Smaller test pieces (1" wide) were cut at an angle 45° and 60° to the axis of the large test piece, and were scribed with circles C_2 lying just inside C^R and subsequently strained in the loading frame described in Chapter 5. $(\epsilon_1^R - \epsilon_2^R)$ was evaluated from measurements of C_1 and C^R, while α, $(\epsilon_1^\sigma - \epsilon_2^\sigma)$ were determined from photographs of C^T and C^σ. The photographic processing was similar to that described in Chapter 2. In determining principal directions of ϵ_{ij}^T, the following steps were taken:

* the images of ellipses C^T were inspected on the glass screen of the Nikon Shadowgraph to determine the approximate positions of major and minor axes of the ellipse.

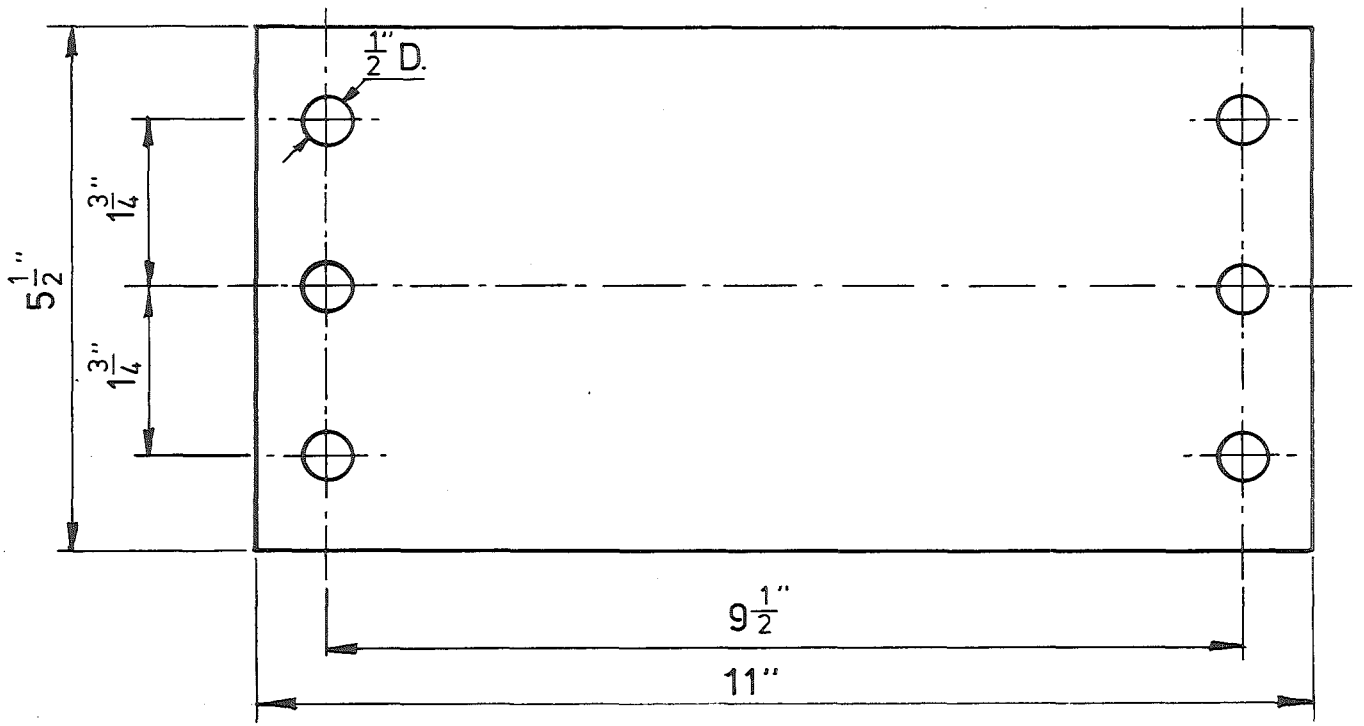

Fig.6·10(a) STRAIN FREEZING TEST PIECE USED IN ISOCLINIC TESTS

* diametral distances (close to major axes) were measured around the approximate position. The scanning was first carried out with 1° rotation between measurements, then with $\frac{1}{2}^{\circ}$ rotation. The maximum measurement was considered to correspond to the principal strain direction (ϵ_1^T) with the corresponding minor axis also aligned at 90° to the major axis. It was found that the reproducibility of α was $\frac{1}{2}^{\circ}$ to 1° depending on the quality of the image.

b. Determination of other data.

The angle β was also measured on the Nikon Shadowgraph; N^R and N^T were determined by a compensation strip and Tardy's method of compensation. The isoclinics were determined accurately within $\frac{1}{2}^{\circ}$.

6.3.4 Results.

A typical tabulation of results is given in Appendix 9 for $\beta = 59^{\circ}\ 45'$.

In the tabulation, r and r' were evaluated by equations (6.27) and (6.29) of Appendix 8.

$$r = \frac{\sin 2\beta}{\tan 2\alpha} - \cos 2\beta \qquad (6.29)$$

$$r' = \frac{\sin 2\beta}{\tan 2\theta} - \cos 2\beta \qquad (6.27)$$

$$r^C = \frac{r'}{r}$$

$$r^N = \frac{N^T}{N^R}$$

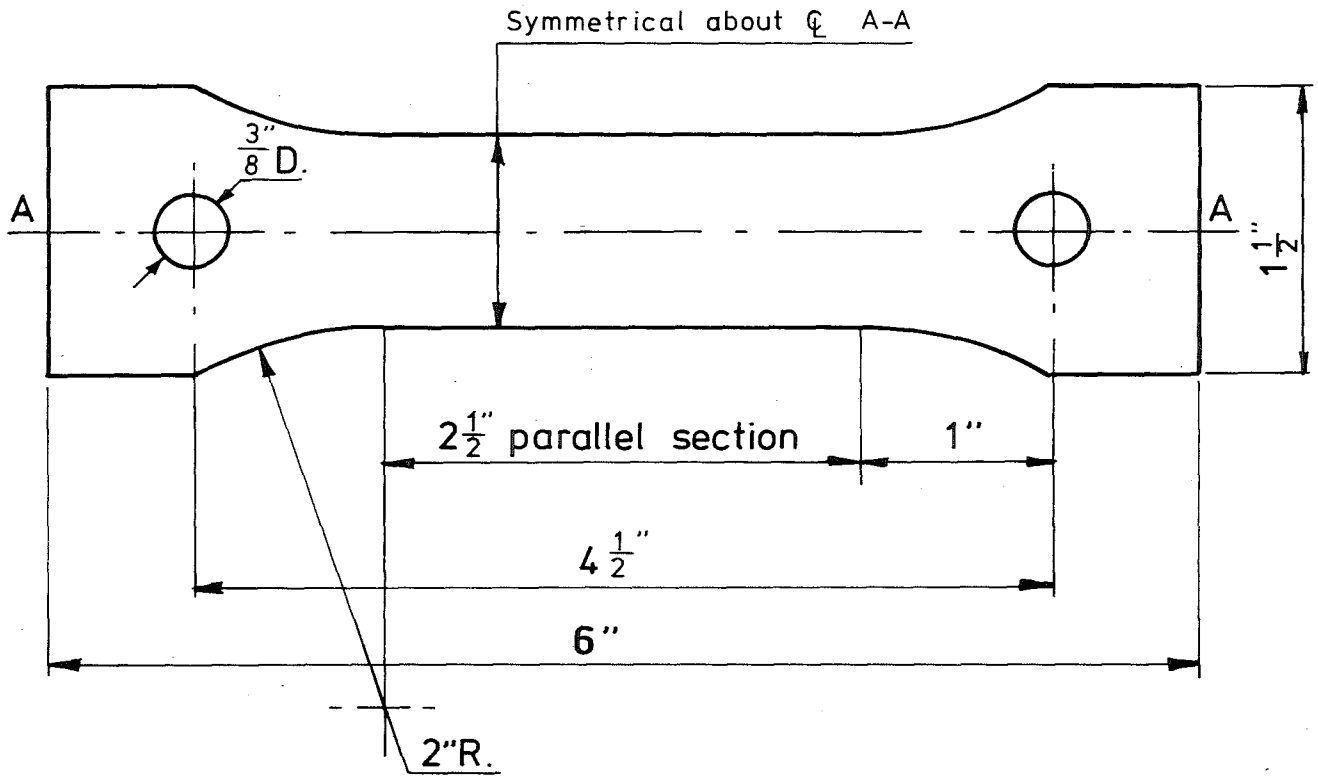

Fig. 6·10 (b) SMALL TEST PIECE USED IN ISOCLINIC TESTS

The value of N evaluated from observed fringe order, is plotted against r' in Fig. 6.8. At $r' > 1$ the experimental values of r^N lie above the curve given by equation (6.24). Better agreement is observed for $r' < 1$. For $\beta = 60^\circ$ and $r' < 1$ most of values of r^N lie below the theoretical curve, a minimum of r^N was observed at $r' \simeq .5$ as pointed out in 6.3.2 while the corresponding isoclinic was 45° as predicted.

The values of $r^C = \frac{C_\epsilon}{C_\epsilon^R}$ are plotted against r in Fig. 6.12, showing a scattering of data about a mean value of approximately 3.0.

The quantity $r(\epsilon_1^R - \epsilon_2^R)$ was also evaluated and plotted against measured $(\epsilon_1^\sigma - \epsilon_2^\sigma)$ in Fig. 6.13. (See equation (6.21)).

To check the assumption that ϵ_{ij}^σ is coaxial to σ, principal directions of ϵ_{ij}^σ were located as outlined in 6.3.3a from which the assumption was found to be valid.

6.3.5 Discussions.

Fig. 6.7 shows that as r' (i.e. r) increases, θ decreases; the rate of change of θ with r' is larger at small r' than at large r', i.e. θ should be accurately determined at large r'. The error analysis in Appendix 8 also shows that at small θ, i.e. at large r', the error $\delta r'$ due to errors in β and θ becomes large.

The accuracy in determining α and r improves with large strain

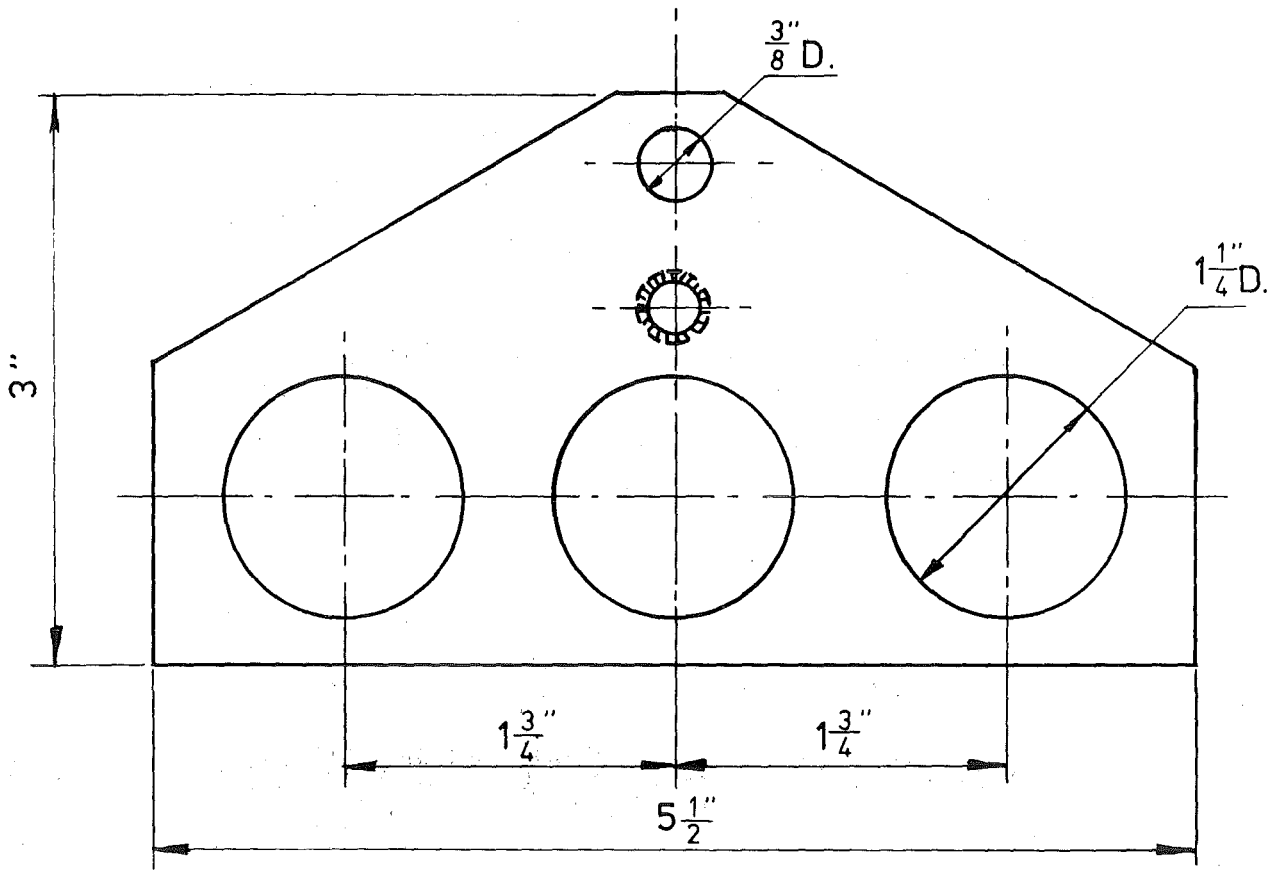

Fig.6·11 LOADING FORKS FOR THE STRAIN FREEZING TEST PIECE USED IN ISOCLINIC TESTS.

as shown by Fig. 6.13.

In other words: at small $(\epsilon_1^\sigma - \epsilon_2^\sigma)$, due to application of the stress σ, values of r are not as accurate as at large $(\epsilon_1^\sigma - \epsilon_2^\sigma)$, but the effects of error in β and θ on r' become pronounced at large $(\epsilon_1^\sigma - \epsilon_2^\sigma)$. The values of r^C are thus sensitive to errors at both small and large values of $(\epsilon_1^\sigma - \epsilon_2^\sigma)$. It was also found that at large values of $(\epsilon_1^\sigma - \epsilon_2^\sigma)$, the fringe pattern in the parallel section of the test piece became non-uniform and the isoclinic directions were not distinct, the error in determining θ being more than $\frac{1}{2}^\circ$.

In Fig. 6.8 for $\beta = 60^\circ$ and $r' > 1$ and for $\beta = 45^\circ$, an error $\delta r' \simeq -.10$ would account for the apparent shift of experimental results to the left of the theoretical curves. This error in r' also reduces values of r_C. From Fig. 6.12 $r^C \simeq 3.0$, for a mean value $C_\epsilon^R = 1.63 \times 10^3$ fringe/in, $C_\epsilon = 4.9 \times 10^3$ fringe/in. This value is low compared with those obtained in Chapter 5, the discrepancy could be due to error in r' and r as discussed above, or to the fact that C_ϵ decreases at large $(\epsilon_1^\sigma - \epsilon_2^\sigma)$ (Chapter 5), giving smaller r' (by equation 6.21).

The accuracy would be improved if larger β was used as shown in Appendix 8, and if isoclinics were more accurately determined. Furthermore, as shown above if large $(\epsilon_1^R - \epsilon_2^R)$ is used, α is accurately determined at large $(\epsilon_1^\sigma - \epsilon_2^\sigma)$ without making r large (i.e. r' large), so as to make effects of

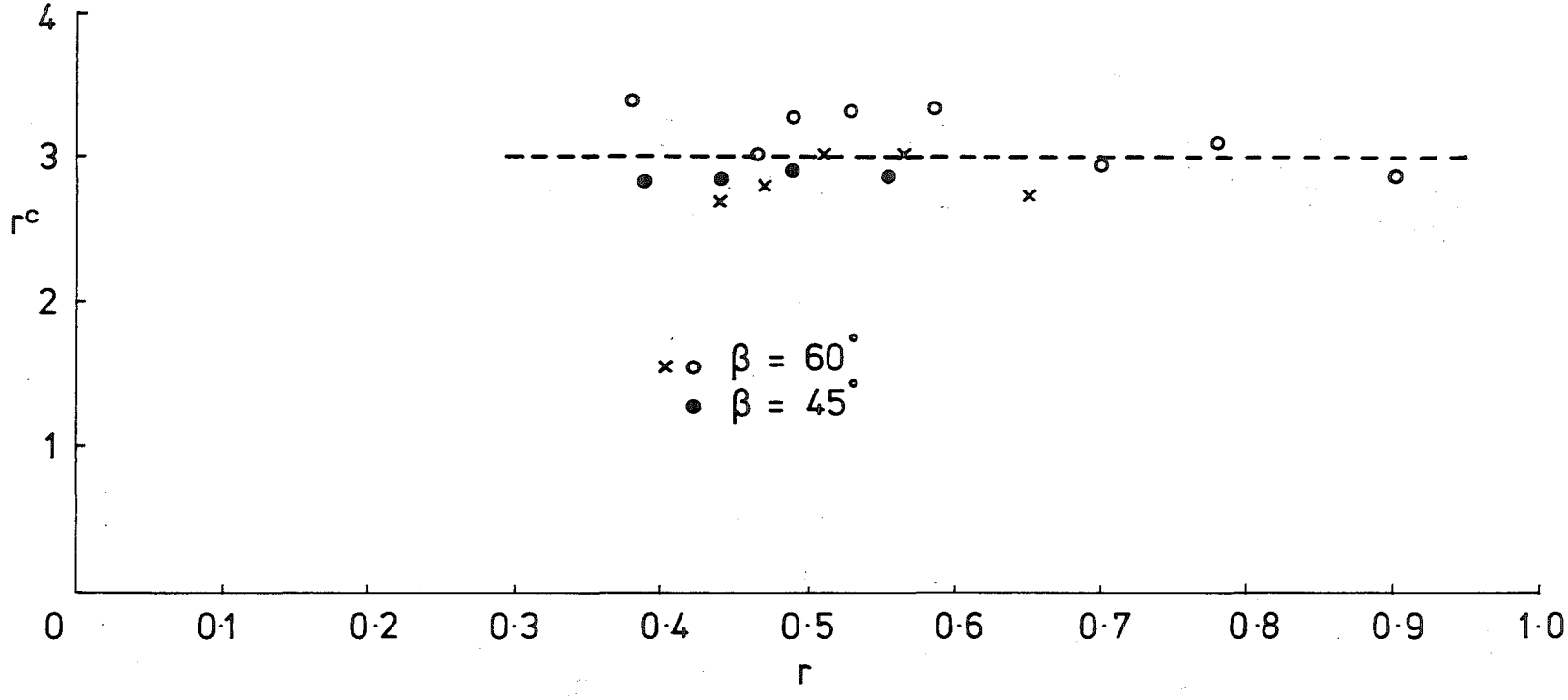

Fig. 6·12 RATIO OF STRAIN-FRINGE COEFFICIENTS – RATIO OF PRINCIPAL STRAIN DIFFERENCE.

errors in β and θ r' pronounced. The range of $(\epsilon_1^R - \epsilon_2^R)$ exployed was .096 - .110.

6.4 CONCLUSIONS

Mechanical non-coincidence in plane stress was effected by straining a strain frozen test piece in uniaxial tension at room temperature. The test piece was cut at angles 45° and 60° to the axis of a large test piece which had been strain frozen in uniaxial tension. The isoclinic directions and total fringe order observed, could be explained by applying tensor transformation law to the birefringent response of frozen strain and of the strain due to stress σ. The analysis shows that under deformation, the isoclinics direction θ depends on β and the ratio of fringe order due to ϵ_{ij}^{σ} to N^R (equation (6.23)). The angle θ is always smaller than the principal direction α of the total strain tensor ϵ_{ij}^T; θ and α both tend to zero as $(\epsilon_1^{\sigma} - \epsilon_2^{\sigma})$ increases to infinity. Experimental results compared favourably with the analysis in intermediate range of r'; at small θ errors in isoclinics affected r' greatly and the values of r^C and hence C_ϵ showed scattering due to sensitivity of r at small strain and of r' at large strain. Large β^* , $(\epsilon_1^R - \epsilon_2^R)$and more accurate determination of isoclinics would improve the results.
The tests conducted here verify indirectly that in an isothermal

* other researcher used: $\beta = 32^{\circ}$(14,20), 40-50°(10a).

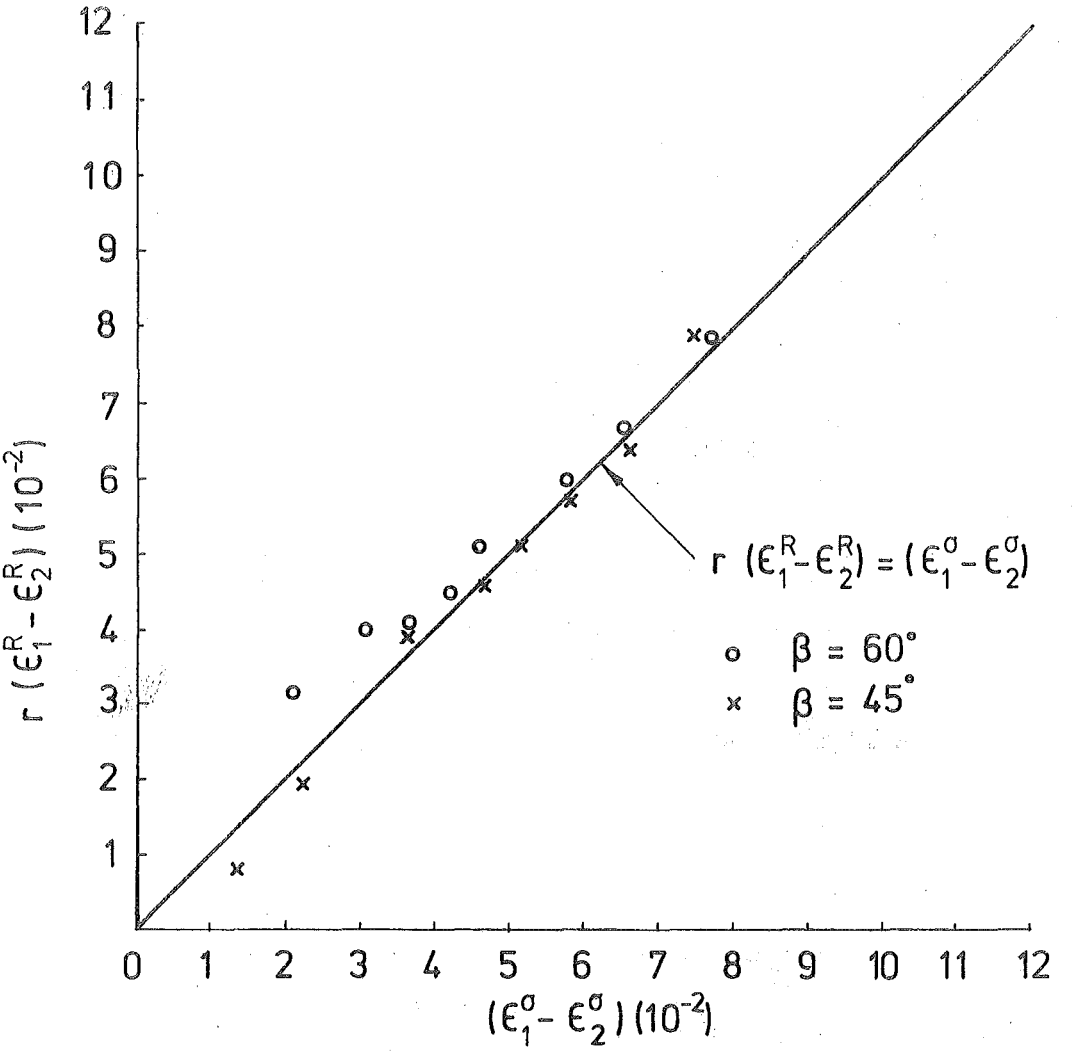

Fig. 6·13 PREDICTED STRAIN VERSUS MEASURED STRAIN

deformation:

$$N_{ij} = C_{\epsilon}(T)\ \epsilon_{ij}.$$

In strain-freezing tests, it was shown that the apparent strain-fringe coefficient for a particular thermal cycle decreases with the temperature during the heating period as does $C_{\epsilon}(T)$, in agreement with the observation in Chapter 3. The increase of fringe order and strain during a strain-freezing experiment was found to be irreversible. The residual strain-fringe coefficient C_{ϵ}^{R}, for the thermal cycle adopted, was found to be dependent on the maximum temperature of the cycle and not on the initial stress level, for values of stress up to 750 psi.

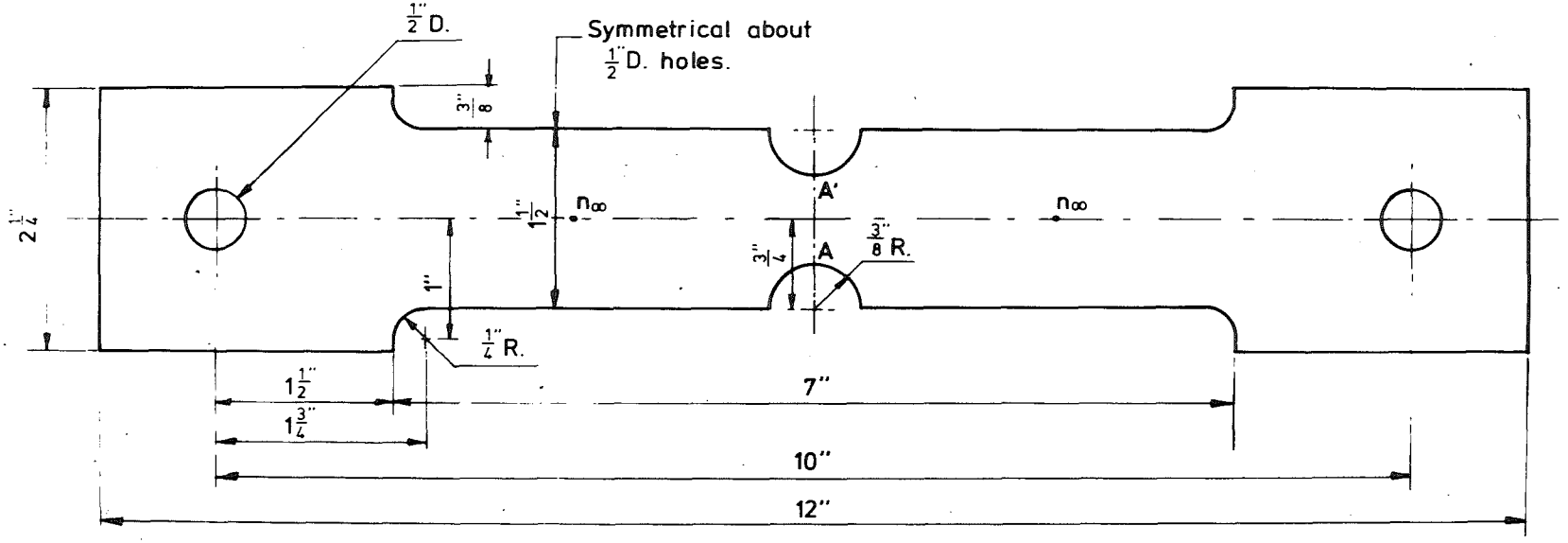

Fig. 7·1(a) PLATE WITH SEMICIRCULAR GROOVE

CHAPTER 7

TENSILE STRIPS WITH SEMI-CIRCULAR GROOVES OR CIRCULAR HOLE

7.1 INTRODUCTION

Tensile strips with notches have been investigated by many researchers in plasticity and photoplasticity. Notches in the form of semi-circular grooves or circular holes were selected for study. Experiments in Chapters 5 and 6 showed that during an isothermal deformation, the fringe order is proportional to the difference of secondary principal strains and that the isoclinics are related to secondary principal strain directions.

In the study, the thickness of the strips was small compared to other dimensions and a plane stress condition can be assumed to exist. The strain field is, however, not biaxial as the lateral strain is not zero.

It can be shown that by a combination of the oblique incidence method devised by Drucker[98,99] and by measuring the lateral strain, the principal strains ϵ_1, ϵ_2 in the plane (x, y) of the test piece can be separated, hence ϵ_x, ϵ_y and ϵ_{xy} can be evaluated. Analysis of stress can be carried out by applying plasticity laws to inelastic behaviour of polycarbonate. Although works by Williams and Ford[100], Sidebottom and co-workers[101,102] show that plasticity laws can be successfully applied to inelastic stress-strain analysis of glassy

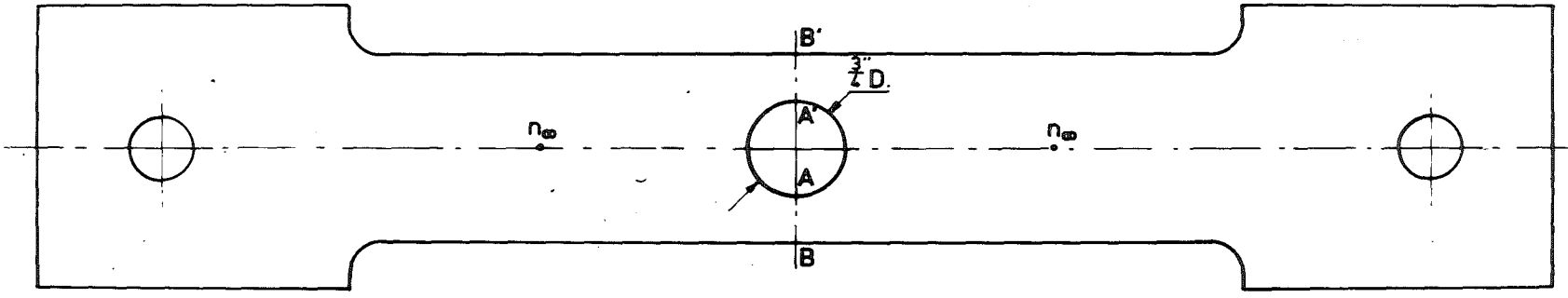

All other dimensions same as Fig. 7·1 (a)

Fig. 7·1 (b) PLATE WITH CIRCULAR HOLE

polymers, such procedures were not pursued.

Here, tensile strips were strained or loaded at constant load with strains and fringe patterns recorded, to give the photomechanical relationship in a biaxial stress field and to illustrate the inelastic behaviour of polycarbonate.

7.2 EXPERIMENTAL METHODS AND APPARATUS

A ratio $\frac{d}{b} = \frac{1}{2}$ was chosen, where d is the diameter of the circular notch and b is the width of the parallel section. This ratio was used by several researchers, notably Theocaris [103-105] and Jarvornicky[36]. All test pieces were cut on a milling machine. In order to avoid premature failure at the $\frac{1}{2}$" diameter holes, serrated grips were used, similar to those used in tensile tests (Chapter 5), Fig. 7.1.
The free square corners permit integral fringe orders to be determined from a photograph of the isochromatic pattern.
The loading fork is shown in Fig. 7.2. Strain was determined by the Moiré fringe method. A 133 L.P.I. orthogonal grid was photoengraved on the test piece. The Moire fringes produced by superimposing an analyser onto the specimen grid was found to be of insufficient contrast for measurements on the Nikon Shadowgraph. The specimen grid was thus photographed with a white reflector at the back (Fig. 7.3). It was found that by using Kodaklith Royal Ortho film developed in Kodaklith fine line developer, a high contrast, even dot-quality image of the specimen grid could be obtained. The negatives of the speci-

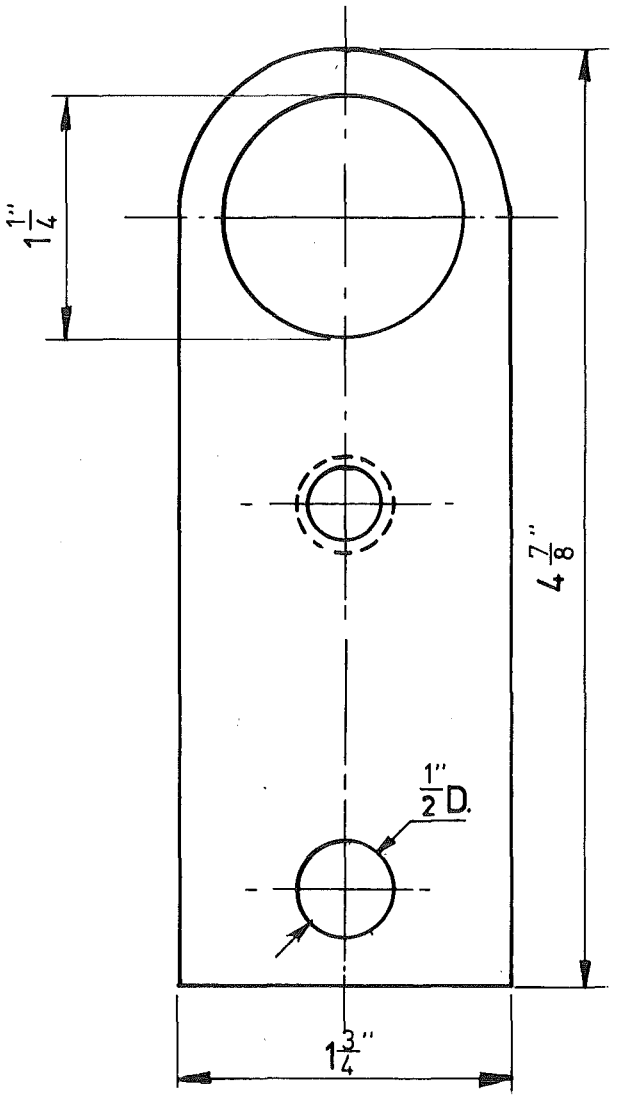

Fig. 7·2 LOADING FORKS

men grid were superimposed onto a 142 L.P.I. analyser grid on the table of the Shadowgraph, the resulting Moiré fringes were analysed as set out in Chapter 4 and Appendix 6.

All experiments were conducted at room temperature of 20°C.

7.3 RELATIONSHIP OF FRINGE ORDER - PRINCIPAL STRAIN DIFFERENCE IN PLANE STRESS.

A tensile strip with semi-circular groove and two tensile test pieces (Fig. 5.18) were cut off a Sharples Makrolon sheet (.175" thick) and were strained in the loading frame. The tensile test pieces were studied in the same manner in part 5.9. For the tensile strip photographs of isochromatic patterns and specimen grid were taken from which the values of fringe order and principal strain difference were determined and plotted in Fig. 7.4. Data from uniaxial stress and biaxial stress are in good agreement especially in the range $(\epsilon_1 - \epsilon_2) > .03$, the scattering below this strain level probably being due to error in determination of strain values. It was found that Sharples Makrolon was more brittle than Bayer Makrolon and Lexan, and its strain-fringe coefficient is approximately 6.2×10^3 fringe/in, in comparison with 5.2×10^3 fringe/in and 5.6×10^3 fringe/in for Bayer Makrolon and Lexan respectively.

At large $(\epsilon_1 - \epsilon_2)$ the fringes were so crowded at the groove that the isochromatic pattern formed Moiré fringes with

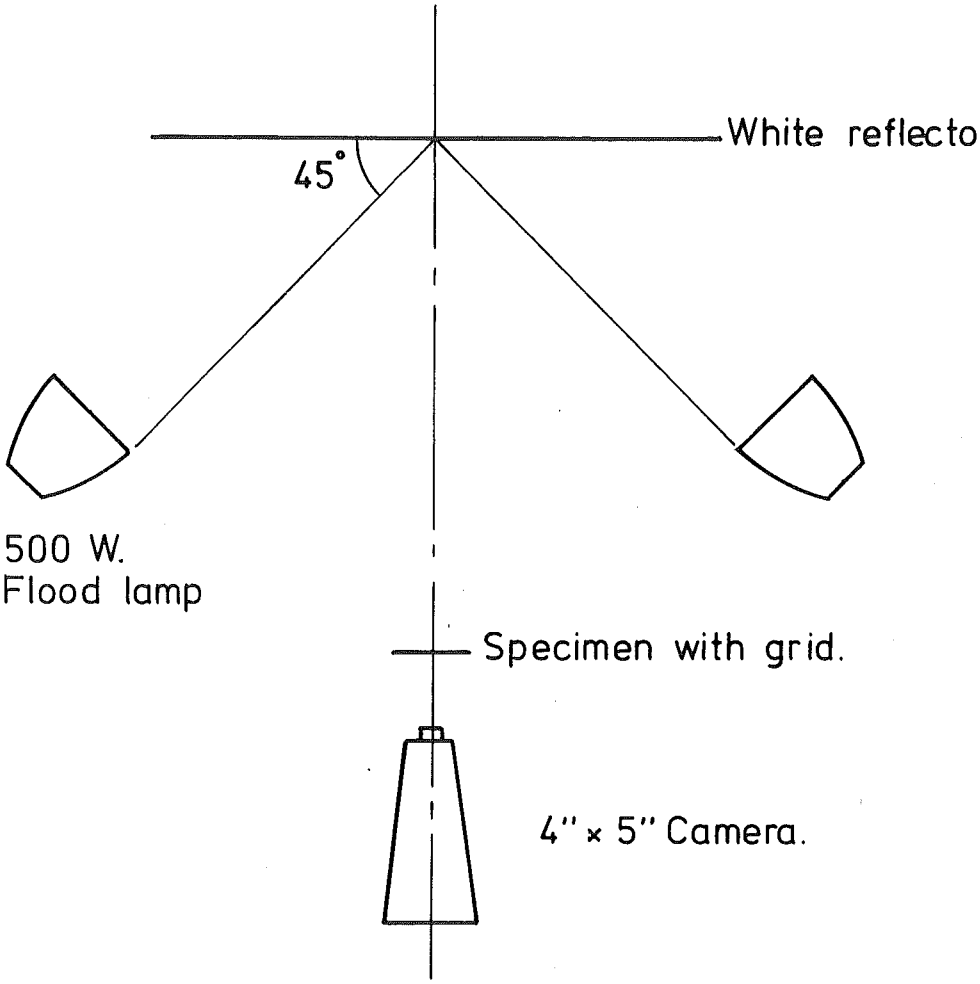

Fig.7·3 EXPERIMENTAL SET UP FOR PHOTOGRAPHING SPECIMEN GRID.

the 133 L.P.I. specimen grid. This could be avoided by using thinner sheet or finer grid.

7.4 TENSILE STRIPS UNDER CONSTANT LOAD

Tensile strips with circular hole and semi-circular grooves were cut from Lexan sheets (.042" thick) and loaded by deadweight in the loading frame. The loading rate was approximately 400 psi/min, similar to that of creep tests (Chapter 5). When the required load was reached the tensile strips were allowed to deform at constant load. The isochromatic and isoclinic fringes were photographed at frequent intervals and the negatives were inspected on the Nikon Shadowgraph. The integral fringe order was determined from the negatives while the fractional fringe order at points of interest was given by the Tardy method of compensation. Because the variation in thickness was very small, the fringe order n as observed was used instead of the fringe order per unit optical path N. Two fringe orders of interest are the maximum fringe order n_{max} and the fringe order n_{∞} in the parallel section and at a distance from the notch (Fig. 7.1).

To facilitate comparison of the loading state in the tensile strips the average stress in the minimum section was used:

$$\sigma_{min} = \frac{\text{Load}}{(b - d).h}$$

where h is the thickness of the strip.

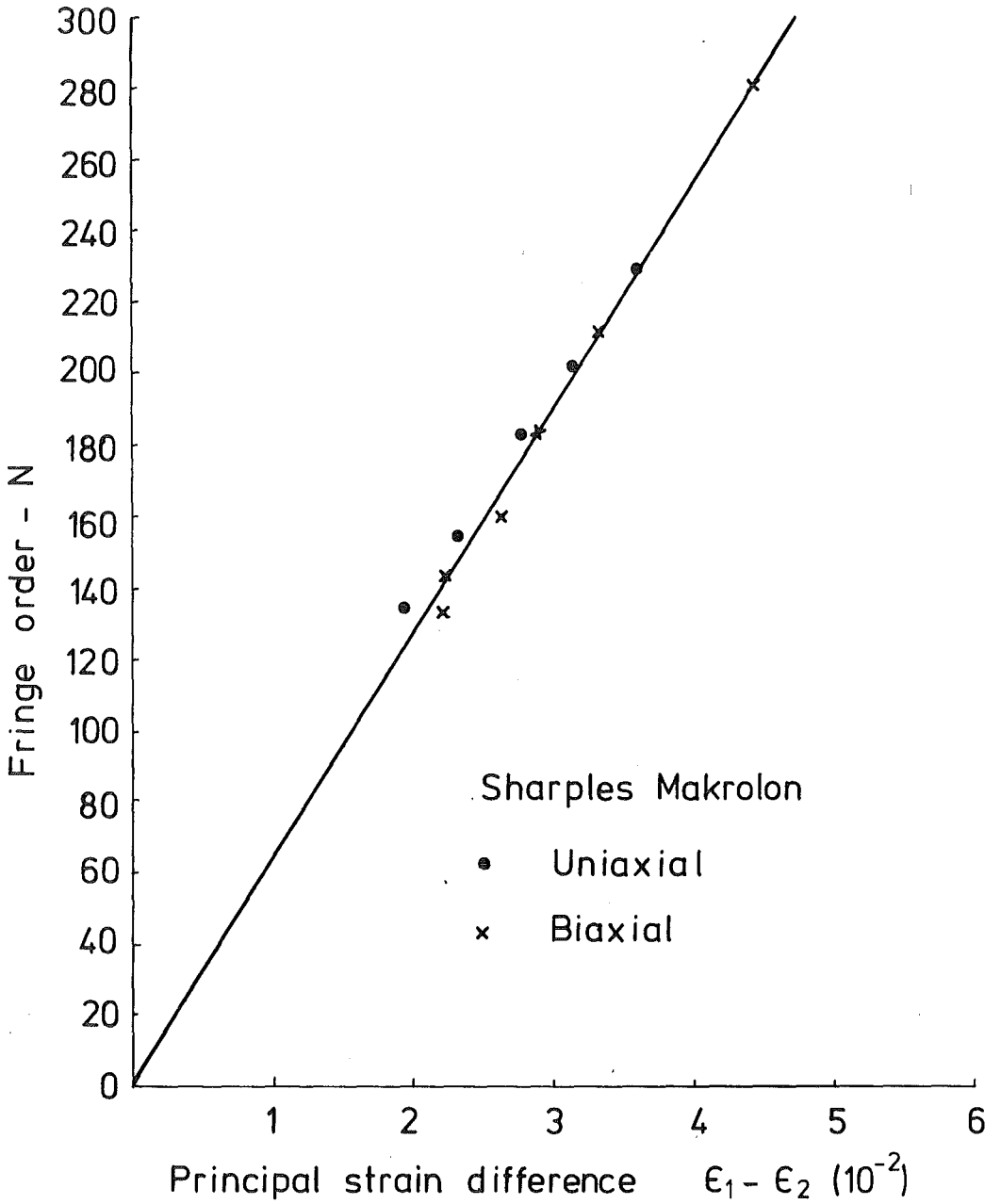

Fig. 7·4 FRINGE ORDER-PRINCIPAL STRAIN DIFFERENCE.

For the geometry adopted, b = 2d, therefore: $\sigma_{min} = 2\sigma_{\infty}$ where σ_{∞} is the stress in the parallel section corresponding to n_{∞}. The stress concentration factor is commonly defined as

$$K_{\sigma} = \frac{\sigma_{max}}{\sigma_{min}}$$

where σ_{max} is the maximum stress.

The elastic stress concentration factors of the tensile strips adopted here are 1.6 and 2.1 for the semi-circular grooves and circular hole respectively.

The value of σ_{min} for tensile strip with circular hole and semi-circular grooves was selected to be 5810 and 7950 psi respectively, so that upon completing the loading the maximum fringe order was the same as found in uniaxial tensile tests.

7.4.1 Variation of Fringe Order with Time.

As σ_{∞} was smaller than 4200 psi in all cases the variation of n_{∞} with time was small.

The isochromatic patterns of the tensile strip with circular hole are shown in Figs. 7.5 and 7.6, the distribution of fringe order on the line A B is plotted in Fig. 7.7. After a period of 2 hours the maximum isochromatic fringe at A was slightly affected by local stress raisers on the boundary of the hole. This is in marked contrast to the case of semi-

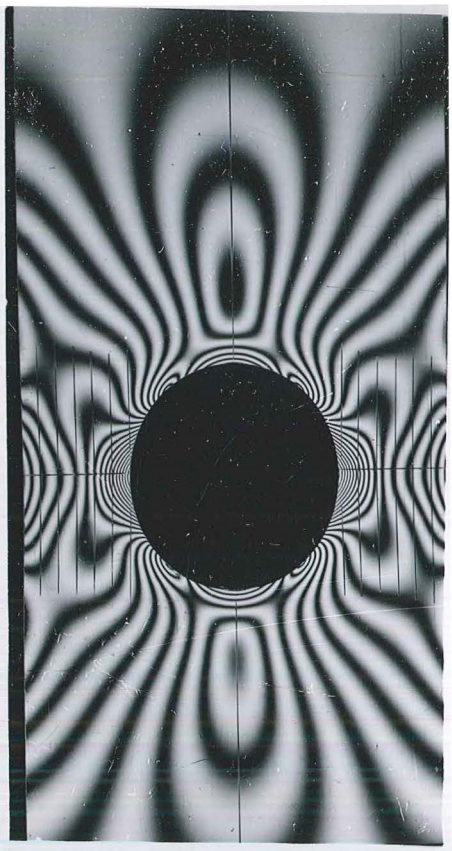

Fig. 7·5 t_i = 1 hour

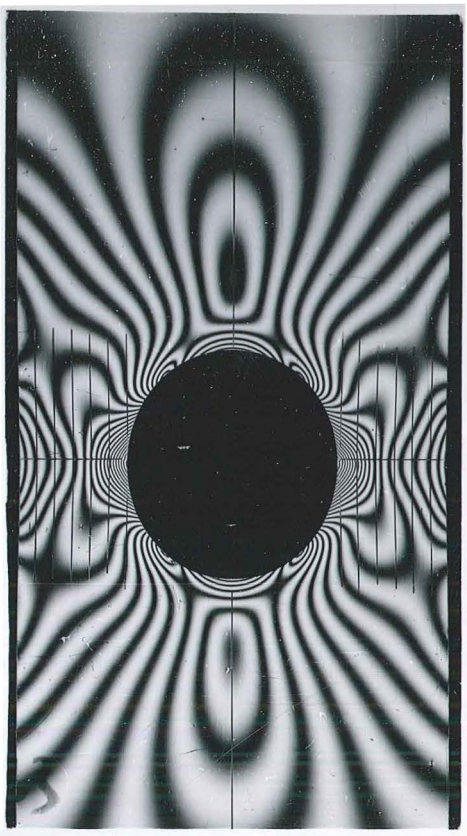

Fig. 7·6 t_i = 12 hours

ISOCHROMATIC PATTERNS - TENSILE STRIP WITH CIRCULAR HOLE.

circular grooves which were cut by a milling cutter as opposed to a boring bar used for the holes. The tool marks in milling the semi-circular grooves influenced the isochromatic pattern considerably, and after a period of one hour a yield zone started to develop. The variation of fringe order on line A-A' in the semi-circular groove is shown in Fig. 7.8. The change of fringe order with time is considerably more than that in the case of the circular hole.

The distribution curves of fringe order along AA' were, however, similar for different times t_i. This is different to the behaviour of celluloid as shown by Jarvornicky[36]: the fringe order distribution along AA' is more even with increasing t_i.

As the fringe order is proportional to $(\epsilon_1 - \epsilon_2)$ or the maximum shear strain, and as loading was proportional, Figs. 7.7 and 7.8 also represent the distribution of maximum shear strain and shear stress along A-A'. They are similar to the distribution curves given by Theocaris[103,105] for elastic-perfectly plastic material. A detailed comparison was not possible because of different behaviour of materials and loading. It should be noted that only data prior to the starting of the yield zones was used.

7.4.2 Maximum-shear-strain concentration factor.

As the fringe order is proportional to the maximum shear strain, the isochromatics are loci of points of equal maximum

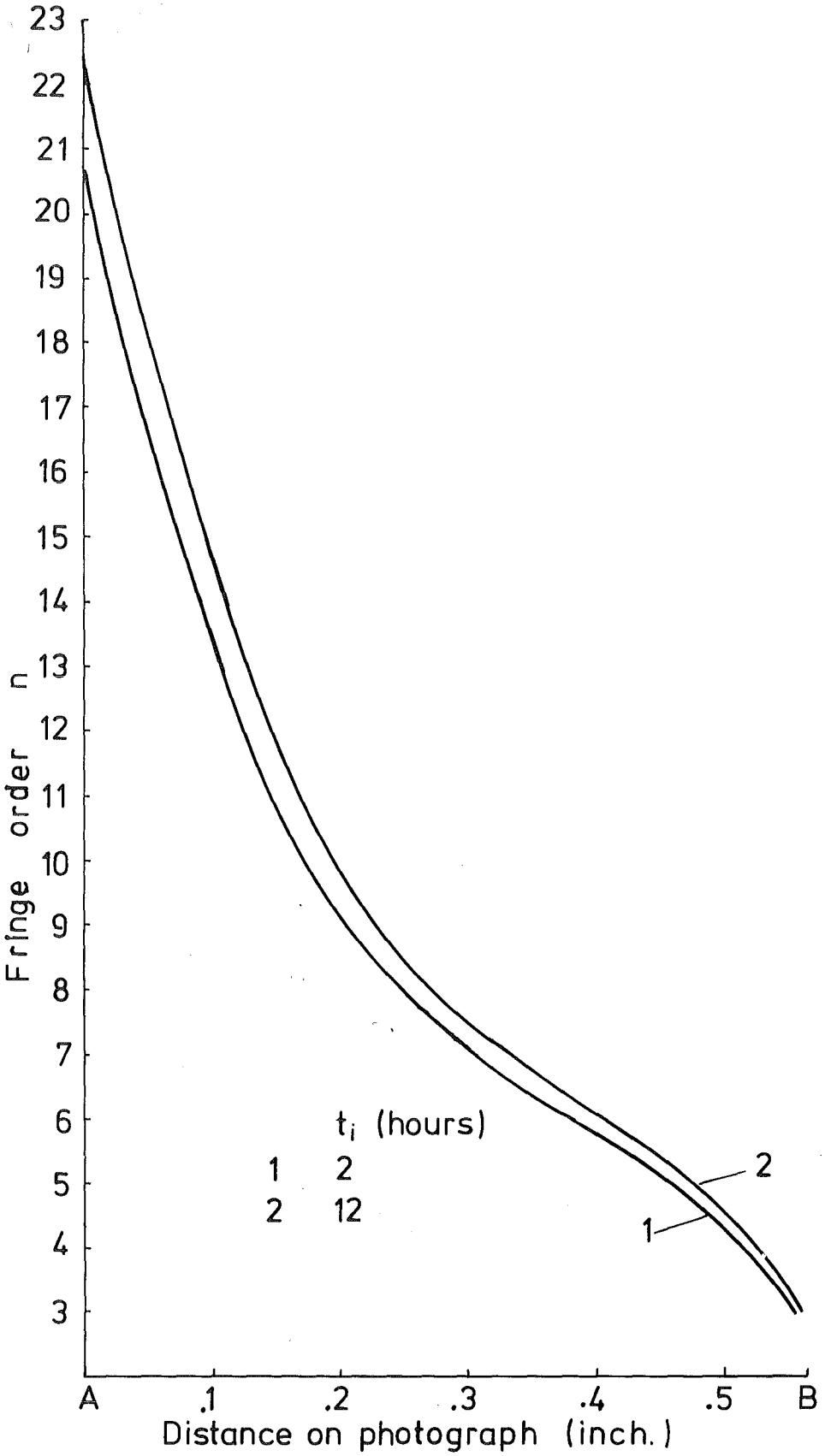

Fig. 7·7 VARIATION OF FRINGE ORDER WITH TIME — TENSILE STRIP WITH HOLE.

shear strain. The maximum shear strain concentration factor is defined as :

$$K_\gamma = \frac{n_{max}}{n_\infty}$$

The variation of K_γ with time is shown in Fig. 7.9.

It can be seen that when a loading member is subjected to constant load the maximum shear strain concentration factor increases with time, while it is well known that stress concentration factor decreases with increasing inelastic deformation.

7.4.3 Yield Zones.

In the case of the semi-circular groove, after one hour two yield zones of width approximately .036" developed on one side of line AA', and progressed to the centre while remaining at right angles to the load line of the tensile strip and at constant width, Figs. 7.10 and 7.11. Another adjacent zone of same width developed on the other side of the line AA' after $2\frac{1}{2}$ hours, Fig. 7.12. The first two yield zones joined up after three hours, Fig. 7.13, and at this instant the test piece was unloaded. The residual isochromatic pattern is shown in Fig. 7.14. The fact that the width of yield zones was approximately equal to the thickness of the tensile strip was also noted by Brinson[35]. Brinson also obtained parallel isochromatics in the yield zones. This could be attributed to a gradual variation of thickness or principal

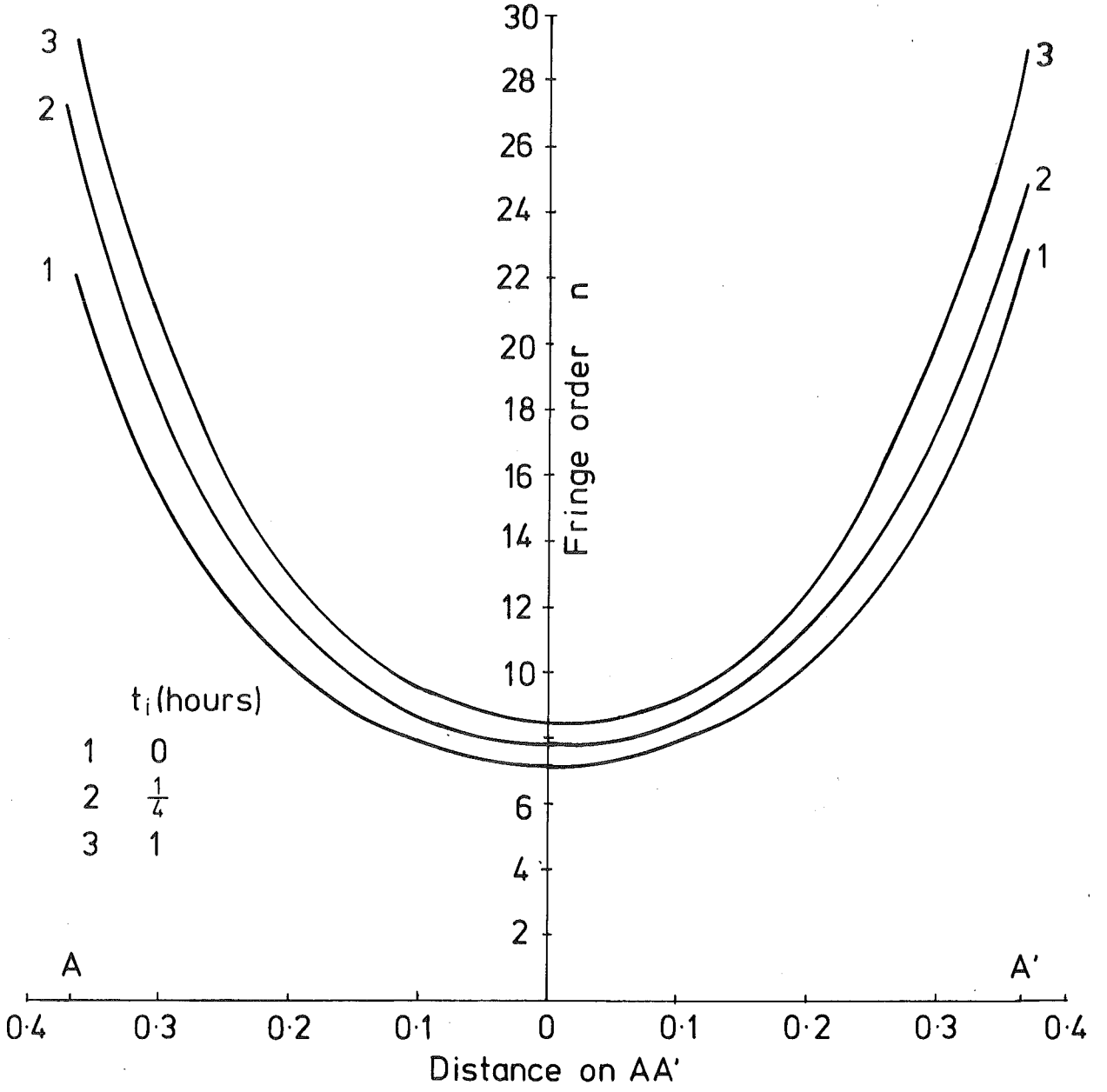

Fig. 7·8 VARIATION OF FRINGE ORDER WITH TIME TENSILE STRIP WITH SEMI-CIRCULAR GROOVE.

strain difference along the yield zones.

Another tensile strip with semi-circular grooves was loaded to $\sigma_{min} = 8250$ psi. A yield zone developed on one side of AA' at five minutes after loading was completed and was immediately joined by an adjacent zone on the other side of AA'. Another yield zone also developed from the opposite groove. The yield zones joined up after 30 minutes and the tensile strip failed after 45 minutes. The isochromatic pattern immediately before failure is shown in Fig. 7.15.

It was found that in both test pieces, yield zones developed when n_{max} was approximately 29 and they were of the same width. It can be tentatively concluded that yield zones develop with a value of maximum shear strain γ of order .10 is reached. Approximately the same value was found in uniaxial tensile tests in Hounsfield tensometer and from data given by Bayer(106).

7.5 CONCLUSIONS

As expected, photomechanical data obtained in biaxial plane stress and uniaxial tensile stress showed a linear relationship between the fringe order and the principal strain difference. The coefficient of proportionality or the strain-fringe coefficient depends on the condition of the polycarbonate material. Sharples Makrolon appears to be more optically sensitive and more brittle than Bayer Makrolon and Lexan. The scarcity of materials did not allow extensive

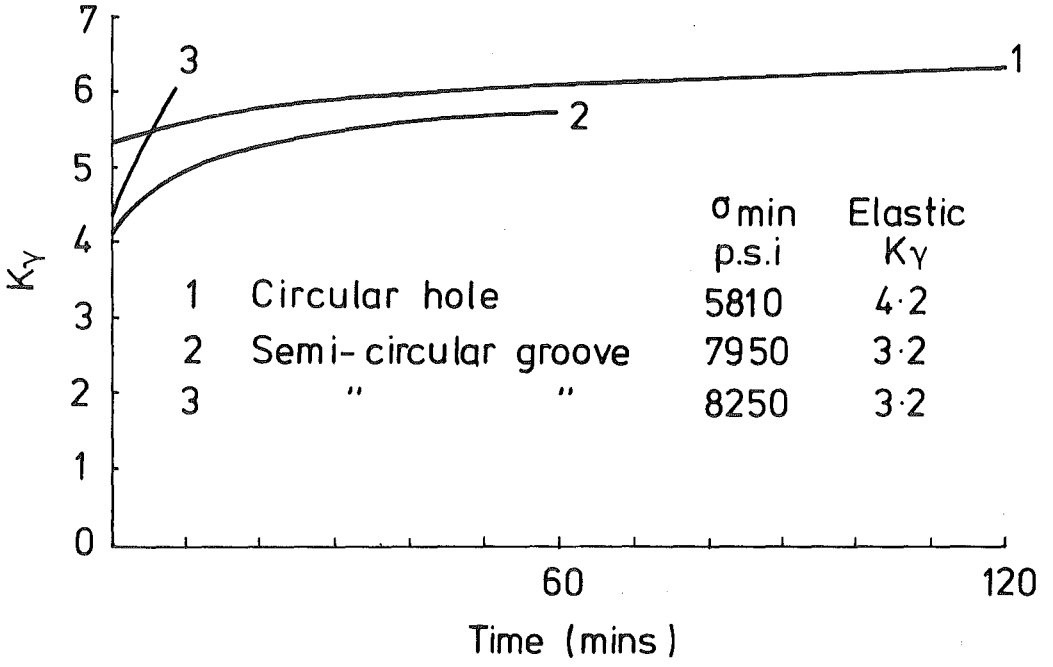

Fig. 7·9 VARIATION OF K_γ WITH TIME

biaxial tests with Bayer Makrolon and Lexan. In plane stress the isochromatics and isoclinics observed at normal incidence are not sufficient for a separation of principal strains. Such a separation can be carried out by using a combination of the oblique incidence method and lateral strain measurement. Stress analysis using birefringence data and plasticity laws can also be carried out after verifying the application of plasticity laws to the inelastic behaviour of polycarbonate. However, from normal incidence isochromatics, the maximum shear strain concentration factor and distribution of maximum shear strain were obtained and interesting features in the propagation of yield zones were observed.

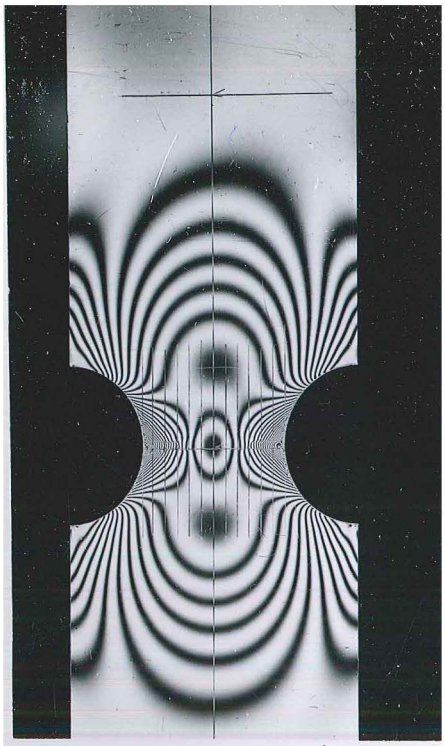

Fig. 7·10 $t_i = 1\frac{1}{2}$ hours

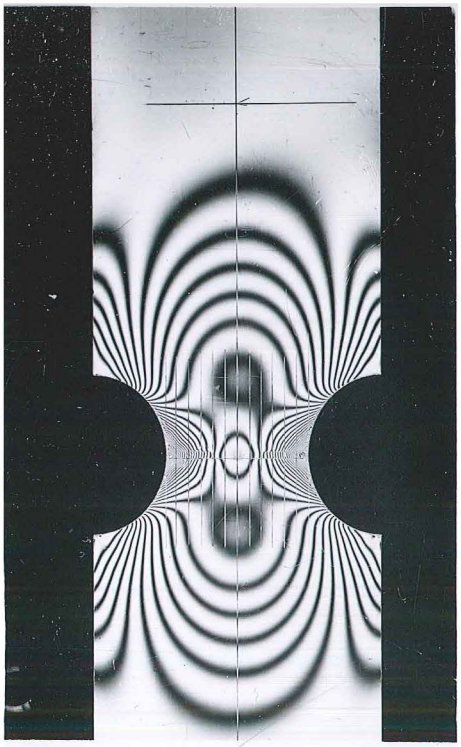

Fig. 7·11 $t_i = 2$ hours

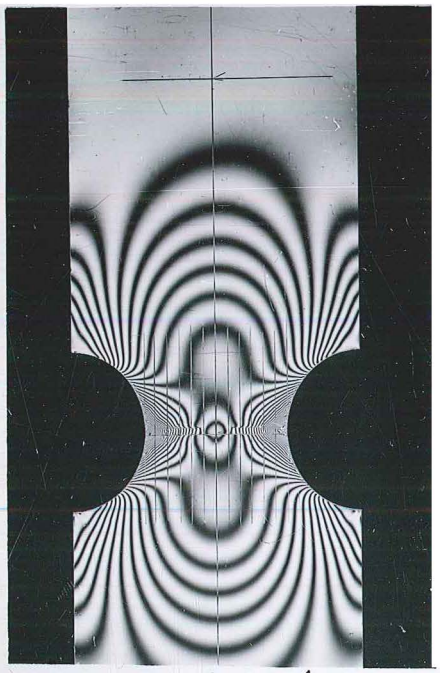

Fig. 7·12 $t_i = 2\frac{1}{2}$ hours

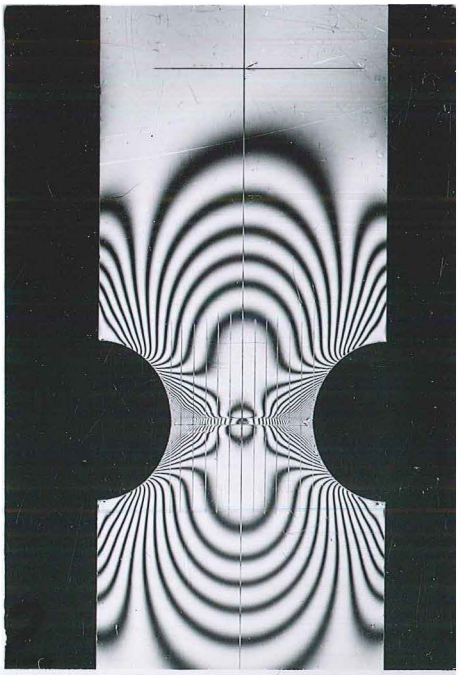

Fig. 7·13 $t_i = 3$ hours

ISOCHROMATIC PATTERNS - TENSILE STRIP WITH SEMICIRCULAR GROOVES - SHOWING PROPAGATION OF YIELD ZONES.

CHAPTER 8

CONCLUSION

This project was initiated in order to extend the techniques of photoelasticity to plasticity of metals. In post-elastic behaviour the application of data from a photomechanical model to the prototype requires the study of inelastic behaviour of the model material and the formulation of similarity criteria.

When polymers are employed as model materials the photomechanical relationship can be studied from the mechanisms of response of deformation and of birefringence to the application of stress and temperature. It was established that the birefringence is predominantly related to the orientation of certain optically sensitive groups, and it is only when these groups form all or most of the main chain of the polymer that birefringence and deformation are intimately related.

In the case of polycarbonate of bisphenol A, consideration of the molecular structure suggested that in an isothermal deformation, the index tensor is a linear function of the strain tensor. For the range of strain and birefringe studied it is adequate to use the first order approximation of the photomechanical relationship. That is to say that the fringe order per unit optical path N is proportional to the difference of the secondary principal strains and that the isoclinics

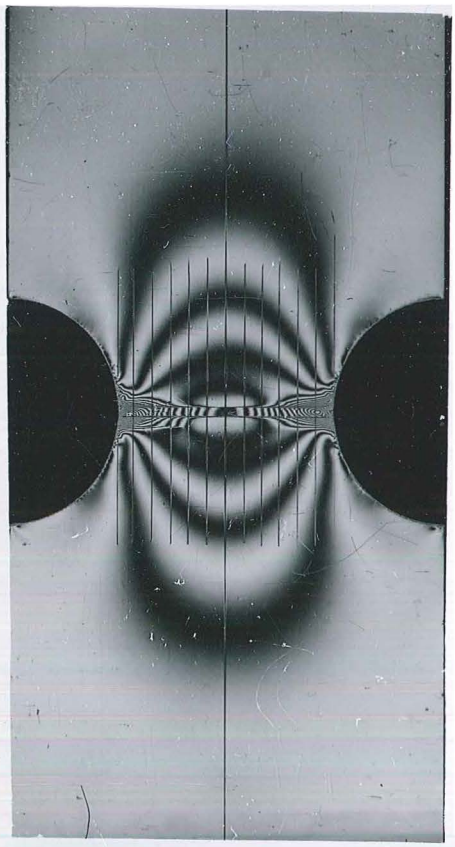

Fig. 7·14
RESIDUAL
ISOCHROMATIC PATTERN

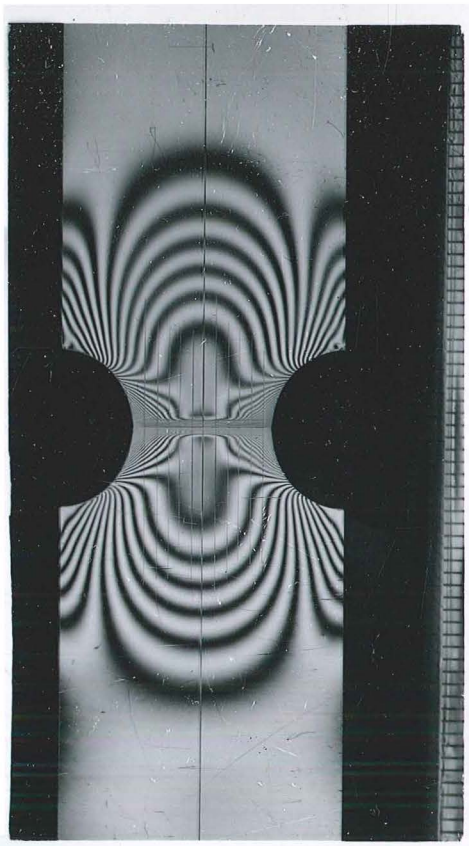

Fig. 7·15
ISOCHROMATIC PATTERN
BEFORE FAILURE σ = 8250p.s.i

represent the secondary principal strain directions. The strain-fringe coefficient should decrease with increasing temperature and may also decrease slightly, during an isothermal deformation, at large deformation. Uniaxial tensile creep and stress relaxation tests at room temperature, strain freezing experiments, experiments involving mechanical non-coincidence and biaxial plane stress experiments all agreed with the photomechanical relationship suggested for polycarbonate.

The Moiré grid analyser method for the analysis of finite strain was set out in detail and was applied to the strain measurement of polycarbonate. It was shown that surface strain parameters can be evaluated from the fringe intercepts with the analyser grid directions and that their evaluation is independent of the relative rotation between the analyser and the specimen. Such a method is extremely useful in the study of inelasticity where observing time should be short: a photograph of the Moiré fringes or of the specimen grid can be taken for later analysis.

Frocht and co-workers studied celluloid extensively and showed that isoclinics are related to secondary principal stress direction. However, the effects of anisotropy, as reported by Frocht and Thompson[10a] and of excessive creep, as shown by Dill and Fowlkes[38], would tend to align the isoclinics with the principal stress directions. Polyethylene

on the other hand, having $-\overset{H}{\underset{H}{C}}-$ as the only atomic group, would exhibit a linear strain-optical relationship, as shown by Fried and Soup[5]. Polyethylene can be obtained in a highly crystalline form and thus offers itself as a good photoplastic material. However, opacity and brittleness are encountered with increasing crystallinity. It would appear that an ideal photoplastic model material is not yet available, nor have the similarity criteria been rigorously formulated for photoplasticity. The inelastic behaviour of polymers makes them suitable as model materials for inelasticity of metal, for example, high temperature creep. Furthermore, Sidebottom and co-workers[101, 102, 107] showed that laws which were initially formulated for plasticity are better applied to creep. It was shown that the time-dependence of deformation of polycarbonate of bisphenol A is non-linear with respect to the stress applied.

Polycarbonate of bisphenol A would be an excellent birefringent coating material because of its linear strain-optical relationship and good optical sensitivity. Mönch and Loreck[8] reported the use of Makrolon as a birefringent coating.

Polycarbonate of bisphenol A can also be used as a model material in plane stress condition, although the separation of principal strains would require oblique incidence observation and lateral strain determination. Such an analysis, combined

with a stress analysis, using a celluloid model, would permit a complete stress-strain analysis of a loading member.

Similarity criteria for a general loading path have not been touched upon and would offer a challenge to future researchers. Extensive tests[13] involving tubes subjected to non proportional loading would also be essential in establishing a post-elastic photomechanical relationship, and in such a test, strains would have to be accurately measured and stresses statically determined.

The effects of curvilinearity of specimen grids, when deformed, on the expressions given in Chapter 4 and the extension of the Moiré grid analyser method to curved surfaces should provide fruitful research.

APPENDIX 1

SECONDARY PRINCIPAL VALUES AND DIRECTIONS OF A TENSOR QUANTITY - STRESS TENSOR.

Tensor is used to describe a quantity which varies with direction such as stress, strain, dielectric coefficient, refractive index. In photomechanics, secondary principal directions and values associated with the direction of observation are frequently used.

The stress tensor is here selected as a specific case.

A1.1 DEFINITION

There are two ways of defining secondary principal stresses:

(1) in terms of plane stress components associated with the direction of observation, as given by Frocht[53].

"Secondary principal stresses for a given direction z' are principal stresses resulting from the stress components which lie in the plane normal to z'", i.e. the principal values and directions of the plane stress system associated with z' are secondary principal stresses and directions for the direction z'. Secondary quantities are given a prime. e.g. (p', q').

(2) in terms of the Cauchy stress quadric, given by Durelli and Riley[54].

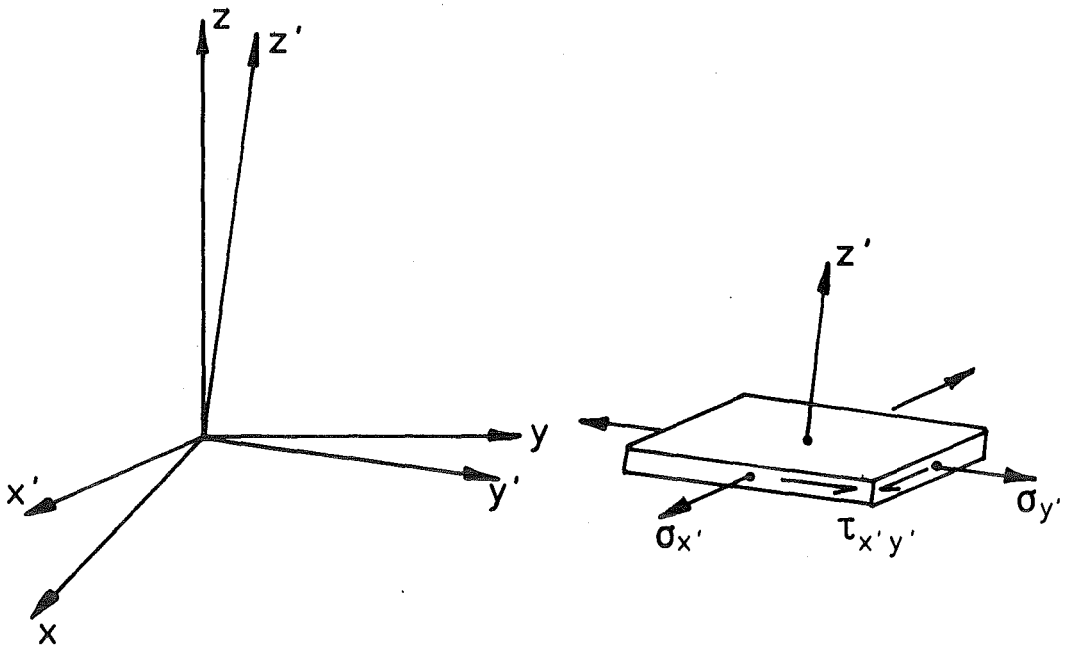

Fig. A.1.1 SECONDARY PRINCIPAL STRESSES FOR DIRECTION Z'

"For a given direction z', the diammetral plane normal to z' will cut the stress quadric along an ellipse or a hyperbola with stationary values of normal stress at the ellipse or the hyperbola axes, these give secondary principal values and directions of the stress tensor associated with z'". The second definition is easier to visualise with the aid of the stress quadric but the first definition allows quick evaluation of secondary principal stresses and secondary principal directions. The two definitions are shown to be equivalent as follows:

A1.2 SECONDARY PRINCIPAL STRESSES FOR A GENERAL DIRECTION

Let the stress tensor be described as $\tau_{\alpha\beta}$ with respect to a Cartesian coordinate system (x_1, x_2, x_3 or (x, y, z)). For a given direction z' form a Cartesian co-ordinate system (x_1', x_2', x_3' or x', y', z'). (Fig. A1.1).

The plane stress components associated with z' are:

$$\tau_{x'x'} = \sigma_{x'}$$

$$\tau_{y'y'} = \sigma_{y'} \qquad \text{(A1.1)}$$

and $\tau_{x'y'}$.

These stress components can be found from the tensor transformation laws:

$$\tau_{ij} = a_{i\alpha}\, a_{j\beta}\, \tau_{\alpha\beta} \qquad \text{(A1.2)}$$

where $\tau_{\alpha\beta}$ = stress tensor component in x, y, z.

τ'_{ij} = stress tensor component in x', y', z'.

$a_{i\alpha}$ = direction cosines of direction i in (x', y', z') to direction α in (x, y, z) or the coefficients of the transformation matrix.

(Note that shear stresses $\tau_{y'z'}$ and $\tau_{x'z'}$ also "lie" in the plane (x', y') but are not considered.)

Alternatively in matrix notations:

Let z' have direction cosines ℓ, m, n with respect to (x, y, z).

An arbitrary pair of orthogonal axes x', y' can be found in the plane normal to z'.

Let x' have direction cosines ℓ', m', n' with respect to (x, y, z).

y' have direction cosines ℓ'', m'', n'' with respect to (x, y, z).

Equation (A1.2) is equivalent to the following matrix representation:(55)

$$\sigma_{x'} = \begin{bmatrix} \ell' & m' & n' \end{bmatrix} \begin{bmatrix} \sigma_x & \tau_{xy} & \tau_{xz} \\ \tau_{xy} & \sigma_y & \tau_{yz} \\ \tau_{xz} & \tau_{yz} & \sigma_z \end{bmatrix} \begin{bmatrix} \ell' \\ m' \\ n' \end{bmatrix}$$

$$\sigma_{y'} = [\ell'' \ m'' \ n''] \begin{bmatrix} & & \\ & & \\ & & \end{bmatrix} \begin{bmatrix} \ell'' \\ m'' \\ n'' \end{bmatrix}$$

and

$$\tau_{x'y'} = [\ell'' \ m'' \ n''] \begin{bmatrix} & & \\ & & \\ & & \end{bmatrix} \begin{bmatrix} \ell' \\ m' \\ n' \end{bmatrix} \qquad \text{(A1.3)}$$

where $\begin{bmatrix} & \end{bmatrix}$ represents the matrix notation of the stress tensor.

Note that for normal stresses $\sigma_{x'}$ and $\sigma_{y'}$, only one set of direction cosines is used compared with two sets for the shear stress $\tau_{x'y'}$.

The secondary principal stresses and directions can be found from Mohr's stress circle of $\sigma_{x'}$, $\sigma_{y'}$, $\tau_{x'y'}$:

$$\begin{pmatrix} \sigma'_1 \\ \sigma'_2 \end{pmatrix} = \tfrac{1}{2}(\sigma'_x + \sigma'_y) \begin{pmatrix} + \\ - \end{pmatrix} \sqrt{\left(\frac{\sigma'_x - \sigma'_y}{2}\right)^2 + \tau^2_{x'y'}}$$

$$\tan 2\,\theta'_p = \frac{2\tau_{x'y'}}{\sigma'_x - \sigma'_y} \qquad \text{(A1.4)}$$

It can be seen that as directions of x', y' are arbitrary in the plane normal to z', they can be rotated about z' until the normal stresses σ'_x, σ'_y are stationary, i.e. equal to σ'_1, σ'_2, giving the secondary principal stresses and directions. This is equivalent to the second definition: stationary values of radial distance to the Cauchy quadric surface are sought in the diametral plane normal to z', where the radial distance to the Cauchy quadric surface is inversely proportional to the normal

stress associated with the direction.

An analytical development of the second definition is beneficial when only σ_1', σ_2' are required, or when (ℓ', m', n') and (ℓ'', m'', n'') are not conveniently chosen.

The second definition can be formulated as: find the maximum and minimum distance r where $r^2 = x^2 + y^2 + z^2$ (A1.5)

subjected to:

$$\sigma_x\, x^2 + \sigma_y\, y^2 + \sigma_z\, z^2 + 2\tau_{yz}\, yz + 2\tau_{zx}\, z.x + 2\tau_{xy}\, x.y = \pm 1 \qquad \text{(A1.6)}$$

(the Cauchy quadric surface)

and also $$\ell x + my + nz = 0 \qquad \text{(A1.7)}$$

This problem can be solved by the Lagrange multiplier method:

Let f represent L.H.S of (A1.6) (a)

and g represent L.H.S of (A1.7) (b)

where f, g are functions of x, y, z.

and form

$$F = \lambda_1(x^2 + y^2 + z^2) + f + \lambda_2 g = 0. \qquad \text{(c)}$$

It can be shown that:

$$(\sigma_x - \sigma_N)x + \tau_{xy}\, y + \tau_{zx}\, z + \frac{\lambda_2}{2}\, \ell = 0 \qquad \text{(d)}$$

where $\sigma_N = -\lambda_1 = \frac{f}{2}$ = the normal stress associated with radial distance r.

Another two equations similar to (d) together with (d) and (A1.7) can be put as:

$$\begin{bmatrix} \sigma_x - \sigma_N & \tau_{xy} & \tau_{xz} & \ell \\ \tau_{xy} & \sigma_y - \sigma_N & \tau_{yz} & m \\ \tau_{xz} & \tau_{yz} & \sigma_z - \sigma_N & n \\ \ell & m & n & 0 \end{bmatrix} \begin{bmatrix} x \\ y \\ z \\ \frac{\lambda}{2} \end{bmatrix} = 0 \quad (A1.8)$$

Equation A has non-trivial solution only when

$$\begin{vmatrix} \sigma_x - \sigma_N & \tau_{xy} & \tau_{xz} & \ell \\ \tau_{xy} & \sigma_y - \sigma_N & \tau_{yz} & m \\ \tau_{xz} & \tau_{yz} & \sigma_z - \sigma_N & n \\ \ell & m & n & 0 \end{vmatrix} = 0 \quad (A1.9)$$

giving a quadratic equation in σ_N yielding two secondary principal stresses.

The secondary principal directions can be found by solving for components x, y, z of r corresponding to a value of σ_N by substituting value of σ_N into three equations like (d).

$$\begin{bmatrix} \sigma_x - \sigma_N & \tau_{xy} & \tau_{xz} \\ \tau_{xy} & \sigma_y - \sigma_N & \tau_{yz} \\ \tau_{xz} & \tau_{yz} & \sigma_z - \sigma_N \end{bmatrix} \begin{bmatrix} x \\ y \\ z \end{bmatrix} = -\frac{\lambda}{2} \begin{bmatrix} \ell \\ m \\ n \end{bmatrix}$$

This is a system of 3 simultaneous equations, a typical value is:

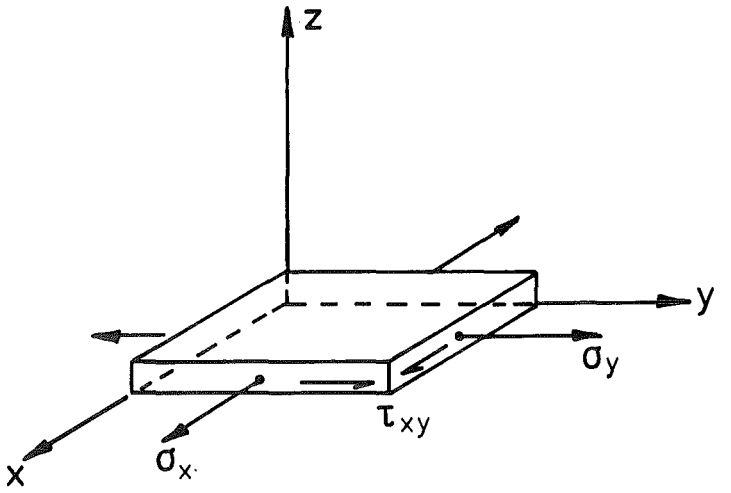

Fig. A.1.2 SECONDARY PRINCIPAL STRESSES FOR DIRECTION Z.

$$x = -\frac{\lambda}{2} \frac{\begin{vmatrix} \ell & \tau_{xy} & \tau_{xz} \\ m & \sigma_y - \sigma_N & \tau_{yz} \\ n & \tau_{yz} & \sigma_z - \sigma_N \end{vmatrix}}{\begin{vmatrix} \sigma_x - \sigma_N & \tau_{xy} & \tau_{xz} \\ \tau_{xy} & \sigma_y - \sigma_N & \tau_{yz} \\ \tau_{xz} & \tau_{yz} & \sigma_z - \sigma_N \end{vmatrix}} \qquad \text{(A1.10)}$$

Note that when (x', y', z') coincide with the (primary) principal directions of the stress tensor, the secondary principal stresses are equal to the (primary) principal stresses. Otherwise either both are smaller than the (primary) principal stresses or one of the secondary principal stresses is smaller than and one is equal to their corresponding (primary) principal stress.

A1.3 AN EXAMPLE OF SECONDARY PRINCIPAL STRESSES

Let z' coincide with z. (Fig. A1.2).

Choose x', y' to coincide with x, y

then $(\ell, m, n) = (0, 0, 1)$

$(\ell', m', n') = (1, 0, 0)$

$(\ell'', m'', n'') = (0, 1, 0)$

By equation (A1.3)

$$\sigma_{x'} = [1\ 0\ 0] \begin{bmatrix} \sigma_x & \tau_{xy} & \tau_{xz} \\ \tau_{xy} & \sigma_y & \tau_{yz} \\ \tau_{xz} & \tau_{yz} & \sigma_z \end{bmatrix} \begin{bmatrix} 1 \\ 0 \\ 0 \end{bmatrix} = [1\ 0\ 0] \begin{bmatrix} \sigma_x \\ \tau_{xy} \\ \tau_{xz} \end{bmatrix} = \sigma_x$$

Similarly $\sigma_{y'} = [0\ 1\ 0] \begin{bmatrix} & & \\ & & \\ & & \end{bmatrix} \begin{bmatrix} 0 \\ 1 \\ 0 \end{bmatrix} = \sigma_y$

$$\tau_{x'y'} = [0\ 1\ 0] \begin{bmatrix} \sigma_x \\ \tau_{xy} \\ \tau_{xz} \end{bmatrix} = \tau_{xy}$$

as expected, and σ_1', σ_2' and their directions can then be found.

By equation (A1.9)

$$\begin{vmatrix} \sigma_x - \sigma_N & \tau_{xy} & \tau_{xz} & 0 \\ \tau_{xy} & \sigma_y - \sigma_N & \tau_{yz} & 0 \\ \tau_{xz} & \tau_{yz} & \sigma_z - N & 1 \\ 0 & 0 & 1 & 0 \end{vmatrix} = 0$$

then

$$\sigma_N^2 - (\sigma_x + \sigma_y)\ \sigma_N + (\sigma_x\sigma_y - \tau_{xy}) = 0$$

giving

$$\sigma_N = \tfrac{1}{2}(\sigma_x + \sigma_y) \pm \tfrac{1}{2} \sqrt{(\sigma_x + \sigma_y)^2 - 4(\sigma_x\sigma_y - \tau_{xy})}$$

$$= \tfrac{1}{2}(\sigma_x + \sigma_y) \pm \tfrac{1}{2} \sqrt{(\sigma_x - \sigma_y)^2 + 4\ \tau_{xy}}$$

It can be seen the second method involves more algebraic operations.

APPENDIX 2

MAXWELL'S ELECTROMAGNETIC EQUATION

The two circuital laws between the electric and the magnetic field of the light wave - considered as an electromagnetic disturbance - give:

$$\frac{\partial \underline{B}}{\partial t} = -\,\text{curl}\ \underline{E} \qquad \text{(A2.1)}$$

$$\frac{\partial \underline{D}}{\partial t} = +\,\text{curl}\ \underline{H} \qquad \text{(A2.2)}$$

where: $\underline{E}$ = electric field intensity vector

$\underline{D}$ = electric displacement vector

$\underline{H}$ = magnetic field intensity vector

$\underline{B}$ = magnetic induction vector

for a non-magnetic medium:

$$\underline{B} = \mu_o \underline{H} \qquad \text{(A2.3)}$$

μ_o = magnetic permeability coefficient, a constant (not refractive index) for an uncharged anisotropic dielectric the dielectric tensor $\underline{\underline{K}}$ or K_{ij} is used to relate $\underline{D}$ and $\underline{E}$:

$$\underline{D} = \underline{\underline{K}} \cdot \underline{E} \quad \text{or} \quad D_i = K_{ij} E_j \qquad \text{(A2.4a)}$$

introduce the "index" tensor $\eta_{ij} = (K_{ij})^{-1}$

$$E_i = \eta_{ij} D_j \qquad \text{(A2.4b)}$$

and furthermore

$$\text{div}\ \underline{D} = 0 \qquad \text{(A2.5)}$$

$$\text{div}\ \underline{H} = 0 \qquad \text{(A2.6)}$$

it can be shown that:

$$\mu_o \frac{\partial^2 \underline{\underline{H}}}{\partial t^2} = -\text{curl}\ (\underline{\underline{\eta}} \cdot \text{curl}\ \underline{H}) \qquad \text{(A2.7)}$$

only in the undeformed state: $\underline{\underline{\eta}} = \eta_o\ \delta_{ij}$, δ_{ij} = kronecker's delta that

$$\mu_o \frac{\partial^2 \underline{\underline{H}}}{\partial t^2} = \eta \nabla^2 \underline{H} \text{ - wave equation} \qquad \text{(A2.8)}$$

when anisotropy exists the wave solution may not be an exact solution of the equation (A2.7).
This point was noted by Mindlin[37].

Mindlin showed that for a biaxial case the simple harmonic wave is the exact solution of (A2.7) only if the index tensor is homogeneous, (i.e. in a material obeying the stress-optical law, the stress is homogeneous) the order of "perturbation" is proportional to the following terms:

$$\lambda^2 \frac{\partial^2 \phi}{\partial s^2}\ ,\quad [\lambda \frac{\partial \phi}{\partial s}]^2,\quad \lambda z \frac{\partial \phi}{\partial s} \cdot \frac{\partial \mu}{\partial s},\quad \lambda z \frac{\partial^2 \mu}{\partial s^2}\ ,$$

$$\lambda^2 \frac{\partial \mu}{\partial s} \cdot \frac{\partial \phi}{\partial s}\ ,\quad \lambda z \left(\frac{\partial \mu}{\partial s}\right)^2 .$$

which are second order terms of : $\frac{\lambda \partial \mu}{\partial s}$, $z\frac{\partial \mu}{\partial s}$, $\lambda \frac{\partial \phi}{\partial s}$

where: λ = wave length of observing light

μ = refractive index

s = a typical length in the plane (along the stress trajectories)

ϕ = angle of principal direction of stress

z = optical path.

For a small gradient of optical anisotropy and for a visible spectrum wave length, terms involving λ are small. Similar conclusions are reached for a three dimensional case.

e.g. $z = \frac{1}{4}"$

$\delta\mu = .12 \quad \delta s = 1" \quad \delta\phi = 2\pi$ radians

$\lambda = 6000\ A^{\circ}$

$$z\frac{\partial\mu}{\partial s} = 3\times10^{-2}, \quad \lambda\frac{\partial\mu}{\partial s} \simeq 3\times10^{-6} \quad \lambda\frac{\partial\phi}{\partial s} = 1.5\times10^{-4}.$$

(This example is for a strain gradient of 1/in in polycarbonates). Note that $z\frac{\partial\mu}{\partial s}$ is large compared to other terms.

The cross product and square of these terms are small indicating that the "perturbation", in assuming wave solution satisfying Maxwell equations, is small except in regions of large gradient of $\frac{\partial\mu}{\partial s}$, for example in the "yield" boundary or cracktip occurring in a highly sensitive material (for example gelatin).

APPENDIX 3

FINITE STRAIN DESCRIPTIONS

A.3.1 INTRODUCTION

Theory of continuum mechanics expresses finite deformation in tensorial quantities: Lagrangian finite strain tensor (or Green's measure) and Eulerian finite strain tensor (Almansi's measure). Strain expressions employed in experimental strain analysis are not tensor components, they can be classified into Lagrangian engineering strains and Eulerian engineering strains. Seth[43,44] used a generalised measure of strain to embody all these strain descriptions and showed that a generalised strain measure can be expressed in terms of Green's measure or Almansi's measure.

A.3.2 LAGRANGIAN AND EULERIAN FINITE STRAIN TENSORS

Strain tensors are defined by considering the change of the square of the length of an infinitesimal line: $(ds)^2 - (ds_0)^2$[45,46], where ds_0 and ds are lengths of the infinitesimal line in the undeformed and deformed state respectively. If a rectangular Cartesian co-ordinate system is employed to describe both undeformed and deformed states, the strain tensors can be related to the displacement vector $\underline{u}$ where:

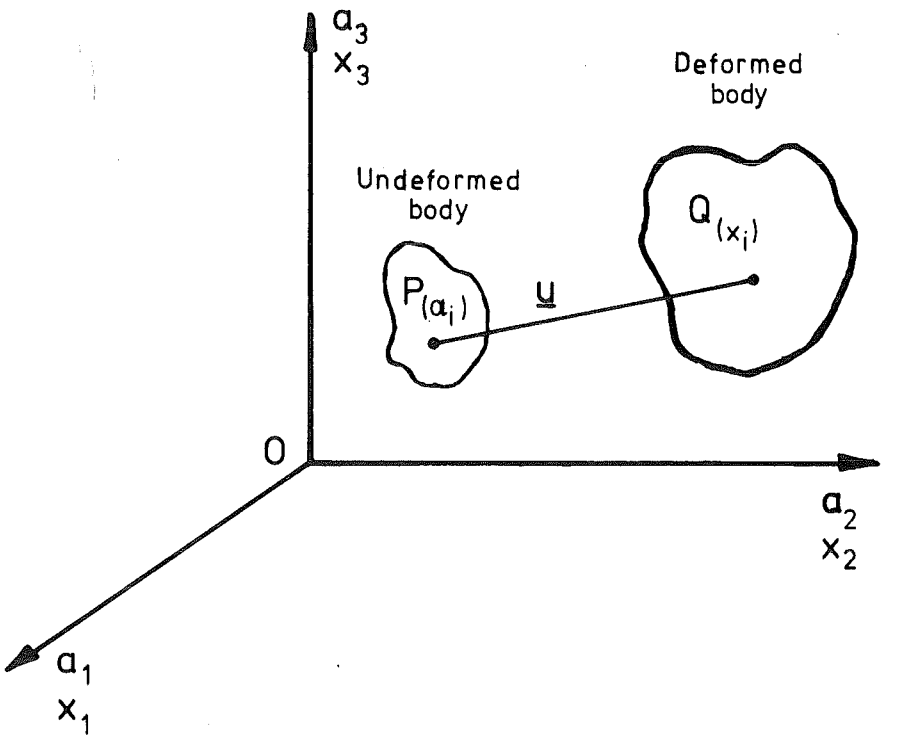

Fig. 2·1 DISPLACEMENT VECTOR AND COORDINATE AXES

$$u_i = x_i - a_i$$

$$\left.\begin{aligned}(ds)^2 - (ds_0)^2 &= 2\epsilon^{E}_{ij}\, dx_i\, dx_j \text{ Eulerian description} \\ &= 2\epsilon^{L}_{ij}\, da_i\, da_j \text{ Lagrangian description}\end{aligned}\right\} (2.20)$$

where a_i = co-ordinates of a material point in the undeformed state.

x_i = co-ordinates of the same material point in the deformed state.

u_i = components of the displacement vector.

Superscripts L and E indicate Lagrangian or Eulerian description.

In unabridged notions let:

$x, y, z,$ stand for x_1, x_2, x_3.

$a, b, c,$ stand for a_1, a_2, a_3.

$u, v, w,$ stand for u_1, u_2, u_3.

Typical components of ϵ^{L}_{ij}, ϵ^{E}_{ij} in terms of u, v, w are:

<u>Lagrangian finite strain tensor</u>:

$$\left.\begin{aligned}\epsilon^{L}_{aa} &= \frac{\partial u}{\partial a} + \frac{1}{2}\left[\left(\frac{\partial u}{\partial a}\right)^2 + \left(\frac{\partial v}{\partial a}\right)^2 + \left(\frac{\partial w}{\partial a}\right)^2\right] \\ \epsilon^{L}_{ab} &= \frac{1}{2}\left(\frac{\partial u}{\partial b} + \frac{\partial v}{\partial a}\right) + \frac{1}{2}\left[\frac{\partial u}{\partial a}\frac{\partial u}{\partial b} + \frac{\partial v}{\partial a}\frac{\partial v}{\partial b} + \frac{\partial w}{\partial a}\frac{\partial w}{\partial b}\right]\end{aligned}\right\} (2.21)$$

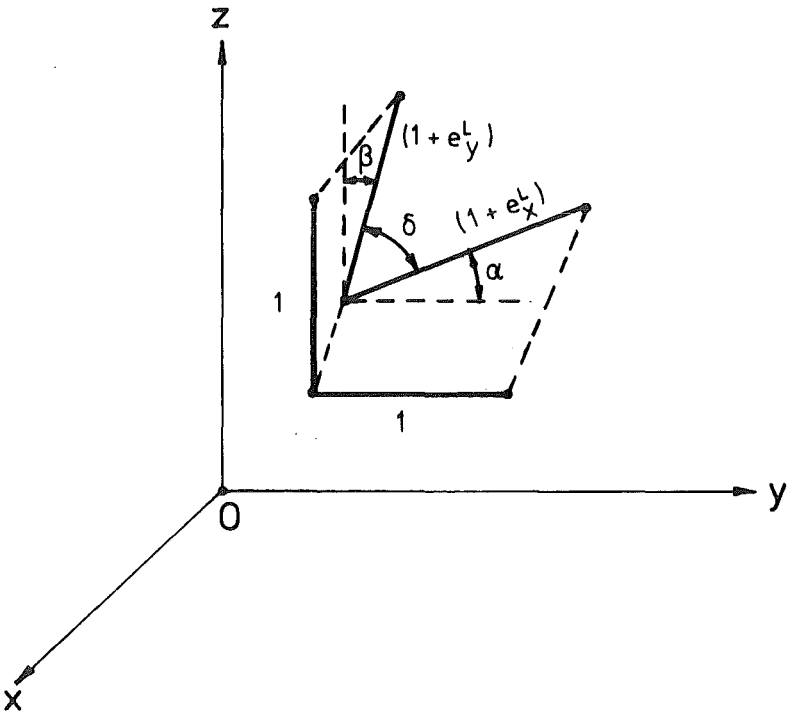

Fig. 2·2 LAGRANGIAN ENGINEERING STRAINS

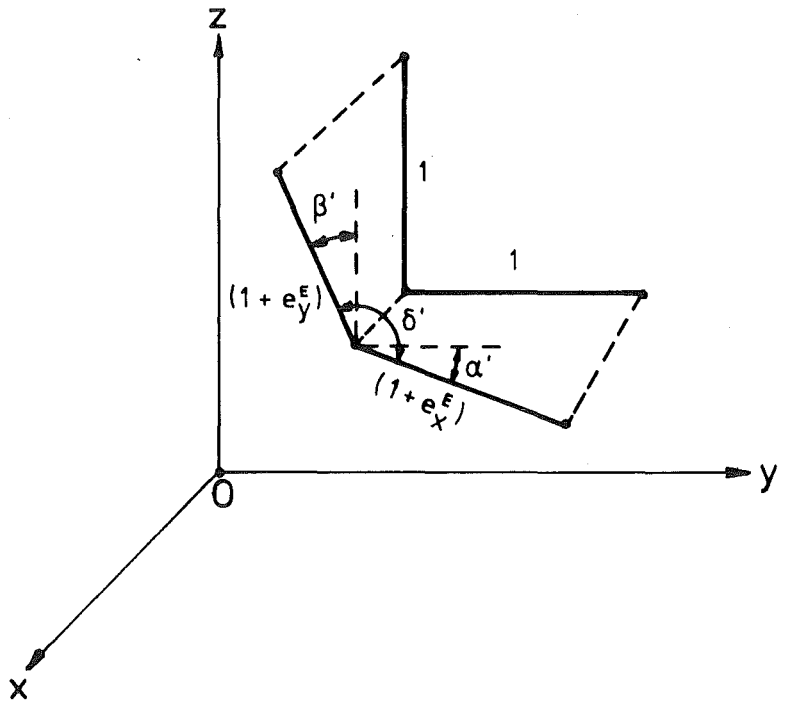

Fig. 2·3 EULERIAN ENGINEERING STRAINS

Eulerian finite strain tensor

$$\left.\begin{aligned} \epsilon^{E}_{xx} &= \frac{\partial u}{\partial x} - \frac{1}{2}\left[\left(\frac{\partial u}{\partial x}\right)^2 + \left(\frac{\partial v}{\partial x}\right)^2 + \left(\frac{\partial w}{\partial x}\right)^2\right] \\ \epsilon^{E}_{xy} &= \frac{1}{2}\left(\frac{\partial v}{\partial y} + \frac{\partial v}{\partial x}\right) - \frac{1}{2}\left[\frac{\partial u}{\partial x}\frac{\partial u}{\partial y} + \frac{\partial v}{\partial x}\frac{\partial v}{\partial y} + \frac{\partial w}{\partial x}\frac{\partial w}{\partial y}\right] \end{aligned}\right\} \quad (2.22)$$

The distinction between the two descriptions is: in the Lagrangian tensor the partial derivatives are evaluated with respect to an infinitesimal line originally parallel to one of the co-ordinate axes, whereas in the Eulerian strain tensor, the infinitesimal line parallel to a co-ordinate axis is attached to the deformed state. This point is illustrated by Parks and Durelli[47].

A.3.3 ENGINEERING STRAIN DESCRIPTION

In the above mathematical description, it can be shown ϵ^{E}_{ij} and ϵ^{L}_{ij} are symmetric second rank tensors; the principal values and directions can be found by analytical or graphical (Mohr's circle) means. However, they don't bear a direct relationship to physical measurements. The so called "Engineering strains" use change in length and angle to describe strain, although these strains are not tensor components. Refer to figures (2.2) and (2.3).

Eulerian Description:

$$* \text{ normal strain } e^{E} = \frac{ds - ds_o}{ds} = \text{extension per unit deformed length} \quad (2.23)$$

* shear strain $\gamma_{yz}^{E} = \delta' - \frac{\pi}{2} = \alpha' + \beta'$. (2.23)

Lagrangian Description:

* normal strain $e^{L} = \frac{ds - ds_o}{ds_o}$ = extension per unit undeformed length.

* shear strain $\gamma_{yz}^{L} = \frac{\pi}{2} - \delta = \alpha + \beta$ } (2.24)

The natural or logarithmic normal strain is defined as:

$$e^{N} = \log \frac{ds}{ds_o} = \log (1 + e^{L})$$

the definition of natural shear strain has not been well formulated. Seth[43] showed that it can be defined in terms of the Lagrangian finite strain tensor.

Natural strains are useful in inelastic problems of incompressible material.

A.3.4 RELATIONSHIP BETWEEN STRAIN DESCRIPTIONS

Engineering strains and finite strain tensors of the same description (Eulerian or Lagrangian) are readily related, but quantities of different descriptions and of natural strains cannot be interchanged unless they are principal values.

It can be shown that the directions of stationary normal strains of all strain expressions are coincident and the shear strains associated with these directions are zero.

They are called principal strain directions. This follows from the fact that they all describe deformation, a physical quantity.

However, a set of finite engineering strains does not allow principal strain values to be evaluated, unless they happen to be the principal strains, while the principal strains can be evaluated from any set of finite strain tensor components.

a. Relation between strain expressions of the same description.

By using line elements originally or finally parallel to co-ordinate axes, it can be shown that:(46)

* Lagrangian description:

$$\epsilon^{L}_{aa} = \tfrac{1}{2}\left[(1+e^{L}_{aa})^2 - 1\right] = e^{L}_{aa} + (e^{L}_{aa})^2$$

$$\epsilon^{L}_{ab} = \tfrac{1}{2}\,(1+e^{L}_{aa})(1+e^{L}_{bb})\,\sin\gamma^{L}_{ab} \qquad (2.25)$$

* Eulerian description:

$$\epsilon^{E}_{xx} = \tfrac{1}{2}\left[1-(1-e^{E}_{xx})^2\right] = e^{E}_{xx} - \tfrac{1}{2}(e^{E}_{xx})^2$$

$$\epsilon^{E}_{xy} = \tfrac{1}{2}\,(1-e^{E}_{xx})(1-e^{E}_{yy})\,\sin\gamma^{E}_{xy} \qquad (2.26)$$

For convenience we adopt only one subscript for normal strain and use variables x, y, z for both Lagrangian and Eulerian descriptions e.g. ϵ^{L}_{x} , ϵ^{E}_{x} .

b. Relation between Eulerian and Lagrangian engineering strains.

Only normal strains or principal strains can be related. From equation (2.23), (2.24) and for principal direction 1:

$$e_1^E = 1 - \frac{1}{1 + e_1^L}$$

hence (2.27)

$$e_1^N = \log (1 + e_1^L) = -\log (1 - e_1^E)$$

c. Relation between Eulerian and Lagrangian descriptions.

Equations (2.26) and (2.27) give

$$\epsilon_1^E = \tfrac{1}{2} \left[1 - \left(\frac{1}{1 + e_1^L}\right)^2\right] \qquad (2.28)$$

i.e. principal values of the Eulerian finite strain tensor can be related to those of the Lagrangian engineering strains. This is also true for any normal strain. The shear strains cannot be exactly related as is shown below: From equation (2.20):

$$2\epsilon_{ij}^E \, dx_i \, dx_j = 2\epsilon_{ij}^L \, da_i \, da_j$$

$$\epsilon_{ij}^E = \epsilon_{ij}^L \left(\frac{\partial a_i}{\partial x_i}\right) \left(\frac{\partial a_j}{\partial x_j}\right) \qquad (2.29)$$

terms like $\left(\frac{\partial a_i}{\partial x_i}\right)$ are not readily measured.

An approximate relation between ϵ^E_{ij} and ϵ^L_{ij} can be derived as follows:

Comparing two expressions of ϵ^E_x in (2.22) and (2.26):

$$e^E_i \simeq \frac{\partial u_i}{\partial x_i}$$

and furthermore by (2.20):

$$\frac{\partial u_i}{\partial x_i} = 1 - \frac{\partial a_i}{\partial x_i} \qquad (2.30)$$

Substitute (2.30) into (2.29) we have:

$$\epsilon^E_{ij} \simeq \epsilon^L_{ij} \, (1 - e^E_i)(1 - e^E_j)$$

by (2.27): $$\epsilon^E_{ij} = \epsilon^L_{ij} \frac{1}{(1 + e^L_i)} \frac{1}{(1 + e^L_j)} \quad \text{approximately} \quad (2.31)$$

In some cases $\left(\frac{\partial u_i}{\partial x_i}\right)$ can be directly obtained from experimental measurement, such as from Moiré fringes when there is no rigid body rotation[47].

A.3.5 FINITE AND INFINITESIMAL STRAIN

The boundary between finite and infinitesimal strain is not clear cut. The discrepancy between the two expressions are the second terms in equations (2.21) and (2.22) which are expressed in second order terms of partial derivatives of displacements. The classification of a deformation therefore depends on the amount of discrepancy or error accepted.

Parks and Durelli[47] showed that in certain cases, engineering strains are better approximations of finite strain tensor components than infinitesimal tensor strains.
* The discrepancy between the Lagrangian finite strain tensor and Lagrangian engineering strains can thus be used as a criterion for dividing a finite deformation from an infinitesimal one.

From equation (2.25):

$$\epsilon_a^L - e_a^L = \tfrac{1}{2}(e_a^L)^2$$

the "percentage error" based on e_a^L is:

$$\frac{\delta e_a^L}{e_a^L} = \tfrac{1}{2}\, e_a^L \qquad (2.32)$$

similarly for shear strain:

$$\frac{\delta \gamma_{ab}^L}{\gamma_{ab}^L} = e_a^L + e_b^L + e_a^L\, e_b^L \qquad (2.33)$$

If the acceptable percentage error is 10% (engineer's error!) the normal strains of two expressions can be considered equivalent if:

$$|\epsilon_a^L| \leq 5\% \,, \qquad \text{by} \qquad (2.32)$$

the error in shear strain depends on signs of the associated normal strains and cannot be generally estimated, the most severe case is when both normal strains are of the same sign

giving

$$|\epsilon_a^L + \epsilon_b^L| \leq 10\% \quad \text{approximately.}$$

Similar results can be obtained between the Eulerian finite strain tensor and Eulerian engineering strains.

* Discrepancy between Eulerian and Lagrangian finite strain tensors.

Only their principal values are considered:

By equation (2.28):

$$2\epsilon_1^E = 1 - (1 + e_1^L)^{-2}$$

$$= 2e_1^L - 3(e_1^L)^2 + 4(e_1^L)^3 - \ldots$$

compared to equation (2.25):

$$\epsilon_1^L - \epsilon_1^E = 4(e_1^L)^2 - 4(e_1^L)^3 + \ldots$$

$$\simeq 4(e_1^L)^2 \ (1 - e_1^L)$$

thus percentage error based on ϵ_1^L is:

$$\delta\epsilon_1^L \simeq 4e_1^L \qquad (2.34)$$

$$\epsilon_1^L = 4\epsilon_1^L \quad \text{approximately.}$$

Equation (2.34) indicates that for an error less than 10% Eulerian and Lagrangian finite strain tensors are equivalent only if:

$$|\epsilon_1^L| \leq 2.5\% \quad \text{approximately.}$$

APPENDIX 4

MOLECULAR CONFIGURATION AND GLASS TRANSITION TEMPERATURES OF POLYMERS USED IN PHOTOMECHANICS.

POLYMER	CONFIGURATION	T_g*
NYLON 6-6	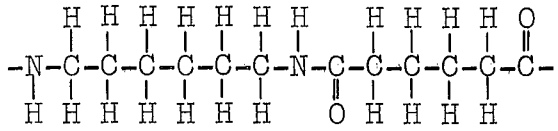 or 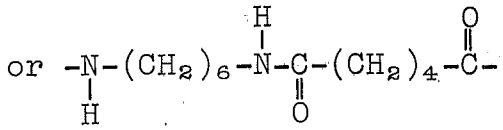	47°C
NYLON 6-10	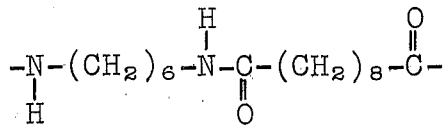	40°C
POLYETHYLENE	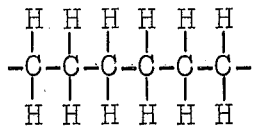	-45°C
POLYETHYLENE TEREPHTHALATE	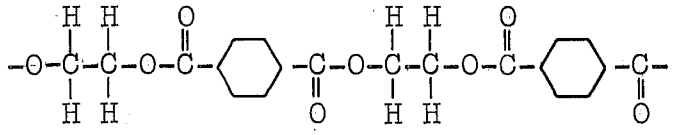	70°C
POLYSTYRENE	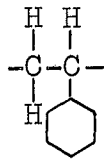	105°C
POLY (METHYL METHACRYLATE)	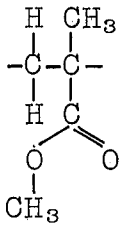	105°C, 120°C.

CELLULOSE NITRATE

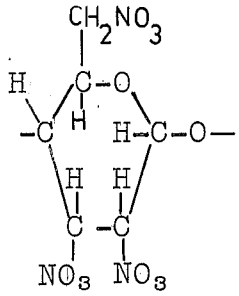

53°C

POLYCARBONATE of bisphenol A

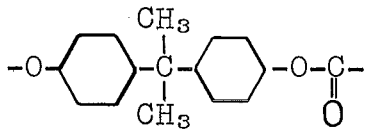

150°C

* Note: the glass transition temperatures given are only nominal.

APPENDIX 5

CONSIDERATIONS OF FRINGE DENSITY, FRINGE INCLINATION and FRINGE CONFUSION UNDER EFFECTS OF STRAIN.

A5.1 FRINGE DENSITY UNDER STRAIN

It is desirable to have a sufficient number of Moiré fringes about the point of interest to allow partial derivatives like $\frac{\partial N_X}{\partial \xi}$ to be accurately evaluated. At the same time the fringe density should not be too large to make fringes indistinguishable, in other words, the ratio of interfringe distance to pitch, such as $\frac{h_{Xn}}{g}$, should not be too small i.e. $\frac{h_{Xn}}{g} > M$ where M is a constant determined from experimental conditions.

From equations (4.5) and (4.8) and similar to equation (4.25):

$$\left(\frac{g}{h_{Xn}}\right)^2 = \frac{1}{(1+e_x)^2 \cos^2\gamma} \{[(1+\lambda)(1+e_x)\cos\gamma - \cos(\theta_o - \beta)]^2 + \sin^2(\theta_o - \beta)\} \qquad (4.31)$$

neglecting 3rd and higher order terms:

$$\left(\frac{g}{h_{Xn}}\right)^2 \simeq (\lambda + e_x)^2 + (\theta_o - \beta)^2 = \lambda_X^2 + \theta_X^2 \qquad (4.32)$$

similarly: $$\left(\frac{g}{h_{Yn}}\right)^2 \simeq (\lambda + e_y)^2 + (\theta_o + \alpha)^2 \qquad (4.33)$$

To avoid dense fringes $\frac{h_{Xn}}{g} > M$ thus:

$$(\lambda + e_x)^2 + (\theta_o - \beta)^2 < \frac{1}{M^2}$$

$$(\lambda + e_y)^2 + (\theta_o + \alpha)^2 < \frac{1}{M^2} \qquad (4.34)$$

($M = 5$ in the case study, Appendix 6).

Equation (4.34) indicates that to avoid dense fringe, λ should be of opposite sign to e_x and e_y and θ_o of opposite sign to α and $(-\beta)$. This is difficult to satisfy in general. Furthermore the roles of λ and θ_o in avoiding high fringe density are complementary.

In practice varying θ_o is easily effected and θ_o does not enter into the strain evaluation. On the other hand if λ is varied, its value should be accurately determined as shown in the error analysis.

A5.2 FRINGE INCLINATION WITH ξ AXIS UNDER STRAIN

The fringe inclination ϕ_X can be obtained from equation (4.5) in a similar way to equation (4.22):

$$\tan \phi_X = \frac{(1 + \lambda)(1 + e_x) \cos \gamma - \cos (\theta_o - \beta)}{\sin (\theta_o - \beta)} \qquad (4.35)$$

Neglecting second order and higher terms:

$$\tan \phi_X \simeq \frac{(\lambda + e_x)}{(\theta_o - \beta)} \qquad (4.36)$$

and similarly

$$\tan \phi_Y \simeq \frac{-(\theta_o + \alpha)}{(\lambda + e_y)} \qquad (4.36)$$

As shown by Post[67], it is desirable to have the Moiré fringes inclined about 45° to the analyser axes, i.e.:

$$\begin{aligned} |\lambda + e_x| &= |\theta_o - \beta| \\ |\lambda + e_y| &= |\theta_o + \alpha| \end{aligned} \qquad (4.37)$$

Both requirements are met for $\phi_X = 45°$ and $\phi_Y = -45°$ only if:

$$e_y - e_x = \alpha + \beta = \gamma \quad \text{i.e. along principal directions.}$$

Equation (4.36) indicates λ and θ_o can be used to obtain favourable inclinations but as previously discussed the use of varying θ_o is preferred. Note that when strains are zero, ϕ_X and ϕ_Y are at 45° to ξ if $\theta_o = \lambda$. As shown in the previous section, roles of λ and θ_o are complementary, suggesting that a small value of λ is used allowing substantial θ_o to be used when required.

A5.3 PREDICTION OF CONFUSION OF TWO MOIRÉ FAMILIES

Fringe confusion can be caused by the effect of the secondary Moiré fringes, as shown by Durelli and Parks[66], or by the tendency of a family to rotate towards the other[67] Fringe confusion is also influenced by contrast and density of fringes. For mismatch less than .30 and initial rotation less than 30° only primary Moiré fringes are observed. In

the case study (Appendix 6), it was found that, in order to obtain two distinct families the acute angle between the two should be greater than 45°. Let ϕ_{XY} be the angle between the X and Y families; we have:

$$\phi_{XY} = \phi_X - \phi_Y$$

and $$45^\circ < \phi_{XY} < 135^\circ \qquad (4.38)$$

giving $$|\tan \phi_{XY}| = \left|\frac{\tan \phi_X - \tan \phi_Y}{1 + \tan \phi_X \tan \phi_Y}\right| > 1$$

Exact expression can be obtained from equations like (4.35), only the approximate equations of (4.36) are used here:

$$\tan \phi_{XY} \simeq \frac{(\lambda + e_y)(\lambda + e_x) + (\theta_o + \alpha)(\theta_o - \beta)}{(\theta_o - \beta)(\lambda + e_y) - (\theta_o + \alpha)(\lambda + e_x)} \qquad (4.39)$$

Equations (4.38) and (4.39) allow λ and θ_o to be evaluated to avoid fringe confusion for given strain parameters. Post[67] used substantial λ and θ_o to avoid fringe confusion, but in the case of finite strain this technique is limited by fringe density: Moire fringes of the same family become too dense to be distinct.

A5.4 ROLE OF GRID PITCH IN SENSITIVITY OF MOIRÉ GRID ANALYSER

Investigators of small strain fields who do not use mismatch and initial rotation, advocate the use of high frequency grids to increase the density of the Moiré fringes in order to bring the interfringe distance to within the range of measure-

ment of equipment. Mismatch and initial rotation not only avoid fringe confusion and align fringes at favourable inclinations but also increase the fringe density.

For finite strain, too dense a fringe pattern is much more of a problem; the use of a high frequency grid is not essential especially if mismatch and rotation are used.

The error analysis also shows that the sensitivity obtained with a high frequency grid is shadowed by errors such as: "noise" error in grid printing, optical system defects, measuring and evaluating fringe intercepts.

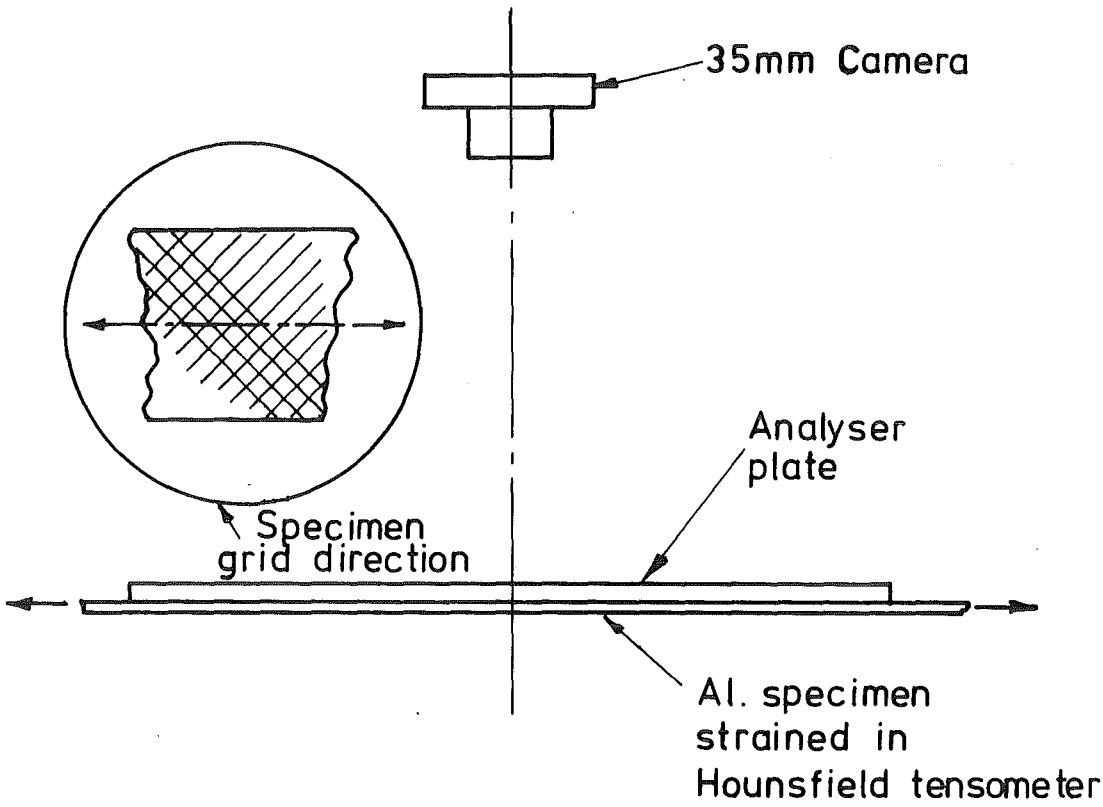

Fig. 4·7 (a) EXPERIMENTAL SET UP FOR THE CASE STUDY OF THE MOIRÉ GRID ANALYSER METHOD.

APPENDIX 6

CASE STUDY OF MOIRÉ GRID ANALYSER METHOD

A simple tensile test is used as a case study.

Tensile test pieces (1" wide, $5\frac{1}{2}$" parallel section) were machined from $\frac{1}{16}$" Aluminium sheet, on which an 133 L.P.I. grid had been photoengraved on a "vina-top Resist" photo-sensitive layer. The specimen grid directions were about 45° to the test piece axis (i.e. in direction of maximum shear strain and with tendency to cause fringe confusion). (Fig. 4.7(a)).

An analyser grid of 142 L.P.I. (nominal) was in intimate contact with the specimen grid throughout the test carried out in a Hounsefield tensometer. Reference points were marked at $\frac{1}{2}$" intervals on the axis along a 3" gauge length.

A load-deformation graph was recorded and photographs were taken at equal intervals of deformation. After processing, the negatives were kept at 20°C, 50°R.H.

The fringe intercepts were measured on a Nikon Shadowgraph which projects the negative on a ground glass screen having two fine crossed lines at 90° (ξ and η axes). The table on which the negative is placed can be rotated and traversed by two micrometers (10^{-4} in) set at 90°. Angular measurement on the ground glass screen is correct to 1 minute.

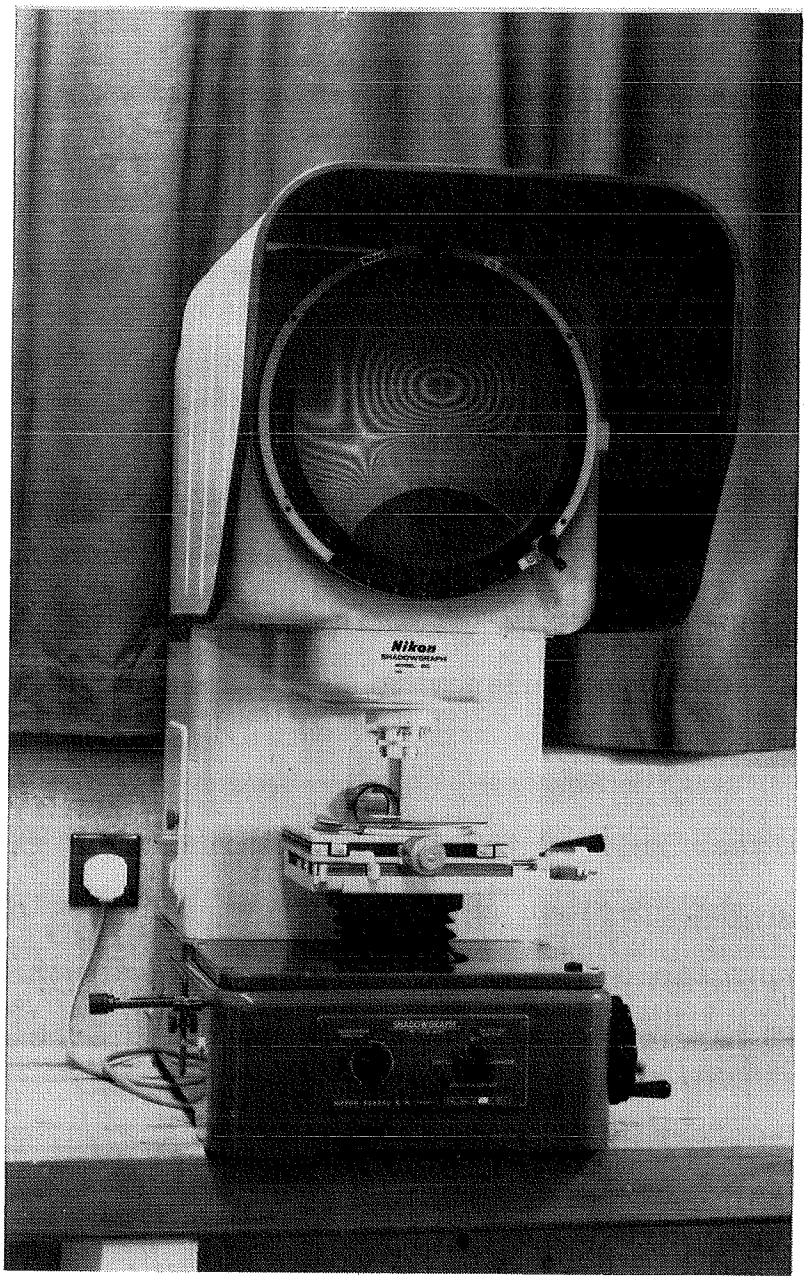

Fig. 4·7 (b) NIKON SHADOWGRAPH
(Isochromatic pattern of tensile strip with semicircular groove shown on screen.)

The grid analyser directions were aligned with the crossed lines of the screen and fringe intercepts were measured against fringe orders about each reference point, Fig. 4.7(b).

Where strain was fairly homogeneous, partial derivatives such as $\frac{\partial N_X}{\partial \xi}$ were taken from the graph of fringe orders versus fringe intercepts (Fig. 4.8). Otherwise they were evaluated by finite difference formulae.

The Lagrangian engineering strains were evaluated according to equations (4.6), (4.7), (4.9), (4.10) and (4.11). The components of Lagrangian finite tensor strain ϵ_{ij}^{L} was evaluated according to equation (2.25) of Appendix 3, from these components the maximum principal strain ϵ_1^L was evaluated and compared with the axial strain ϵ_g (Lagrangian finite strain) obtained from the 3" gauge length. Where the strain distribution was not uniform along the axis, ϵ_1^L was plotted along the 3" gauge length (Table 4.4 and Fig 4.9) and the average value $\bar{\epsilon}_1^L$ compared with ϵ_g. A typical set of data is given in Table 4.5.

Moiré fringes were observed to be fairly uniform until locally large strain took place when one family was distorted into curves. The shape of the slip line was indicated by points of large variation of slope as shown in photographs of Fig 4.10 which show the appearance of Moire fringes with various values of θ_0.

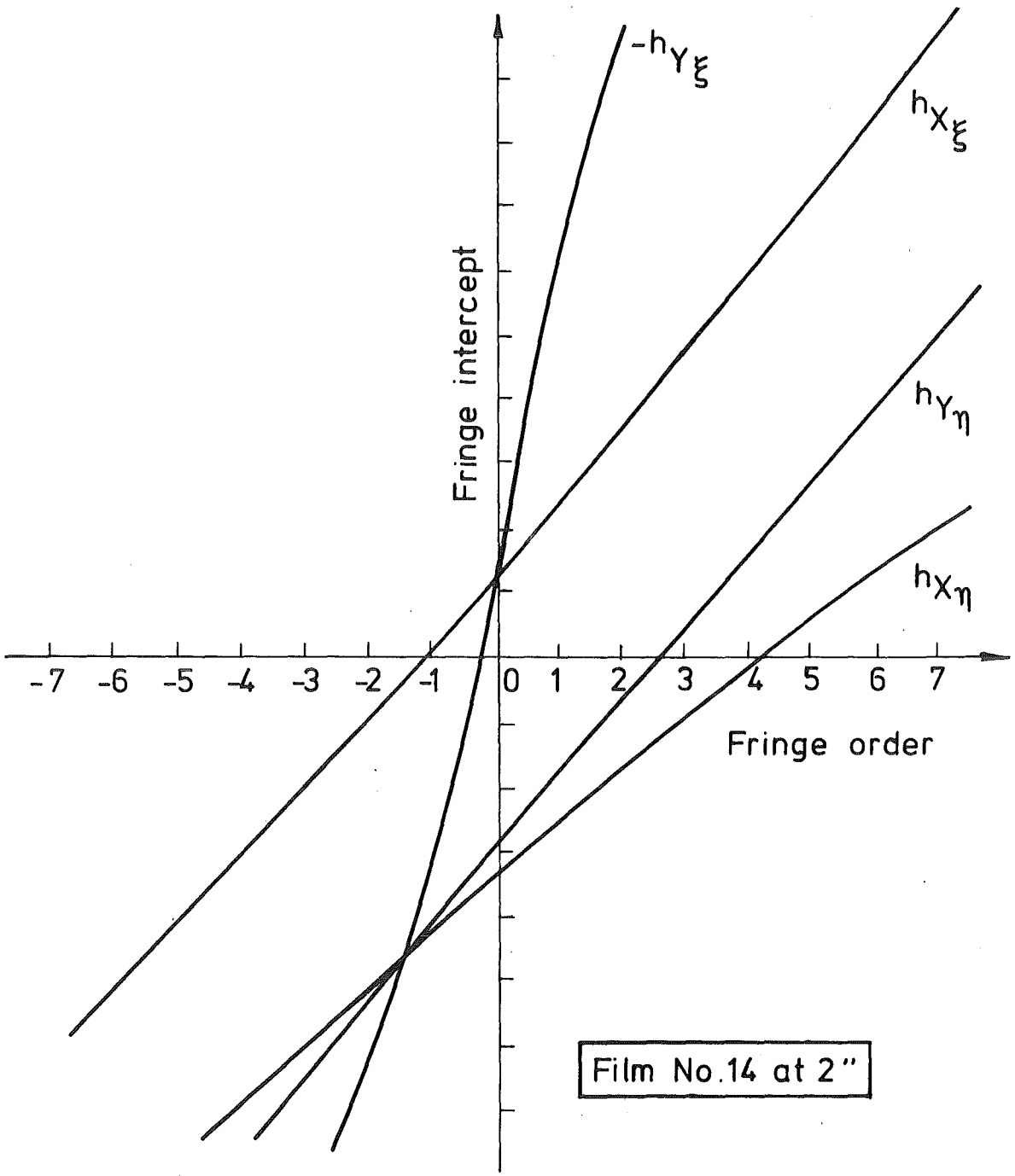

Fig. 4·8 FRINGE INTERCEPTS α FRINGE ORDERS FOR A REFERENCE POINT.

Under no strain, ϵ_1^L was found to be -.0003, indicating the amount of error involved.

Two photographs taken for the same strain field at different values of θ_o (analyser rotated) gave essentially the same strain: film numbers 9 and 10 in Table 4.3, confirm the independence of θ_o in strain evaluation.

TABLE 4.3

Film No.	4	8	9	10	11	12	13	14
ϵ_g	.0000	.0084	.0204	.0212	.0309	.0433	.0571	.0699
ϵ_1^L (at $\frac{1}{2}$" ref.pt)	-.0003	.0087	.0217	.0215	.0316	.0416	.0493	.0521
$\bar{\epsilon}_1^L$	-	-	-	-	.0341	.0472	.0605	.0694

TABLE 4.4

STRAIN DISTRIBUTION ALONG 3" GAUGE LENGTH

for Film No. 14 (obtained from Moiré fringes).

REFERENCE POINT	$-\frac{1}{2}$"	0	$\frac{1}{2}$"	1"	$1\frac{1}{2}$"	2"	$2\frac{1}{2}$"
STRAIN ϵ_1^L	.0529	.0529	.0533	.0710	.0888	.1032	.0751

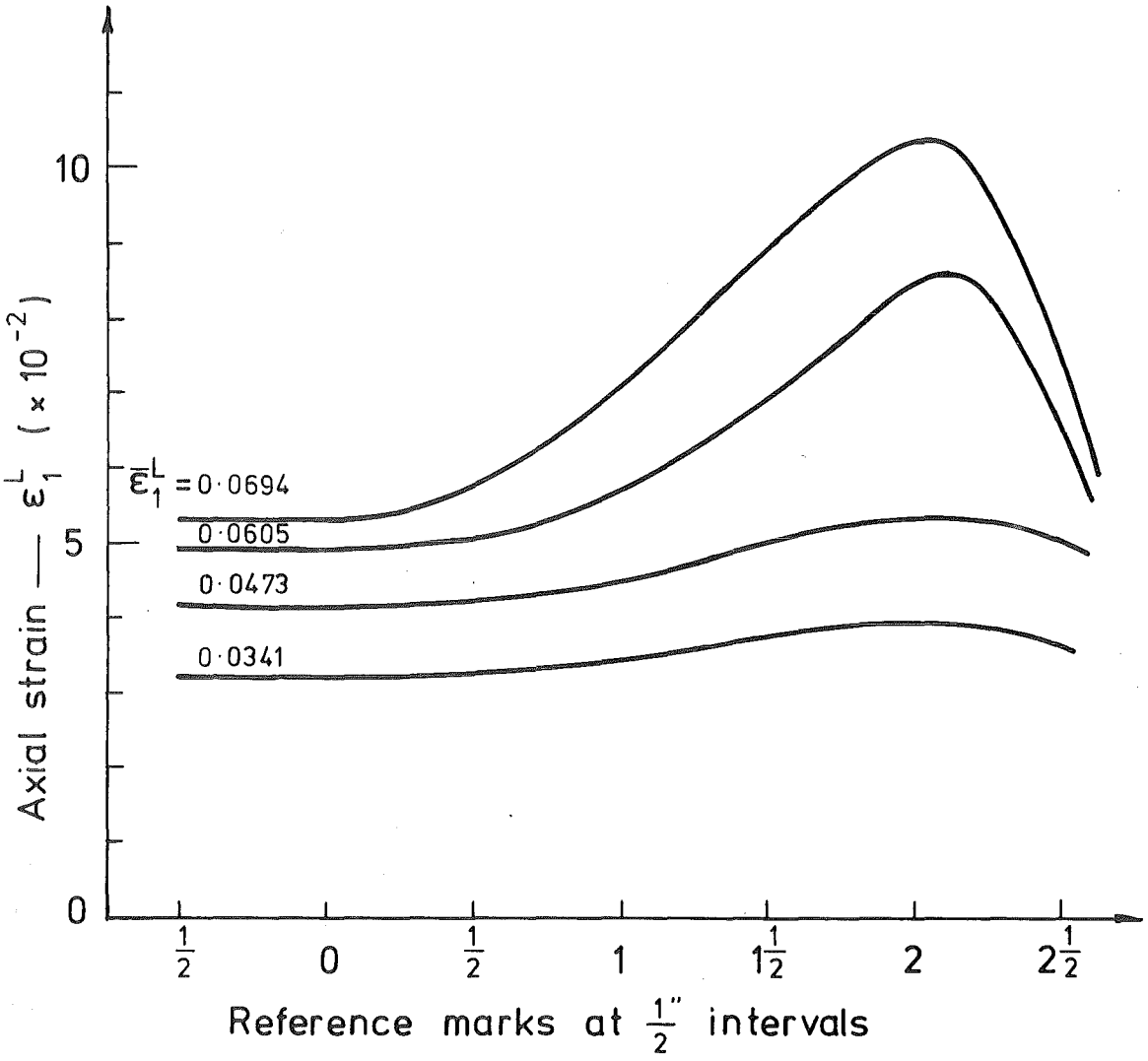

$\bar{\varepsilon}_1^L$ is the average strain obtained from the distribution curve.

Fig. 4·9 STRAIN DISTRIBUTION ALONG 3" GAUGE LENGTH

TABLE 4.5

Typical values for Film No 14 at $1\frac{1}{2}$".

mismatch: $\lambda = .06703$

Fringe intercepts:

X family $\frac{g}{h_{X\xi}} = .09964$, $\frac{g}{h_{X\eta}} = .13212$

Y family $\frac{g}{h_{Y\xi}} = -.03021$, $\frac{g}{h_{Y\eta}} = .09617$

$\tan(\theta_0 - \beta) = -.13657 \rightarrow \theta_0 - \beta = -7^\circ\ 46'$

$\tan(\theta_0 + \alpha) = -.03111 \rightarrow \theta_0 + \alpha = -1^\circ\ 46'$

$\gamma = 6^\circ$

$\epsilon_x^L = .0303$, $\epsilon_y^L = .0358$, $2\epsilon_{xy}^L = .1114$

$\epsilon_1^L = .0888$, $\epsilon_2^L = -.0228$

The use of approximation equations (3.16), (3.17) and (3.20), (3.21):

Equation (4.16) gives:

$$e_x = -.06703 + (1.06703).(.09964) - \tfrac{1}{2}[(.06703)^2 + (.09964)^2 + (.13212)^2]$$

$$= .0234 \quad (\text{cf } .0303)$$

Equation (4.17) gives:

$e_y = .0283$ (cf .0358)

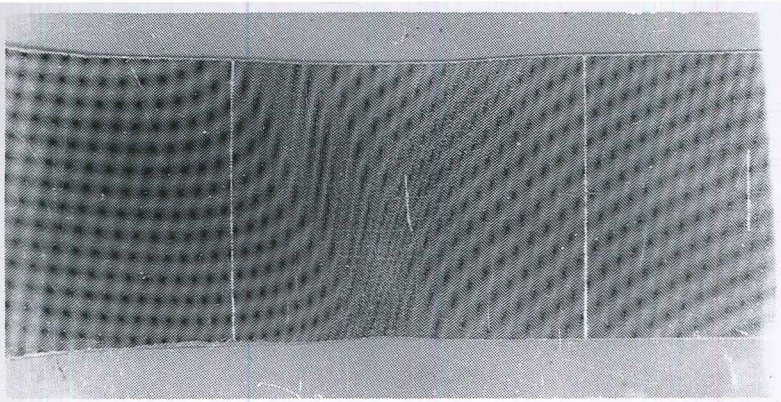

$\theta_0 = 4^\circ$

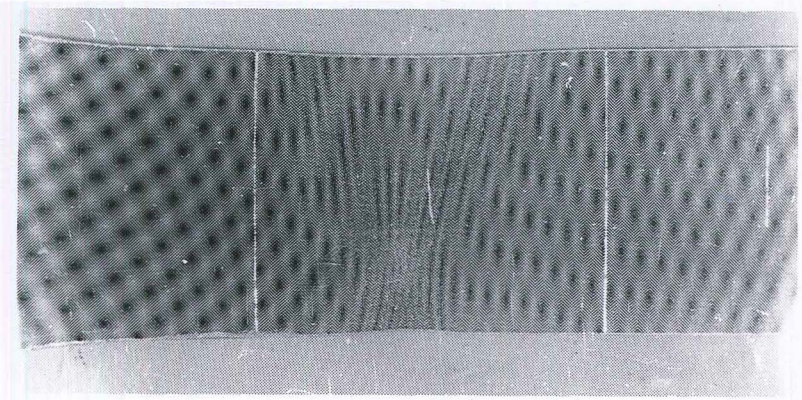

$\theta_0 = 0^\circ$

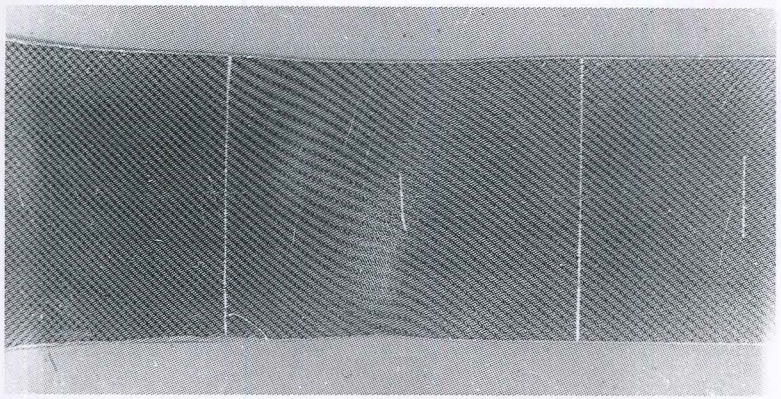

$\theta_0 = 19^\circ$

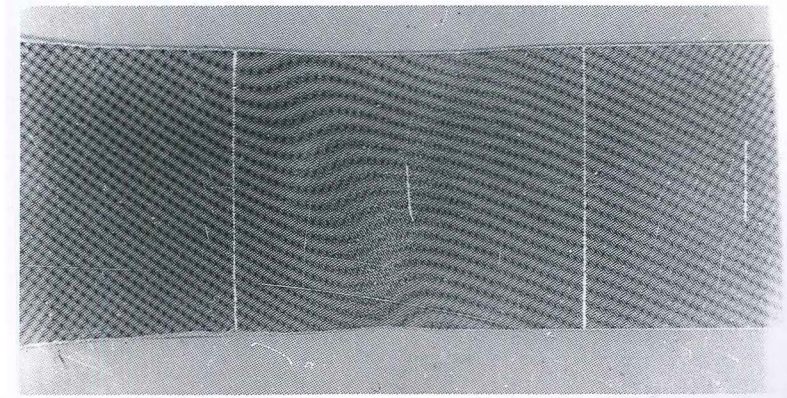

$\theta_0 = 12^\circ$

Fig. 4·10 VARIATION OF MOIRÉ FRINGE PATTERN WITH ROTATION OF ANALYSER.

Equation (4.20) gives:

$\tan\gamma = (.13212 - .03021)\,[1 - .06703 + (.09964 + .09617)]$

$= .10191 \cdot (1.12878)$

$= .1150$ cf $.1114$

Equation (4.21) gives:

$\tan\gamma \simeq .1019$ cf $.1114$

It can be seen approximations for shear strain are reliable, while those for normal strains are not as good because the directions of specimen grid were nearly at 45° to the principal strain directions.

APPENDIX 7

TABLE 6.1

DATA OF STRAIN FREEZING EXPERIMENTS

GRAPH	MATERIAL	INITIAL THICKNESS	INITIAL σ	T_{max}	SOAKING TIME	N_o	N_{max}	N^R	$N_{max}-N_o$	C^R_ϵ
(Figs 6.3&6.5)	-	(in)	(psi)	(°C)	(hour)	(fringe /in)	(fringe /in)	(fringe /in)	(fringe /in)	(10^3 fringe /in)
A	Bayer Makrolon	.228	523	135.5	$1\frac{1}{2}$	13.5	47.8	33.8	34.3	2.12
B	"	.234	505	136.5	$3\frac{1}{2}$	13.4	40.1	27	26.7	2.14
C	Lexan	.042	652	137	7	16.9	67.5	48.8	50.6	2.23
D	"	.042	628	148	1	16.7	145.7	132.5	129.0	1.72
E	"	.043	530	151	$1\frac{1}{2}$	13.8	176	152	162.2	1.48
F	"	.043	538	153	$1\frac{1}{2}$	16.1	256.6	239	240.4	1.26
G	"	.043	708	151.5	2	17.3	268.4	247.8	251.1	1.48

TABLE 6.2

VARIATION OF N'^{+} AND $\epsilon_1 - \epsilon_2$ IN A STRAIN-FREEZING EXPERIMENT

σ_o = 538 psi T_{max} = 153°

Time	Temp	N'	$e_1 - e_2$	$C_\epsilon^A(T)^{++}$
-h-min-	(°C)	(fringe/in)		(10^3 fringe/in)
0	20	-	-	-
3.30	141	46.6	.0143	3.26
4.10	145	70.5	.0287	2.43
5.38	147	91.8	.0419	2.20
7.20	150.5	115.8	.0625	1.84
8.15	152.5	154.5	.0989	1.59
9.00	153	200	.1451	1.43
10.20	151.5	249.2	.1919	1.36
12.05	139	256.5	-	-
22.00	78	254.2	-	-
26.00	54	254.3	-	-
40.00	20	254.2	-	-
zero load	20	238.5	.2001	1.26

$^{+}$ N' = fringe order per unit initial thickness

$^{++}$ $C_\epsilon(\dot{T}) = \frac{N'}{(e_1 - e_2)} \quad (1 - e_2)$

APPENDIX 8

ANALYSIS OF ERRORS IN TESTS ON THE MEANING OF ISOCLINICS

A8.1 EFFECT OF ERRORS IN β AND θ ON r'

Equation (6.23) can be written as:

$$r' = \frac{\sin 2\beta}{\tan 2\theta} - \cos 2\beta \qquad (6.27)$$

giving:

$$dr' = 2\left[\left(\frac{\cos 2\beta}{\tan 2\theta} + \sin 2\beta\right) d\beta - \frac{\sin 2\beta}{\sin^2 2\theta}\ d\theta\ \right]$$

$$\text{i.e. } \delta r' \leqslant 2\left\{\left|\frac{\cos 2\beta}{\tan 2\theta} + \sin 2\beta\right|\ \delta\beta + \left|\frac{\sin 2\beta}{\sin^2 2\theta}\right|\ \delta\theta\right\} \qquad (6.27)$$

where $\delta r'$, $\delta\beta$, $\delta\theta$ are errors in r', β, θ respectively. Equation (6.28) indicates that as $\theta \to 0^\circ$, the effects of errors in β and θ on r' become large.

Two values of β were used in this study: $\beta = 45^\circ$ and 60°. For $\delta\beta = \frac{1}{2}^\circ$, $\delta\theta = \frac{1}{2}^\circ$, the error $\delta r'$ is listed in Table 6.3:

TABLE 6.3.

β \ θ	45°	30°	10°	0°
60°	.03	.03	.12	∞
45°	.03	.04	.17	∞

From equation (6.22):

$$r = \frac{\sin 2\beta}{\tan 2\alpha} - \cos 2\beta \qquad (6.29)$$

i.e. effects of errors in β and α on r are similar to those of β and θ on r' as discussed above.

A8.2 EFFECT OF ERROR IN r' ON r^N

Neglect effect of error in β on r^N. Equation (6.26) gives:

$$\frac{dr^N}{dr'} = \frac{r' + \cos 2\beta}{\sqrt{1 + 2r' \cos 2\beta + r'^2}} \qquad (6.30)$$

Consider $\beta = 45°$ and $60°$, only, the ratio $\frac{\delta r^N}{\delta r'}$ is given in Table 6.4:

TABLE 6.4.

r'	$\frac{\delta r^N}{\delta r'}$	
	$\beta = 45°$	$\beta = 60°$
0	0	-.50
.5	.45	0
1	.70	.50
2	.89	.87
3	.95	.95

It can be seen that:

* $\frac{\delta r^N}{\delta r'}$ increases with r'.

* for $r' > 2$ $\delta r^N \simeq \delta r'$

* for $\beta = 60^\circ$ and $r' < .5$, δr^N is of opposite sign to $\delta r'$.

APPENDIX 9

MEANING OF ISOCLINICS TEST

$\beta = 59^\circ\ 45'$ $\quad \epsilon_1^R - \epsilon_2^R = .0855$ $\quad C_\epsilon^R = 1.63 \times 10^3$ Fringe/in

No.	$\alpha(^\circ)$	r	$r(\epsilon_1^R - \epsilon_2^R)$	$\epsilon_1^\sigma - \epsilon_2^\sigma$	$\theta(^\circ)$	r'	r^C	r^N
1	-	-	-	-	60	0	-	1
2	-	-	-	-	49	.38	-	.86
3	-	-	-	-	45	.50	-	.85
4	-	-	-	-	42	.59	-	.85
5	-	-	-	-	39	.68	-	.86
6	-	-	-	-	37	.75	-	.89
7	-	-	-	-	34	.85	-	.91
8	-	-	-	-	32	.92	-	.97
9	-	-	-	-	30	1.00	-	1.00
10	-	-	-	-	$27\frac{1}{2}$	1.11	-	1.07
11	-	-	-	-	26	1.18	-	1.17
12	49	.38	.032	.021	25	1.31	3.47	1.26
13	46	.47	.040	.031	$21\frac{1}{2}$	1.43	3.04	1.40
14	$45\frac{1}{2}$	.48	.041	.037	19	1.61	3.32	1.53
15	44	.53	.045	.042	17	1.78	3.36	1.73
16	42	.59	.051	.046	15	2.00	3.38	1.85
17	$38\frac{1}{2}$	.70	.060	.058	$14\frac{1}{2}$	2.06	2.95	2.17
18	36	.78	.067	.065	12	2.45	3.13	2.30
19	32	.92	.079	.077	11	2.64	2.86	2.58

BIBLIOGRAPHY

1. R.D. Mindlin, A Mathematical Theory of Photo-viscoelasticity, Journal of Applied Physics, 206-216, (1949).

2. L.N.G. Filon and H.T. Jessop, On the Stress-Optical Effect in Transparent Solids Strained Beyond the Elastic Limit, Phil. Trans. Roy. Soc. London, Series A, Vol. 223, 89-126 (1923).

3. M. Hetenyi, A Study in Photoplasticity, Proc. 1st U.S. Nat. Cong. Appl. Mech., 449-502, (1951).

4. B. Fried, Some Observations on Photoelastic Materials Stressed Beyond the Elastic Limit, Proc. Soc. Exp. Stress Analysis, Vol. 8, No. 2, 143-148, (1951).

5. B. Fried and N.H. Soup, A Study in Photoplasticity - The Photoelastic Effect in the Region of Large Deformation in Polyethylene, U.S. Nat. Cong. Appl. Mech. 477-483, (1954).

6. R. Hiltscher*, Theorie Und Anwendung der Spannungsoptik im Elastoplastichen Gebeit, Z. Ver dtsch Ing, Vol. 97, No. 2, 49-58, (1955).

7. T. Fujii and T. Tokuoka, On Birefringent Phenomena in Plastic Deformation of High Polymer Solids (Photoplasticity of Celluloid), Journal, Japan Society for testing materials, Vol. 10, 52-56, (1961).

8. E. Mönch and R. Loreck, A Study of the Accuracy and Limits of Application of Plane Photoplastic Experiments, Proc. of Int. Symposium on Photoelasticity (Ed. M.M. Frocht), 169-184, (1963).

9. M. Nisida, M. Hondo and T. Hasanuma, Studies of the Plastic Deformation by the Photoplastic Method, Proc. 6th

* Translated copy available.

Japan Nat. Con. Applied Mechs., 137-140, (1956).

10. M.M. Frocht and R.A. Thompson, Studies in Photoplasticity, Proc. 3rd U.S. Nat. Cong. Appl. Mechs., 533-540, (1953).

10a. M.M. Frocht and R.A. Thompson, Experiments on Mechanical and Optical Coincidence in Photoplasticity, Exp. Mech., 43-47, (Feb. 1961).

11. M.M. Frocht and R.A. Thompson, Further Work on Plane Elastoplastic Stress Distributions, Proc. of Int. Symposium on Photoelasticity, Ed. M.M.Frocht, 185-193, (1963).

12. Y.F. Cheng, Foundations for Three-dimensional Photoplasticity, Illinois Inst. of Technology, (Doctoral thesis), (1961).

13. M.M. Frocht and Y.F. Cheng, An Experimental Study of the Laws of Double Refraction in the Plastic State in Cellulose Nitrate - Foundations for three Dimensional Photoplasticity, Proc. of Int. Symposium on Photoplasticity 1961, Ed. M.M.Frocht, 195-216, (1963).

14. S.E.A. Bayoumi and E.K. Frankl, Fundamental Relations in Photoplasticity, British Jour. Appl. Phys., 306-310, (1953).

15. S.I. Gubkin, S.I. Dobrovol'skii* and B.B. Boiko, Photoplasticity, Izd. Akad. Nauk. BSSR Minsk., (1957).

16. C.V. Johnson III and W. Goldsmith, Optical and Mechanical properties of Birefringent Polymers, Experimental Mechanics, 263-268, (June 1969).

17. K. Ito, New Model Materials for Photoelasticity and Photoplasticity, Experimental Mechanics, 373-376, (1962).

* Translated copy available.

18. K. Sharples, Makrolon as a Photoelastic Model Material, Strain, Vol. 1, No. 2, 22-23, (April 1965).

19. G.L. Cloud, Mechanical-Optical Properties of Polycarbonate Resin and some Relating with Material Structure, Experimental Mechanics, 489-499, (1969).

20. W.A. Brill, Basic Studies in Photoplasticity, Ph.D. thesis Stantford University, (1966).

21. R.B. Heywood, Design by Photoplasticity, Chap and Hall, (1952).

22. J. Jarvornicky, Evaluation of Stresses and Strains in Two dimensional Photoplasticity, Journal of Strain Analysis, Vol. 3, No. 1, 33-38, (Jan. 1968).

23. T. Tokuoka, Theoretical Investigation of Birefringence - Deformation relations in Photo-elastoplasticity, Int. J. Solids Structure, Vol. 1, 343-350, (1965).

24. T. Tokuoka, Mechanical foundations of Birefringence of Photo-elastoplastic media, Int. J. Solids Structure, Vol. 2, 49-58, (1966).

25. R.D. Andrews and J.F. Rudd, Photoelastic Properties of Polystyrene in the Glassy State - Effect of Molecular orientation , Effect of temperature, J. Appl. Phys. 28, 1091-1095, 1097-1100, (1957).

26. J.F. Rudd, Photoelastic Properties of Polystyrene in the Glassy State - Part 3. Styrene Derivatives and Copolymers, J. Appl. Phys., 818-826, (1960).

27. E.F. Gurnee, Theory of Orientation and Double Refraction in Polymers, J. Appl. Phys., 1232-1240, (1954).

28. J.F. Rudd and E.F. Gurnee, Photoelastic Properties of Polystyrene in the Glassy-state - Effect of Temperature, J. Appl. Phys. 1096-1100, (1957).

29. G.R. Taylor and S.R. Darin, Birefringence and Crystallization in Elastomers, J. Appl. Phys., 1075-1079, (1955).

30. W. Ramberg and W.R. Osgood, Description of Stress-strain curves by Three Parameters, NACA T.N. 902 (1943).

31. G.U. Oppel and H.A. Peterson, Experimental Techniques for Photoelastic Analysis of Cellular Shells, Experimental Mechanics, 184-191, (1963).

32. A.R. Hunter and M.E. Schwarz, Development and Application of a Photoelastoplastic Method to Study Stress Distributions in Vicinity of a Simulated Crack, NASA, cr-655, (Dec. 1966).

33. E. Mönch and R. Jira, Studie zur Photoplastizitat von Celluloid am Rohr unter Innendruck, Z. Agnew Phys., Vol. 7, 450-453, (1955).

34. R.E. Ely, Biaxial Stress Results for Nylon, Experimental Mechanics, 267-271, (1968).

35. H.F. Brinson, The Ductile Fracture of Polycarbonate, Experimental Mechanics, 72-77, (1970).

36. J. Jarvornicky, Plastic Stress and Strain Concentration Factors in a Strip with a Hole or Notches under Tension, Journal of Strain Analysis, Vol. 3, No. 1, 39-49, (Jan. 1968).

37. R.D. Mindlin, The Optical Equations of Three Dimensional Photoelasticity, Journal of Applied Physics, 89-95, (1949).

38. E.H. Dill and C. Fowlkes, Photoviscoelasticity, NASA, cr-444, (May 1966).

39. E.G. Coker, L.N.G. Filon and H.T. Jessop, A Treatise on Photoelasticity, Cambridge, 2nd edition, (1957).

40. J.E.H. Braybon, A new Method of Measurement of the Variation with Wavelength of the Refractive Index and Absolute Stress Optical Coefficients of Amorphous Solids, Proceedings of the Physical Society, London, Section B, Vol. 63, 446-451, (1950).

41. D. Post, Photoelastic Evaluation of Individual Principal Stresses by Large Field Absolute Retardation Measurements, Proc. of S.E.S.A. Vol. XIII, No. 2, 119-132, (1956).

42. D. Post, Gerneric Nature of Absolute Retardation Photoelasticity, Experimental Mechanics, 233-241, (1967).

43. B.R. Seth, Generalized strain and Transition Concepts for Elastic - plastic deformation - creep and relaxation, Proceedings of 11th Int. Cong. Applied Mechanics, 383-389, (1964).

44. B.R. Seth, Measure Concept in Mechanics, Int. Journal. of Non-linear Mechanics, 35-40, (1966).

45. I.S. Sokolnikoff, Mathematical Theory of Elasticity, McGraw Hill, 2nd Edition, (1956).

46. Y.C. Fung, Foundations of Solid Mechanics, Prentice Hall, (1965).

47. V.J. Parks and A.J. Durelli, Various Forms of the Strain Displacement relations Applied to Experimental Strain Analysis, Experimental Mechanics, 37-47, (1964).

48. R.D. Andrews and R.M. Kimmel, Birefringence effects in Acrylonitrile Polymers, Part 1 - Effects at different temperatures, Part 2 - The 140°C transition temperature, J. Appl. Phys., 3194-3202, (1964), 3063-3071, (1965).

49. R.D. Andrews and V. Chatre, Stress Optical Properties of P.V.C. above the Glass Transition, J. Appl. Phys., 4266-4271, (1969).

50. A.V. Tobolsky, Properties and Structure of Polymers, Wiley, (1960).

51. H.F. Mark and N.Gaylord, Encyclopedia of Polymer Science and Technology, Vol. 10, Interscience, (1969).

52. W.F. Christopher and D.W. Fox, Polycarbonates, Reinhold Publishing Corporation, (1962).

53. M.M. Frocht, Photoelasticity, Vol II., John Wiley and Sons Inc., (1948).

54. A.J. Durelli and W.F. Riley, Introduction to Photomechanics, Prentice-Hall, (1965).

55. A.J. Durelli, E.A. Phillips and C.H. Tsao, Introduction to the Theoretical and Experimental Analysis of Stress and Strain, McGraw-Hill, (1958).

56. P.S. Theocaris, Moiré Fringes: A Powerful Measuring Device, Appl. Mech. Review, Vol 15, No. 5, 333-339, (May 1962).

57. J. Guild, Diffraction Gratings as Measuring Scales, Oxford University Press, (1960).

58. J. Guild, The Interference Systems of Crossed Diffraction Gratings: Theory of "Moiré" Fringes, Oxford University Press, (1956).

59. B. Kostak and K. Popp, Moiré Strain Gauges, Strain, Vol. 2 No. 2, 5-16, (1966).

60. G. Oster, M. Wasserman and C. Zwerling, Theoretical Interpretation of Moiré Patterns, Journal of the Optical Society of America, 169-175, (1964).

61. P.S. Theocaris and H.H. Kuo, The Moiré Method of Zonal and Line Gratings, Experimental Mechanics 267-272, (1965).

62. S. Morse, A.J. Durelli and C.A. Sciammarella, Geometry of Moiré Fringes in Strain Analysis, Proc. A.S.C.E. Eng. Mechanics Div., 105-126, (1960),

63. C.A. Sciammarella and A.J. Durelli, Moiré Fringes as a Means of Analysing Strains, Proc. ASCE Eng. Mech. Div. 55-74, (Feb 1961).

64. A.J. Durelli, V.J. Parks and T.L. Chen, Stress and Finite Strain Analysis of a Circular Ring Under Diammetral Compression, Experimental Mechanics, 210-214, (1969).

65. B. Kostak, General Interpretation of Moiré Patterns in Strain Analysis, Journal of Strain Analysis, Vol. 3, No. 2, 90-95, (April 1968).

66. A.J. Durelli and V.J. Parks, Moiré Fringes as Parametric Curves, Experimental Mechanics, 97-104, (1967).

67. D. Post, The Moiré Grid Analyser Method for Strain Analysis, Experimental Mechanics, 368-377, (1965).

68. R.H. Bromley, Two Dimensional Strain Measurement by Moiré, Proceedings of the Physical Society of London, B., Vol. 69, 373-381, (1956).

69. G.S. Holister, Experimental Stress Analysis, Principles and Methods, Cambridge University Press, (1967).

70. G.S. Holister and A.R. Luxmore, The Production of High-Density Grids, Experimental Mechanics, 210-216, (1968).

71. J.D.C. Crisp, The Measurement of Plane Strains by a Photo-screen Method, Proc of S.E.S.A., Vol. 15, No. 1, 65-76, (1957).

72. A. Vinckier and R. Dechaene, Use of the Moiré Effect to Measure Plastic Strains, ASME TRANS 82 D, J. Basic Eng. 2., 426-434, (June 1960).

73. W. Bossaert, R. Dechaene and A. Vinckier, Computation of Finite Strains from Moiré Displacement Patterns, Journal of Strain Analysis, 65-75, (January 1968).

74. C.A. Sciammarella, Basic Optical Law in the Interpretation of Moiré Patterns Applied to the Analysis of Strains - Part 1, Experimental Mechanics, 154-160, (1965).

75. B.E. Ross, C.A. Sciammarella and D. Sturgeon, Basic Optical Law in the Interpretation of Moiré Patterns Applied to the Analysis of Strains - Part 2, Experimental Mechanics, 161-166, (1965).

76. R.C. Sampson and D.M. Campbell, The Grid Shift Technique for Moiré Analysis of Strain in Solid Propellants, Experimental Mechanics, 449-457, (1967).

77. F.D. Chiang, V.J. Parks and A.J. Durelli, Moiré - Fringe Interpolation and Multiplication by Fringe Shifting, Experimental Mechanics, 554-560, (1968).

78. D. Post, Sharpening and Multiplication of Moiré Fringes, Experimental Mechanics, 154-159, (1967).

79. D. Post, New Optical Methods of Moiré Fringe Multiplication, Experimental Mechanics, 63-68, (Feb. 1968).

80. C.A. Sciammarella, Moiré Multiplication by Means of Filtering and a Wave Reconstruction Process, Experimental Mechanics, 179-185, (1969).

81. J.H. Lamble and A.P. Vafiadakis, The Application of Moiré Rotational Mismatch Techniques to Strain Analysis, Journal of Strain Analysis, Vol. 2, No. 2, (1967).

82. F.P. Chiang, A Method to Increase the Accuracy of the Moiré Method, Proc A.S.C.E. E.M. 91, 137-149, (1965).

83. H.J. Duffey and G.K. Mesmer, Finite Rotation and Strain Measurement Using the Moiré Technique, Experimental Mechanics, 537-540, (1967).

84. L.P. Martin and F.D. Ju, The Moiré Method for Measuring Large Plane Deformations - General Theory and Application to Homogeneous Deformation, Journal of Applied Mechanics, 385-391, (1969).

85. F.P. Chiang, Gap Effect in Moiré Fringes, Experimental Mechanics, 294-296, (1970).

86. F.P. Chiang, Techniques of Optical Spatial Filtering Applied to the Processing of Moiré Fringe Patterns, Experimental Mechanics, 523-526, (1969).

87. L.E. Nielsen, Mechanical Properties of Polymers, Reinhold, (1962).

88. P.S. Theocaris, A Review of the Rheo-optical Properties of Linear high Polymers, Experimental Mechanics, 105-114, (1965).

89. M.L. Williams and R.J. Arenz, The Engineering Analysis of Linear Photoviscoelastic Materials, Experimental Mechanics, 249-262, (1964).

90. P.D.W. Soden and R. Sowerby, Large Deformation of Time Dependent Materials in Uniaxial Tension, Journal of Strain Analysis, Vol. 4, No. 3, 199-207, (1969).

91. R.N. Haward and G. Thackray, The Use of a Mathematical Model to Describe Isothermal Stress-strain curves in Glassy Thermoplastics, Proceedings of the Royal Society A, 302, 453-472, (1968).

92. R. Lansard, Fillets Without Stress Concentration, Proc. of S.E.S.A., Vol. XIII, No.1, 97-104, (1956).

93. F.R. Shanley, Weight-strength Analysis of Aircraft Structures, Dover, (1960).

94. J.O. Smith and O.M. Sidebottom, Inelastic Behaviour of Load-carrying Members, Wiley, (1965).

95. J. Bahuaudand M. Boivin, Etude du Coefficient de Poisson pour des Deformations Elastiques, élastico-plastiques, petites ou finites, Journal de mécanique, 141-153, (1968).

96. J. Bahuaud and M. Boivin, Nouvel aspect des Formules du coefficient de Poisson : sécant et Tangent, Journal de mécanique, 553-564, (1969).

97. E. Mönch and D. Galster, A Method for producing a Defined Uniform Biaxial Tensile Stress Field, British Jour. of Applied Physics, Vol. 14, 810-812, (1963).

98. D.C. Drucker, Photoelastic Separation of Principal Stresses by Oblique Incidence, Journal of Applied Mechanics, A 156-A 160, (Sept. 1943).

99. D.C. Drucker, The Method of Oblique Incidence in Photoelasticity, Proc. of S.E.S.A., Vol. VIII, No. 1, 51-66, (1951).

100. J.G. Williams and H. Ford, Stress-Strain Relationships for Some Unreinforced Plastics, Journal of Mechanical Engineering Science, 405-417, (1964).

101. S. Dharmarajan and O.M. Sidebottom, Arc Hyperboline Sine Creep Theory Applied to Torsion-Tension Member of Circular Cross-section, Experimental Mechanics, 153-160, (1963).

102. M.R. Shammamy and O.M. Sidebottom, Incremental versus Total Strain Theories for Proportionate and Non-proportionate Loading of Torsion-Tension Members, Experimental Mechanics, 497-505, (1967).

103. P.S. Theocaris, Experimental Solution of Elastic-Plastic Plane-stress Problems, J. of Applied Mechanics, 735-743, (Dec. 1962), (1962 B).

104. P.S. Theocaris, Combined Photoelastic and Electrical Analog Method for Solution of Plane Stress Plasticity Problems, Experimental Mechanics, 207-214, (Sept.1963).

105. P.S. Theocaris and E. Marketos, Elastic-plastic Analysis of Perforated Thin Strips of a Strain Hardening Material, Journal of the Mechanics and Physics of Solids, Vol. 12, 377-390, (1964).

106. Farbenfabriken Bayer, Makrolon: Description and Types, (1963).

107. J.L. Schlafer and O.M. Sidebottom, Experimental Evaluation of Incremental Theories for Nonproportionate Loading of Thin-walled Cylinders, Experimental Mechanics, 500-506, (1969).